Development of Optical Coherence Tomography for Quantitative Analysis of Cardiac Morphology

by

Michelle Cua

B.A.Sc. (Hons.), Simon Fraser University, 2011
B.Sc., Simon Fraser University, 2011

Thesis Submitted in Partial Fulfillment

of the Requirements for the Degree of

Master of Applied Science

in the

School of Engineering Science

Faculty of Applied Science

© Michelle Cua 2014

SIMON FRASER UNIVERSITY

Spring 2014

Approval

Name: **Michelle Cua**

Degree: **Master of Applied Science**

Title of Thesis: ***Development of Optical Coherence Tomography for Quantitative Analysis of Cardiac Morphology***

Examining Committee:

Chair: **Dr. Andrew Rawicz, P.Eng.**
Professor

Dr. Marinko Sarunic, P.Eng.
Senior Supervisor
Associate Professor

Dr. Glen Tibbits
Supervisor
Professor and Chair

Dr. Mirza Faisal Beg, P.Eng.
Supervisor
Associate Professor

Dr. Glenn Chapman, P.Eng.
Internal Examiner
Professor
Department of Engineering Science

Date Defended: April 24, 2014

Partial Copyright Licence

Abstract

Transgenic mouse models have been instrumental in the elucidation of the molecular mechanism behind many cardiac diseases such as Marfan syndrome. However, the small size of the murine heart has hampered the characterization of its cardiac morphology. In this project, we describe the development of a murine cardiac imaging modality using optical coherence tomography (OCT). After fixation and optical clearing, the hearts were imaged from multiple perspectives. These data sets were then corrected for refraction and registered together to yield a single volume of the whole heart. From this OCT volume, we then applied techniques from computational anatomy to quantify morphological parameters such as wall thickness, luminal volume, and wall masses. Using this pipeline, we performed a preliminary study comparing the cardiac morphology of a mice model of Marfan syndrome with their wild-type counterparts.

Keywords: optical coherence tomography, cardiac imaging, morphometric analysis, computational anatomy

Acknowledgements

I am fortunate to have been surrounded by a group of supportive individuals, without whom I would not have been able to complete this thesis. In particular, I would like to give a shout out to the following people:

To my senior supervisor, Dr. Marinko Sarunic, for his continuous support, patience, and encouragement.

To my committee members, Dr. Glen Tibbits and Dr. Mirza Faisal Beg, for their guidance, insightful comments, and technical expertise. Their help and knowledge in cardiac biology and image processing respectively was invaluable.

To Dr. Glenn Chapman for imparting his extensive knowledge and passion in optics and lasers.

To the members of our collaborating lab, Molecular Cardiology and Physiology group. In particular, I would like to thank Dr. Eric Lin for his guidance, feedback, and advice during group meetings, and Dr. Xiaoye Sheng and Ling Lee for providing the biological samples as well as imparting their knowledge in cardiac biology and echocardiography.

To my friends within Biomedical Optics Research Group, for the technical help and camaraderie, and for making this journey entertaining.

To the members of the SFU mechanics shop, for their speedy help in the design and construction of various parts that were needed for my system.

To my family for their unconditional love and continued support in all my endeavours.

Table of Contents

List of Tables

List of Figures

List of Acronyms

Ao	Aorta
AT_1	Angiotensin II Type 1 receptor
BPD	Balanced Photodiode Detector
BW	Body Weight
CCA	Complex Conjugate Ambiguity
CCAC	Canadian Council of Animal Care
CMR	Cardiac Magnetic Resonance
DCM	Dilated Cardiomyopathy
DFT	Discrete Fourier Transform
DMSO	Dimethyl sulfoxide
DOF	Depth of Focus
FBN1	Fibrillin 1
FC	Fiber Coupler
FC/S	Fiber Coupler or Optical Switch
FWHM	Full Width at Half Maximum
GM	Galvanometer-Scanning Mirrors
IVS	Interventricular Septum
LA	Left Atrium
LV	Left Ventricle
MFS	Marfan Syndrome
MR	Mitral Regurgitation
PCA	Principal Component Analysis
PM	Papillary Muscle
PSF	Point-Spread Function
RA	Right Atrium
RMSE	Root-Mean-Squared Error
RV	Right Ventricle
SD-OCT	Spectral Domain Optical Coherence Tomography
SNR	Signal-to-Noise Ratio
SS-OCT	Swept-Source Optical Coherence Tomography
TD-OCT	Time Domain Optical Coherence Tomography

TGF-β	Transforming Growth Factor β
OCT	Optical Coherence Tomography
PBS	Phosphate-Buffered Solution
µCT	Micro-Computed Tomography
US	Ultrasound
WT	Wild-Type

Chapter 1.   Introduction

Marfan syndrome (MFS) is a genetic connective tissue disorder affecting 1 in every 5,000 to 10,000 individuals [1], [2]. Approximately 75% of cases are inherited, while the remaining are *de novo* mutations [2]. Due to the ubiquity of connective tissue, MFS affects multiple systems in the body. The most visible symptoms are the skeletal symptoms, such as the disproportionately long limbs, arachnodactyly, and a deformed chest cavity (pectus carinatum or excavatum) [2], [3]. MFS also affects the ocular symptom, causing lens dislocation, myopia, and a flattened cornea [2], [3]. However, cardiovascular complications such as aortic enlargement and dissection are the primary cause of morbidity and mortality.

Marfan syndrome is currently incurable, but is medically managed through pharmacological and surgical interventions. Current therapies focus on delaying the aortic growth due to its associated morbidity. With proper management, the life expectancy of those with MFS can be extended from 37 years to the mid-70s [4]. MFS has been difficult to diagnose and treat due to its complex etiology: MFS can result from numerous different genetic mutations normally in the fibrillin 1 (*FBN1*) gene and exhibits marked phenotypic variability, even within families with the same genetic mutation [3], [5], [6].

Animal models can be beneficial in elucidating the etiology behind Marfan syndrome. Despite the difference in size between mice and humans, mice are becoming increasingly common as animal models for human diseases due to their well-characterized genome, ease of genetic manipulation, relatively inexpensive husbandry, and short gestation period [7], [8]. Through targeted gene manipulation, various aspects of the human condition, such as the progressive aortic dilation, have been mimicked and studied. Using histology, researchers have been able to study the aortic wall composition, structure, and size in response to these targeted manipulations [9]–[11]. For example, histological analyses on rodent models of MFS have helped determine the link between fibrillin 1 levels and phenotype severity, elucidate the molecular mechanism behind aortic root aneurysms, and discover the usefulness of angiotensin II type 1 receptor (AT_1) blockers such as the pharmaceutical drug Losartan in MFS treatment.

Losartan is an antihypertensive drug that prevents progressive aortic dilation likely by inhibiting transforming growth factor-β (TGF-β) activity, which is dysregulated in MFS [11], [12].

While histology can be used to visualize the microstructure and study changes in a localized area of the heart, it cannot easily be used to quantify the overall morphology of the heart. Histology is a 2D imaging method, and requires extensive tissue processing and slicing that can deform the heart's structure, making volumetric reconstructions of the heart inaccurate, laborious, and expensive.

Structural phenotyping can be useful in the study of a diseases' pathogenesis as changes in cardiac morphology often occur as a result of ventricular remodeling. Ventricular remodeling can be defined as an adaptive mechanism in response to changes in hemodynamic stress or the ability to deal with that stress [13]. While the change is originally compensatory in nature, designed to maintain or improve cardiac function, ventricular remodeling can eventually lead to cardiac dysfunction. Proper functioning of the heart requires both adequate force development and deformation. These two factors are dependent on both internal factors such as the heart geometry and the mechanical properties of the wall, as well as external factors such as hemodynamic stress. Changes to any of these parameters, such as heart geometry, can lead to cardiac dysfunction.

In Marfan syndrome, primary cardiomyopathy is a controversial finding [14]. In the human, some studies have found evidence of biventricular dilation in the absence of valvular disorders, while others have found mild dilation that is insufficient to cause dysfunction [15]–[18]. In the mice, cardiovascular phenotyping in vivo has been challenging due to the small size and fast heart rate of the murine heart. Consequently, detailed mice heart phenotyping is performed ex vivo. The following section gives a brief overview of the different modalities used for murine cardiac imaging.

1.1. Overview of Mouse Cardiac Imaging Modalities

Cardiac imaging in mice is challenging due to their small heart size (0.2 g) and fast heart rate (500-650 bpm). Common modalities used to image the murine heart include ultrasound (US), cardiac magnetic resonance imaging (CMR), and micro computed tomography (μCT).

Ultrasound is the preferred imaging modality for *in vivo* functional imaging due to its high temporal resolution; however, conventional ultrasound systems (7.5-15 MHz) have low spatial resolution, typically on the order of hundreds of microns. Ultra-high-frequency ultrasound systems (20 – 55 MHz) that offer higher spatial resolution (50-100 µm) are available; however, they have limited depth of penetration, around 5-8 mm, which is insufficient for imaging adult mouse hearts *in vivo* [19]. While this depth of penetration may be sufficient for *ex vivo* cardiac imaging, the spatial resolution may not be sufficient for detecting small differences in morphology. Research on cardiac dysfunction in humans has suggested that US might not be sensitive enough to detect small differences in cardiac dimensions: evidence of dilated cardiomyopathy was detectable using CMR, but not US [15], [16], [18], [20].

CMR and µCT are also used for *in vivo* imaging. In contrast to ultrasound, depth of penetration is not an issue. Instead, the trade-off is between spatial resolution and acquisition time. Although they have longer acquisition times, they are able to generate three-dimensional images of the murine heart at different points in the cardiac cycle through the application of gating techniques. However, both CMR and µCT suffer from poor signal to noise, low spatial resolution, and high imaging costs. Small animal MRI machines at 1.5T to 14T can cost $1 million to $6 million, whereas a small-animal µCT machine costs approximately $250,000-$500,000 [21]–[24]. Instead of owning a machine, many MRI and µCT facilities will lend their machines for data acquisition at a per-hour cost of $200-350 for MRI and $60 to $250 for µCT [25]–[27]. While these techniques can also be applied to *ex vivo* imaging of murine hearts with higher resolution and sensitivity, it is at the cost of longer acquisition times, which hampers its usefulness in studying cardiac dynamics at high resolution. Thus, there is a need for a cost-effective imaging modality that can image the murine heart with both high temporal and spatial resolution.

Optical coherence tomography is a non- contact imaging modality that acquires depth-resolved, cross-sectional images with high spatial and temporal resolution [28]. Similar to ultrasound, depth is determined based on the 'time-of-flight' of back-scattered pulses. However, since the speed of light is orders of magnitude faster than the speed of sound, the 'time-of-flight' of light cannot be measured directly, but is instead probed using low coherence interferometry. In cardiac tissue, OCT can achieve a depth penetration of up to 1 mm in atrial tissue and 2 mm in ventricular tissue, and can resolve small structures such as the electrical conduction system, coronary vasculature, and the myocardial fiber orientation over depth.

The advantage of using OCT for morphological phenotyping is that it can provide high-resolution (~10 µm) images with high sensitivity without requiring any tissue sectioning or exogenous contrast agents. OCT systems are also much cheaper than CMR or µCT: the cost of a commercial OCT system is approximately $60,000. However, there are currently no commercial OCT systems available to image the mouse heart due to its unique challenges. Given the size of an adult murine heart, the depth of penetration in OCT is a limiting factor. The average adult mouse heart is approximately 1.5 cm in diameter, with an average left ventricular wall thickness of 1.5 mm [29]. Since the depth of penetration in OCT is 1 to 2 mm, the adult murine heart cannot be fully imaged using conventional approaches. This thesis describes our approach in overcoming this depth limitation to image the whole heart, and developing a tool for studying cardiovascular diseases such as MFS.

1.2. Overview of Thesis

The goals of this thesis are to develop OCT for murine heart imaging, and to apply tools from computational anatomy on the OCT volumes to quantify and compare the cardiac morphology between wild-type mice and a mouse model of Marfan syndrome.

Before describing our approach, a brief background on cardiac anatomy and Marfan syndrome is first presented in Chapter 2. Chapter 3 describes the design of the imaging system and our image acquisition protocol, while Chapter 4 describes the processing steps required to yield a single volume of the whole heart using OCT. Chapter 5 describes the various morphological parameters that were extracted from these volumes. Chapter 6 presents the results of a preliminary study comparing the cardiac morphology of wild-type and Marfan mice, and Chapter 7 concludes the thesis with a discussion of our current results and limitations, and presents some potential future work.

Chapter 2.   Cardiovascular Complications in Marfan Syndrome

Marfan syndrome (MFS) is an autosomal dominant connective tissue disorder that affects 2-3 people in every 10,000 [1], [2]. Its prevalence has been hard to describe accurately due to difficulties in determining a proper diagnosis protocol. Part of the difficulty in determining a proper diagnosis is the genotypic and phenotypic variability inherent in MFS: more than 800 genetic mutations have been discovered in MFS [30]. Phenotypically, variations in the clinical manifestations have been found both between and within families [31].

MFS is caused by any number of mutations to the *FBN1* gene that encodes the matrix protein fibrillin-1 and results in fibrillin-1 deficiency [32], [33]. Fibrillin-1 is a primary component of the microfibril, which is present in the extracellular matrix and forms a scaffold on which elastin and myofibrils grow on. A deficiency of fibrillin-1 could cause elastic fiber disarray and lead to weakness and decreased elasticity of connective tissue. However, the primarily structural role of fibrillin-1 deficiency failed to explain many of the symptoms of MFS [3].

Studies using mouse models of MFS have elucidated a regulatory role of fibrillin-1 in transforming growth factor beta (TGF-β) protein signaling [11], [34], a cytokine that is important in regulating cellular proliferation and differentiation. Fibrillin-1 binds to TGF-β and keeps it sequestered. A haploinsufficiency of fibrillin-1 results in increased TGF-β signaling which leads to degeneration of the components within the extracellular matrix [34]–[36].

In the heart, increased TGF-β signaling has been associated with aortic stiffening, which plays a role in aneurysm formation and increases the susceptibility to dissection [10]. While the aortic complications are the most life-threatening, the other cardiovascular symptoms, such as pulmonary artery dilation and mitral valve prolapse, also have a negative impact on cardiac function. Since connective tissue is integral in the architecture of the myocardium, MFS can also impair myocardial function and result in ventricular dilation; however, this finding is still debatable. Clinical studies using CMR, but not ultrasound, on a small population of Marfan patients found mild but significant systolic dysfunction and dilated cardiomyopathy in the

absence of valvular regurgitation [14]–[18]. Transgenic mouse models can be used to study the impact of MFS on cardiac morphology. However, the cardiac morphology of transgenic mouse models is also not well characterized.

In this section, I will first briefly describe the relevant cardiac anatomy and the impact of morphology on proper cardiac functioning. I will then highlight some key differences between the anatomy of the human and mouse heart. I will end the section by describing the transgenic mouse model of MFS that we used in our study comparing wild-type and MFS mouse hearts, and our hypothesis on the change in cardiac morphology.

2.1. Cardiac Structure

The heart is a muscular organ that is responsible for transporting nutrients and waste throughout the body by circulating blood with enough pressure to perfuse the organs and tissues. It is anchored to the middle mediastinum of the thorax by the pericardium, a fibro-serous, fluid-filled sac. The pericardium consists of two portions: the fibrous pericardium and the serous pericardium. The outermost layer, the fibrous layer, is a thick, inelastic layer that anchors the heart to the thorax via its attachments to the diaphragm, aorta, and pulmonary trunk. In contrast, the serous portion consists of two thinner layers, the parietal and visceral pericardia, which border the pericardial cavity and secrete serous fluid. The serous fluid in the cavity is important for minimizing friction and limiting excessive motion between the heart and the thoracic cavity.

Structurally, the heart consists of 4 chambers: 2 atria and 2 ventricles. The atria serve as reservoirs, collecting blood from the rest of the body to the heart, while the ventricles function as pumps that propel blood from the heart to the rest of the body. Figure 2-1 below presents a diagram of the basic structure of the heart and depicts the relative locations of the atria and ventricles.
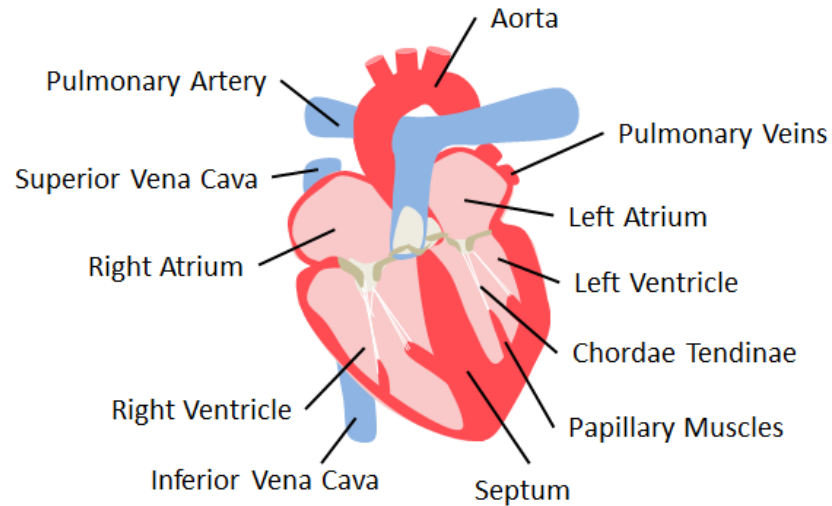
Figure 2-1: Major components of the heart. The blood vessels that service the right side of the heart have been shown in blue, while the blood vessels that service the left side of the heart have been shown in red.

The right side of the heart is responsible for pumping deoxygenated blood to the lungs (pulmonary circulation), while the left side is responsible for pumping oxygenated blood from the lungs to the rest of the body (systemic circulation). Deoxygenated blood enters the right atrium from the superior and inferior vena cava and travels to the right ventricle. The right ventricle pumps the blood through the pulmonary arteries to the lungs, where the blood gets oxygenated. Oxygenated blood returns from the lung through the pulmonary veins to the left atrium and then travels to the left ventricles. The blood is pumped by the left ventricle to the aorta, which distributes the oxygenated blood to the rest of the body. The volume of blood ejected by the left ventricle per minute is referred to as the cardiac output. During each cardiac cycle, an electrical excitation starts at the right atrium and travels to the left atrium, which signals to atria to contract. After a delay, the excitation travels down the septum to the apex of the ventricles, and then to the wall of both ventricles, where it signals the ventricular contract. Atrial contraction precedes ventricular contraction to allow time for blood for fill the ventricles before the blood is pumped to the lungs and body, respectively.

Within the heart, there are four valves that ensure one-way flow of blood. Two of these valves, the atrioventricular valves, are located between the atria and ventricles. These atrioventricular valves are connected to papillary muscles located on the ventricular surface by fibrous chords, the chordae tendinae, which prevent backflow of blood from the ventricles to the

atria. The papillary muscles contract simultaneously with the ventricles to prevent the valves from folding back into the atria.

The two other valves, the semilunar valves, are located at the entrances of the pulmonary artery and aorta and prevent backflow from these arteries back into the ventricles. These valves consist of three crescent-shaped cusps that attach to the arterial wall and project into the lumen of the artery. Due to their shape, these valves open when blood flows from the ventricles to their respective arteries, but close when blood flows in a retrograde manner.

2.1.1. Layers of the Heart

The heart wall consists of three layers: the epicardium, endocardium, and myocardium. Figure 2-2 illustrates the relative location of the layers from a cross-section of the heart wall. It also shows the local coordinate system that we will use in this section. The transverse axis is parallel to the surface of the heart, the radial axis denotes the transmural direction, and the longitudinal axis is parallel to the long axis of the heart.
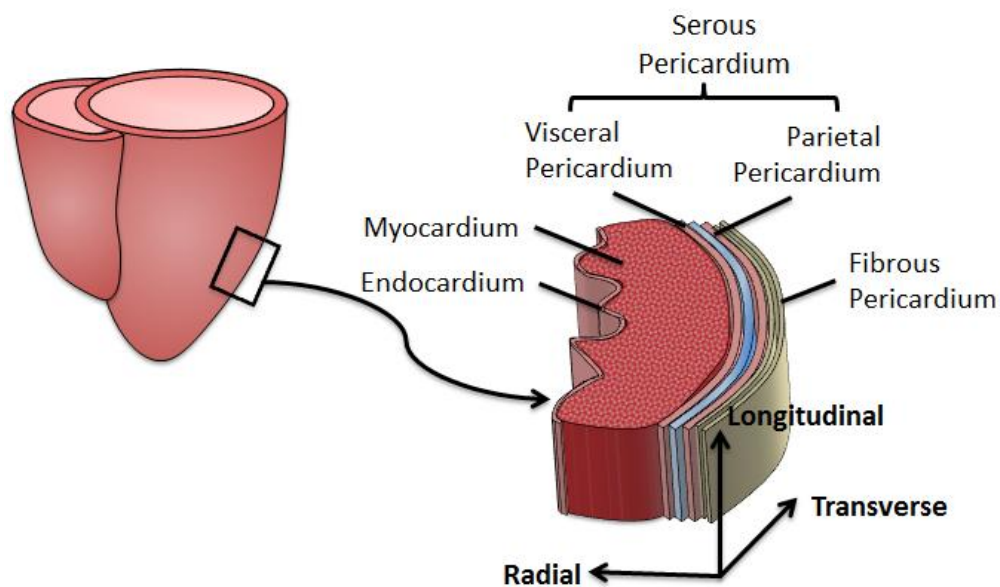
Figure 2-2: Diagram showing layers of the heart wall. Ventricular wall of heart consists of primarily myocardium, bounded by endocardium and pericardium. The pericardium consists of two portions: the fibrous and serous pericardium. The serous pericardium consists of two layers that border the pericardial cavity. Arrows show local coordinate system.

The epicardium, also known as the visceral pericardium, lines the outer surface of the heart and serves to protect the heart and reduce friction from relative movement between the heart and thorax. The endocardium lines the inner surface of the heart, forming the valves and covering the trabeculae carnae. The endocardium also helps modulate myocardial contractility.

The myocardium forms the bulk of the heart, and is responsible for the pumping mechanism. It is composed of myocytes that are approximately 50-100 µm in length and 10 - 15 µm in diameter [37]. These myocytes are joined end-to-end by intercalated discs that bind the myocytes together and transmit mechanical force through the myocytes, thereby allowing the myocytes to contract as a synctium. These intercalated discs also contain gap junctions that that function to transmit electrical impulses between myocytes. The myocytes are embedded in an interstitium that contains collagenous fibers along with other cells such as fibroblasts and microfibrils. These collagenous fibers form a meshwork that surround both individual myocytes and groups of myocytes and provide architectural support.

Myocytes are arranged in a laminar structure, with approximately 4 myocytes per layer. The fiber layers are joined to adjacent layers through branching, with perimysial collagen fibers located between the fibers. These fiber layers rotate counterclockwise from epi- to endo- cardial surface. The muscle layers also run in discrete layers longitudinally in a radial direction [38], [39].

The cleavage planes between the layers allow slippage between the myocytes to accommodate the changes in volume and wall thickness that accompany the cardiac cycle [37]. These cleavage planes are oriented parallel to the fiber orientation. When viewed along the transverse axis, such that the heart is sliced parallel to the surface of the heart, the cleavage planes rotate counterclockwise from the epicardial to endocardial surface. In contrast, within a longitudinal cross-section, the cleavage planes are oriented radially [38]. Figure 2-3 shows the fiber orientation and cleavage planes in the right ventricular free wall of a murine heart, as visualized using optical coherence tomography (OCT).
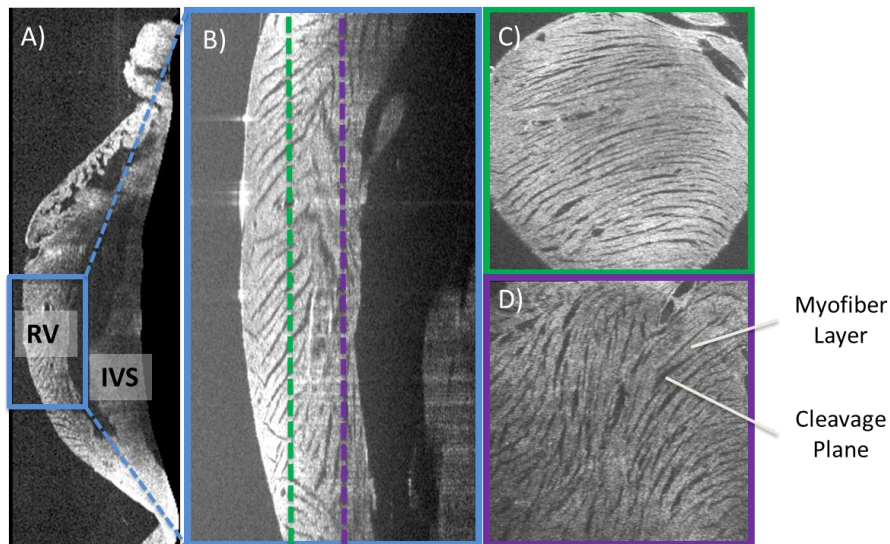
Figure 2-3: Orientation of cleavage planes within the right ventricular free wall. A) Cross-section of right ventricular free wall and inter-ventricular septum. B) Zoomed-in high-resolution longitudinal cross-section of right ventricular free wall showing radial alignment of fibers. Dashed lines show depth at which transverse slices were taken. C) Transverse slice taken from epicardial surface. D) Transverse slice from endocardial surface. C) and D) show transmural variation in fiber angle.

Globally, these layers join to form helices that gradually convert from a left-handed helix in the endocardial region to a right-handed helix in the epicardial layer. Figure 2-4 presents a schematic that depicts the global orientation of the fibers in the epicardial and endocardial layers.
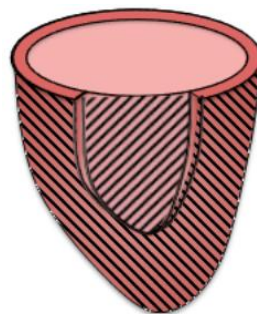
Figure 2-4: Global Organization of fibers within the left ventricle. The fiber orientation gradually changes from a left-handed helix in the sub-epicardial surface to a right-handed helix in the sub-endocardial surface.

2.1.2. Importance of the Fiber Orientation

The fiber orientation in the heart plays an important role in cardiac functioning. Locally, myocytes shorten along their longitudinal axis as they contract. Groups of myocytes oriented in the same direction will generate more stress than if they were disarrayed. Regionally, the transmural rotation of fiber increases systolic efficiency. The contraction of the epicardial fibers causes shearing and cross-fiber shortening in the endocardial surface, which results in thickening of the wall during systole, thereby increasing the amount of ejected blood [40].

The global orientation of the muscle fibers is also important for proper systolic and diastolic function. Not much is known about the relation between the global orientation and functioning in the right ventricle. Instead, most studies have focused on the relation in the left ventricle. In the left ventricle, the right-hand helix in the epicardium causes the base of the left ventricle to rotate clockwise, as viewed from the apex, and the apex to rotate counterclockwise. Conversely, the contraction in the endocardium results in counterclockwise rotation of the base and clockwise rotation of the apex. When both the epicardial and endocardial fibers contract, the rotation from the epicardial fibers dominates as it has a greater mechanical advantage. Figure 2-5 shows the fiber orientation in the epicardial and endocardial layer of the left ventricle, and the direction in which they would cause the ventricle to twist.
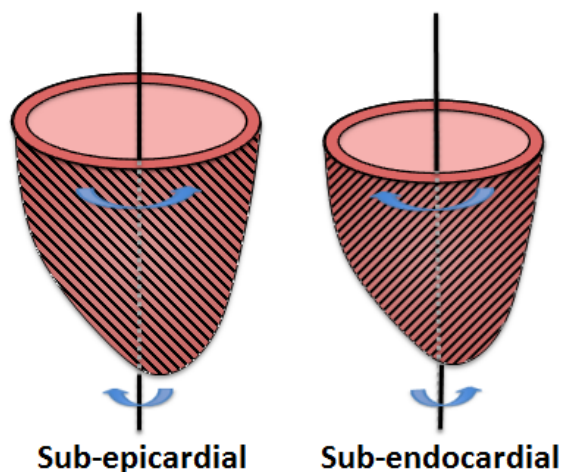
Figure 2-5: Twist in left ventricle caused by global fiber orientation. Arrows depict the direction of rotation with contraction. Contraction in the sub-epicardial and sub-endocardial region results in opposing force development and rotation.

Ventricular contraction starts at the sub-endocardial surface of the heart, where it results in a slight 'unwinding', with the apex rotating clockwise and the base rotating counterclockwise. Since the fibers in the endocardial and epicardial surface are oriented perpendicularly, endocardial contraction results in stretching of the fibers on the epicardial surface. This mechanical stretch is important as it increases contractility.

As the excitation travels transmurally from the endocardial to the epicardial surface, the epicardial contraction eventually overweighs the endocardial rotation, and the left ventricle rotates clockwise at the base and counterclockwise at the apex, resulting in a twisting motion that 'wrings' blood from the ventricle. The twisting and shearing in the endocardial surfaces also aids in diastolic relaxation by storing potential energy in the form of elastic recoil [41].

A final important function of the myofibril orientation is the distribution of stress: the torsion created by the fiber orientation results in a more uniform distribution of stress and shortening across the wall, thereby increasing systolic efficiency [42].

2.2. Motivation for Studying Cardiac Morphology

The impact of myofibril orientation on proper systolic and diastolic function was described in the previous section. The gross morphology of the heart is also an important determinant of cardiac functioning. Proper cardiac functioning depends on both appropriate filling of the ventricles, as well as the generation of sufficient pressure and deformation to overcome arterial blood pressure and eject blood out of the ventricles. The regional wall stress, which affects the amount of deformation and pressure that can be generated, is dependent on the thickness of the myocardial wall or heart geometry, as described by the law of Laplace, which is

2-1

$$\sigma = \frac{PR}{2T},$$

where σ is the wall stress, P is the ventricular pressure, R is the radius of the lumen, and T the wall thickness. Changes in morphology can occur as a result of abnormal hemodynamic stress, or impaired ability to deal with the stress. These changes are initially compensatory response designed to maintain cardiac output [13], [43]. However, chronic remodeling can lead to

irreversible changes in the myocardium and result in cardiac dysfunction. To illustrate this concept, the pathological adaptation to chronic preload due to mitral regurgitation is described.

Preload is the stretch on the ventricular myocytes prior to contraction. As the stretch on individual myocytes is difficult to measure directly, preload is usually calculated as the product of the volume of blood in the ventricles and the pressure that volume exerts on the ventricular walls prior to contraction. During Mitral Regurgitation (MR), the valve does not fully close during contraction, and some of the ejected blood flows retrogradely back to the left atria. This regurgitant volume decreases the net volume of blood ejected into the systemic circulation and increases the volume of blood present in the next cardiac cycle. In other words, cardiac output in decreased, while preload is increased.

In acute MR, the increased stretch on the heart from the increased preload results in a myogenic increase in contractile strength which serves to help maintain cardiac output. However, with chronic MR, the heart cannot increase contractility to compensate the increased preload, and cardiac output decreases. To accommodate the increased preload, the ventricular lumen size increases. The increase in lumen size, called dilation, allows the heart to increase the volume of blood ejected each beat without an increase in contractility or stress to the myocytes. While this adaptation allows the heart to regain near-normal cardiac output, eventually, the progressive dilation results in increased wall compliance, increased wall stress, and decreased contractility. The mal-adaptation results in decreased cardiac output [44]. Thus, while the adaptation (left ventricular dilation) originally occurred to maintain cardiac output despite increasing preload, progressive adaptation eventually lead to compromised cardiac functioning.

2.3. Difference in human and murine cardiac anatomy

Although the mammalian heart shares many similarities across the different species, there are structural differences that are important to note when using murine hearts to study human cardiac conditions.

One obvious difference in the murine and human heart is its size: the murine heart is considerably smaller than the human heart. The human heart weighs approximately 250-350 g

and beats approximately 60-70 times per minute, while the mouse heart weight approximately 0.2 g and beats 500-600 times per minute [29], [45].

The shape of the heart between the mouse and human differs, due to the difference in how the heart rests inside the thoracic cavity [45]. Since humans stand upright, the heart rests on the diaphragm, and has a flattened inferior surface, making it more pyramidal in shape. In contrast, the mouse stands on four legs and the heart does not rest on the diaphragm; thus, the murine heart is more ellipsoidal in shape. Within the heart, the distribution of the right and left ventricle differs. Figure 2-6 illustrates the difference in ventricular shape between the human and mouse heart.
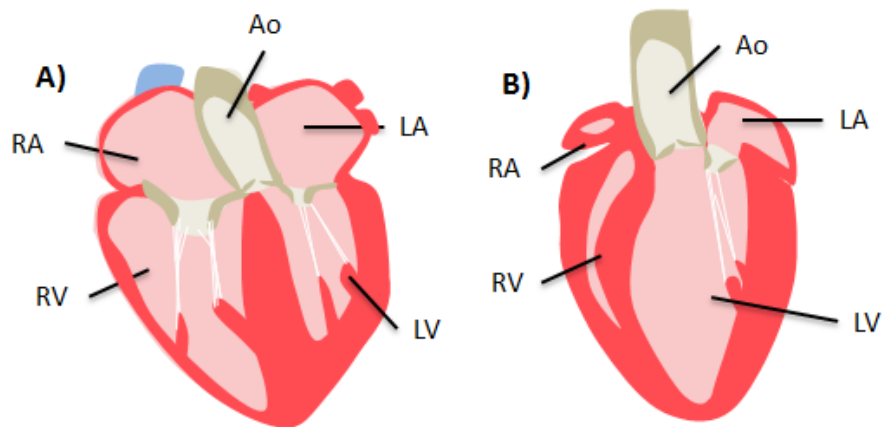
Figure 2-6: Comparison of the structure of the human heart (A) and mouse heart (B). The mouse heart Ao, aorta; LA, left atrium; LV, left ventricle; RA, right atrium; RV, right ventricle.

In both the mice and human, the left ventricle is more dominant and has a thicker wall than the right ventricle since it needs to eject blood against a greater pressure. However, comparing the shape of the right ventricle, the right ventricle in the mouse is smaller than the human and has a more crescent shape.

The veins and arteries that supply the heart also differ between the mouse and human. In the human, only two veins supply de-oxygenated blood to the right atrium, the superior and inferior vena cava. In contrast, the mouse exhibits three vena cava: two cranial vena cava and one caudal cava. For blood supply into the left atrium, four pulmonary veins arise from the lungs and independently join the atrium, whereas in the mouse heart, the pulmonary veins join to a solitary vein that connects to the left atrium [45].

Finally, the interior of the ventricular surface of the mouse and human heart also differ. The murine heart contains numerous protusions, called trabeculae carnae, in both the right and left ventricles. In contrast, in the human ventricles, the trabeculae carnae in the right ventricle are much coarser than the trabeculae in the left ventricle [45].

2.4. Effect of MFS on Murine Cardiac Morphology

Many transgenic mouse models have been developed to study the origin and progression of MFS. For our preliminary study comparing the morphology of wild-type and Marfan mice, we used a well-established mouse model that contained a heterozygous mutation of fibrillin-1 (C1039G) [46].

Using ultrasound, CMR, and histology, the effects of fibrillin-1 mutation on the aortic dimensions and aortic wall composition has been characterized [9]–[11]. However, similar characterizations of the gross cardiac morphology of the different transgenic mouse models have not been made: there is only one study on the effect of MFS murine mutation on cardiac morphology. This study found dilated cardiomyopathy (DCM) in a mouse model of severe MFS, $Fbn1^{mgR/mgR}$ in which mgR is a hypomorphic mutation that results in decreased production of FBN1 [47]. They also found the DCM phenotype in the absence of valvular conditions or any other common clinical cardiac manifestations of MFS and concluded that DCM seems to be a primary manifestation in MSF [47]. We expect to have milder, but similar, findings with our heterozygous mouse model of MFS.

The effect of MFS on myofibril orientation is also not well characterized in either the murine or human case; indeed, only one documented case has been reported in the human [48]. As MFS results in a deficiency of fibrillin-1, which serves as a scaffold for other products within connective tissue, it is possible that MFS can cause myofibrillar disarray. Another goal of this thesis is to develop the tools needed to investigate myofibrillar disarray in Marfan mice.

2.5. Summary

In this section, we provided a background into cardiac anatomy and Marfan syndrome. We also briefly described the research on cardiac dysfunction in Marfan syndrome and our motivation for studying cardiac morphology. To study the effect of MFS on myofibril orientation

and heart structure, we propose the use of a high-resolution imaging modality called optical coherence tomography (OCT). However, imaging murine hearts with OCT presents some unique challenges. In the next chapter, the challenges of imaging murine hearts, along with our approach to resolving these issues are described. We also outline the considerations that went into the design of our hardware acquisition system and described our imaging system and protocol.

Chapter 3.   Optical System Background and Design

Morphological phenotyping is important for characterizing and studying diseases. However, cardiovascular imaging in mice has been hampered by the mouse's small heart size and fast heart rate. To resolve small changes in cardiac morphology, an imaging modality with high spatial resolution is required.

Optical coherence tomography (OCT) is capable of providing depth-resolved images of structures with near-histological resolution (1 – 10 µm). Unlike CMR or ultrasound, light has a very limited tissue penetration depth due to absorption and scattering. Using near-infrared light, which is in the tissue optical window, OCT has a depth of penetration of up to 1-2 mm in cardiac tissue. However, this limited depth of penetration is not sufficient for cardiac imaging of mice. The size of an adult mouse heart is typically 7-10 mm in diameter, with an average left ventricular wall thickness of 1.5 to 1.8 mm [1,2]. Thus, conventional OCT imaging alone is not able to image the full mouse heart. To improve the depth of penetration, optical clearing agents such as glycerol can be used.

In this chapter, we first describe the theory behind optical coherence tomography and optical clearing before going into the considerations into the design of our imaging system and the imaging acquisition protocol on ex vivo mouse hearts.

3.1. Background of Optical Coherence Tomography

Optical coherence tomography (OCT) is a high-resolution, depth-resolved imaging modality that is based on the principles of low coherence interferometry. A schematic of a generic OCT system in a Michelson interferometer topology is presented Figure 3-1.
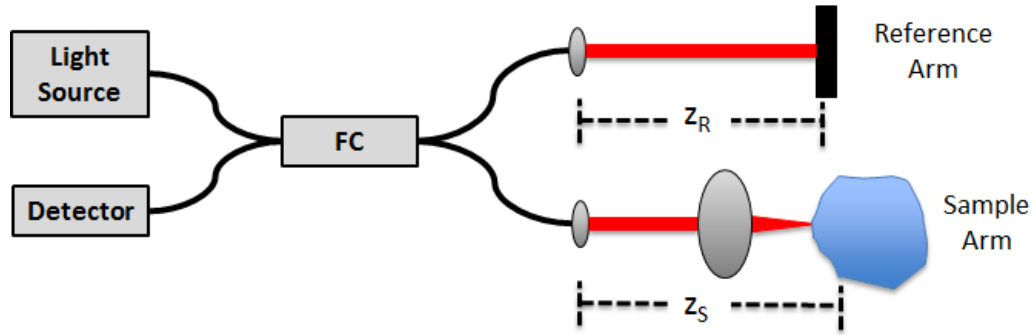
Figure 3-1: Fiber-based Michelson interferometer. OCT uses principles from low coherence interferometry to extract the relative depth, z_S-z_R, of the sample reflectors from the back-scattered light.

Light is coupled into a fiber coupler that splits light into two arms: a reference arm and a sample arm. Light reflected from the reference and sample arms are combined at the fiber coupler, where they interfere to produce a fringe frequency with intensity

3-1

$$I_D(k) = I_R + I_S + \sqrt{I_R I_S} \cos(2\Delta zk),$$

that is proportional to the optical path length mismatch, $\Delta z = z_R - z_{Si}$ where z_R is the optical path length of the reference arm, and z_{Si} are the path lengths from the multiple reflections of the sample. I_R and I_S are the intensities of the reflections from the reference and sample arms respectively. This interference fringe pattern is detected, digitized, and read into the computer, which converts the fringes into depth-resolved images by using the discrete Fourier transform (DFT).

In OCT, a tomographical volume is acquired by laterally scanning the beam in 2D across the sample. A depth profile taken at a single location in space is called an a-scan. A b-scan is a 2-dimensional image formed by laterally scanning the beam in one direction and concatenating the a-scans acquired at the different locations. A volumetric image is formed by concatenating a series of b-scans. Finally, an en-face view is formed by summing up all the intensities for each a-scan. The relationship between a-scan, b-scan and volumes is presented in Figure 3-2.
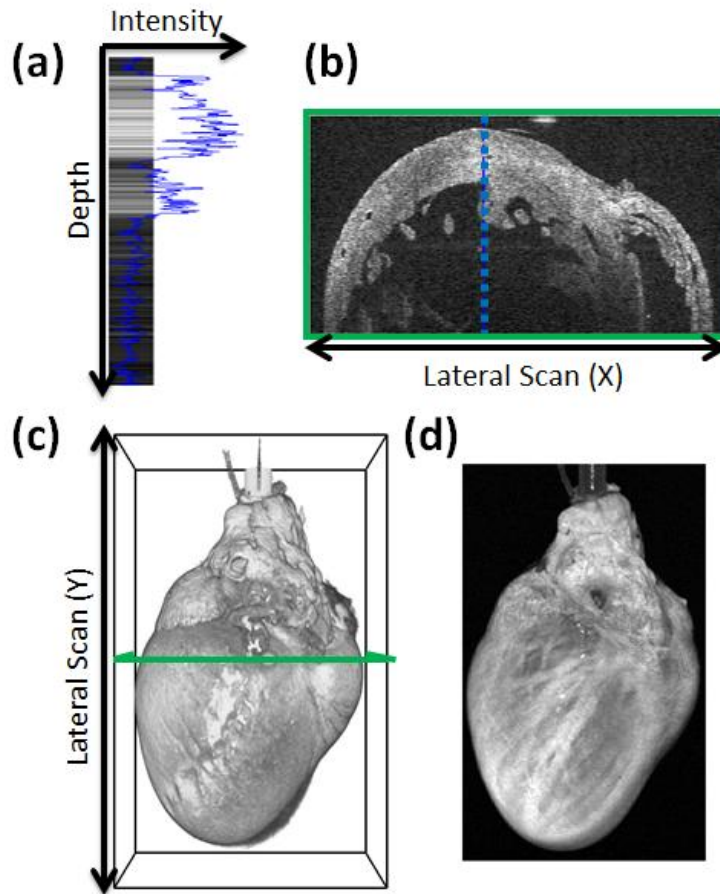
Figure 3-2: Scanning schemes and terminology in OCT. A) Representative a-scan. B) Representative B-scan. C) Volumetric rendering. D) En-face View.

From the data set, slow-axis scans and C-scans can also be extracted, as shown in Figure 3-3. A slow-axis scan is a scan taken perpendicular to the b-scan, which shows the lateral y-scan at a single x position. A c-scan is an image acquired at a single depth.
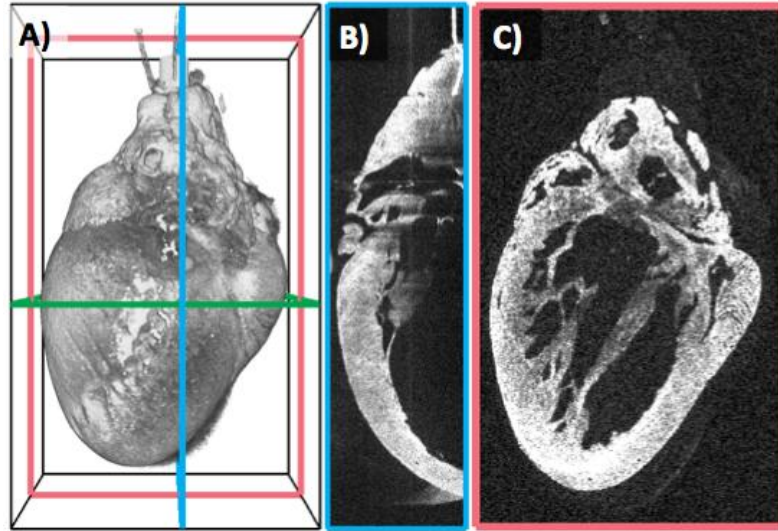
Figure 3-3: Scan Terminology for OCT. A) Volumetric rendering of data show location and orientation of slices relative to b-scan (in green). B) Slow-axis scan. C) C-scan.

3.1.1. Mathematical description of OCT

This section provides the mathematics that describes the interferometric signal acquired at the detector, and how the interference fringe relates to the optical path length mismatch. The mathematics in the section closely follows published work by J. Izatt and M. Choma [49].

Mathematically, the electric field of a light wave can be represented as:

3-2

$$E = Re\{E_o e^{i(kz-\omega t)}\}$$

where $k = 2\pi/\lambda$ is the wavenumber, and ω is the frequency. The light wave incident on the fiber coupler from the light source can be modeled as:

3-3

$$E_o = s(k,\omega)e^{i(kz-\omega t)},$$

where $s(k,\omega)$ is the light source spectrum. Assuming that the fiber coupler splits light evenly, the light reflected from the reference and sample arms can be modeled as:

$$E_R = \frac{E_o}{\sqrt{2}}\sqrt{r_R}e^{i2kz_R} \text{ and } E_S = \frac{E_o}{\sqrt{2}}\sum_{n=1}^{N}\sqrt{r_{sN}}e^{i2kz_{sN}}.$$

where E_R and E_S are the electromagnetic waves from the reference and sample arms respectively, r_R is the reflectivity of the reference arm, and $r_{S1}, r_{S2}, \dots . r_{Sn}$ be the reflectivities of the sample at depths $z_{S1}, z_{S2}, \dots z_{SN}$.

The multiple back-reflections from the sample and reference arms combine at the coupler to produce an interference fringe whose intensity can be determine using

3-5

$$I_T(k) = \langle |E_R + E_S|^2\rangle = \langle (E_R + E_S)(E_R + E_S)^*\rangle.$$

Since the fiber coupler attenuates half of the combined light, the light intensity incident on the detector is:

3-6

$$I_D(k) = \frac{\rho}{2}I_T(k),$$

where ρ is the detector responsivity. Combining Equations 3-3 to 3-6 yields:

$$I_D(k) = \frac{\rho}{4}\left\{S(k)\left[R_R + \sum_{n=1}^{N}R_{sn}\right]\right\} \qquad \text{DC Term}$$

$$+ \frac{\rho}{2}\left\{S(k)\sum_{n=1}^{N}\sqrt{R_R R_{sn}}\cos(2k(z_R - z_{sn}))\right\} \qquad \text{Cross-Correlation Term} \qquad \textbf{3-7}$$

$$+ \frac{\rho}{4}\left\{S(k)\sum_{n\neq m=1}^{N}\sqrt{R_{sn}R_{sm}}\cos(2k(z_{sn} - z_{sm}))\right\} \qquad \text{Auto-Correlation Term}$$

where $S(k) = |s(k,\omega)|^2$ is the power spectrum of the source. The above Equation has three terms:

1) A 'DC' term that is a path length-independent offset that is equivalent to the source spectrum scaled by the reflectivities within the system.

2) A "cross-correlation' term that is due to the interference between reference and sample reflections.

3) An "auto-correlation" term that is due to mutual interference between the multiple reflections off the sample.

Comparing Equations 3-1 and 3-7, we see that Equation 3-1 holds true in the case of a solitary reflector in the sample arm where:

3-8

$$I_R = \frac{\rho}{4} S(k) R_R,$$

3-9

$$I_S = \frac{\rho}{4} S(k) R_R,$$

3-10

$$\text{and } \Delta z = z_R - z_{S1}.$$

To extract depth-resolved data from Equation 3-7 the following Fourier property can be used:

3-11

$$\cos(2kz_R) \overset{\mathcal{F}}{\leftrightarrow} \frac{1}{2}[\delta(z - z_R) + \delta(z + z_R)].$$

Applying the Fourier transform to Equation 3-7 yields:

3-12

$$I_D(z) = \frac{\rho}{8}\{\gamma(z)[R_R + \sum_{n=1}^{N} R_{sn}]\} + \frac{\rho}{4}\{\gamma(z) \otimes \sum_{n=1}^{N} \sqrt{R_R R_{sn}} \delta(z \pm 2(z_R - z_{sn}))\} +$$
$$\frac{\rho}{8}\{\gamma(z) \otimes \sum_{n\backslash \neq m=1}^{N} \sqrt{R_{sn} R_{sm}} \delta(z \pm 2(z_{sn} - z_{sm}))\}.$$

where $\gamma(z) \overset{\mathcal{F}}{\leftrightarrow} S(k)$. From the above Equation, we see that the bandwidth of $S(k)$ determines the axial resolution of the imaging system: a larger spectral bandwidth results in a smaller coherence length, or axial resolution. If the source spectrum $S(k)$ has a Gaussian shape, then the axial resolution of the system can be calculated using:

$$l_c = \frac{2\sqrt{\ln(2)}}{\Delta k} = \frac{2\ln(2)}{\pi}\frac{\lambda_o^2}{\Delta\lambda} \ ,$$

where λ_o is the central wavelength of the spectral source, and Δk and $\Delta\lambda$ are the spectral bandwidths of *S(k)* in wavenumber and wavelength units respectively [49]. Thus, the axial resolution in OCT is decoupled from the system optics. Instead, the sample arm optics only determines the transverse resolution and depth of focus of the OCT system.

3.1.2.   OCT Modalities

From Equations 3-7 and 3-12, the interferogram must be acquired in either z-space or k-space in order to extract the depth-resolved images. Figure 3-4 provides a schematic of the three basic types of OCT systems.
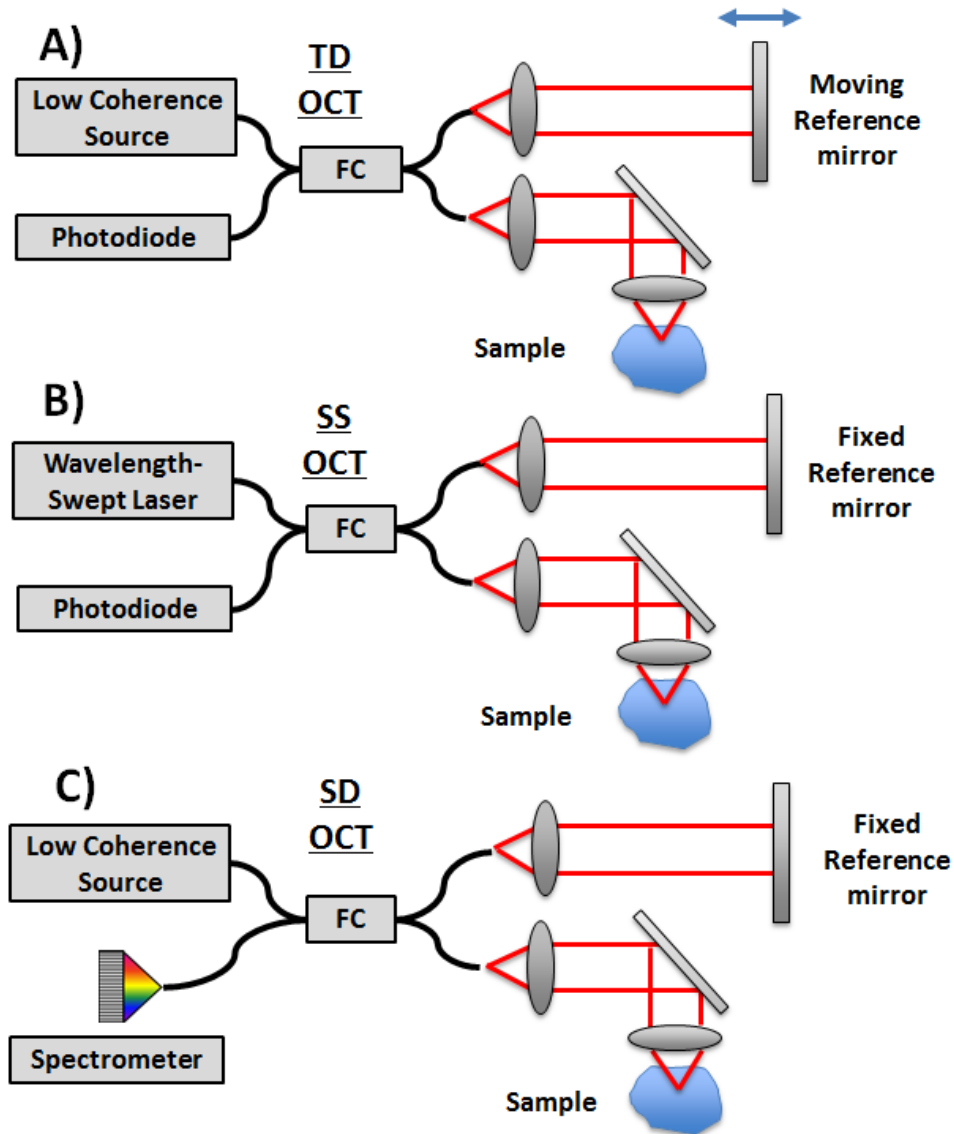
Figure 3-4: Basic Schematic of Difference OCT Systems. A) Time-domain system (TD-OCT). B) Swept-source system (SS-OCT). C) Spectral domain system (SD-OCT). TD-OCT systems acquire data from different depths by moving the reference mirror. SS-OCT and SD-OCT systems acquire data from different depths by spectrally resolving the data, and thus employ a fixed reference arm. SS-OCT uses a wavelength-swept laser and captures the different wavelengths over time, whereas SD-OCT disperses light from a broadband light source using a spectrometer.

Time-domain optical coherence tomography (TD-OCT) systems acquire data in z-space. Since interference only occurs when the path length mismatch is within the coherence length of the source, the reference arm must be translated axially in order to acquire fringes from different depths. The need for physical translation of the reference arm limits the imaging speed and signal-to-noise ratio of TD-OCT.

In contrast to time-domain based system, Fourier domain systems make use of k-space sampling to acquire depth-resolved information. Fourier domain systems do not require mechanical translation of the reference arm; instead, interference from path length mismatches that are larger than the coherence length is resolvable by acquiring the spectral content of the interferogram. Due to the elimination of mechanical translation, Fourier domain systems can achieve higher imaging speeds and sensitivity than time-based systems.

There are two main Fourier-domain imaging methods: Swept-Source optical coherence tomography (SS-OCT) and Spectral Domain optical coherence tomography (SD-OCT).   These two methods differ in their method of dividing the interferogram in k-space. SS-OCT encodes the spectral content in time by utilizing a wavelength-swept laser. The intensity of the interference fringe at each wavelength is then detected using a simple photodiode detector. In contrast, SD-OCT encodes the spectral content in space by utilizing a spectrometer as a detector. The light source for an SD-OCT is a broad bandwidth, low-coherence, light source. As the focus of this thesis was in the development of a mouse imaging modality using SS-OCT, the rest of this discussion will focus on SS-OCT.

3.2. Swept Source Optical Coherence Tomography

The basic components used in a swept-source OCT system are the wavelength-swept laser and the photodiode detector. Wavelength-swept lasers sweep through a bandwidth of wavelengths over time, emitting a narrow-bandwidth light at a single point in time. The bandwidth of light emitted at a single point in time is referred to as the linewidth and determines the sensitivity roll-off. The depth at which the sensitivity is 6dB lower than the maximum can be calculating using

3-14

$$\hat{z}_{6dB} = \frac{2\ln(2)}{\delta_r k} = \frac{\ln(2)}{\pi}\frac{\lambda_o^2}{\delta_r \lambda},$$

where $\delta_r k$ and $\delta_r \lambda$ are the linewidths of the source in wavenumber and wavelength units respectively [49].

Since the spectral data is encoded in time, the phase of the interferference fringe from each spectral component can be detected using a simple photodiode detector. For improved

25

detection, a balanced photodiode detector can be used to reject the DC and auto-correlation components of the interferogram. Two balanced configurations for SS-OCT have been provided in Figure 3-5.
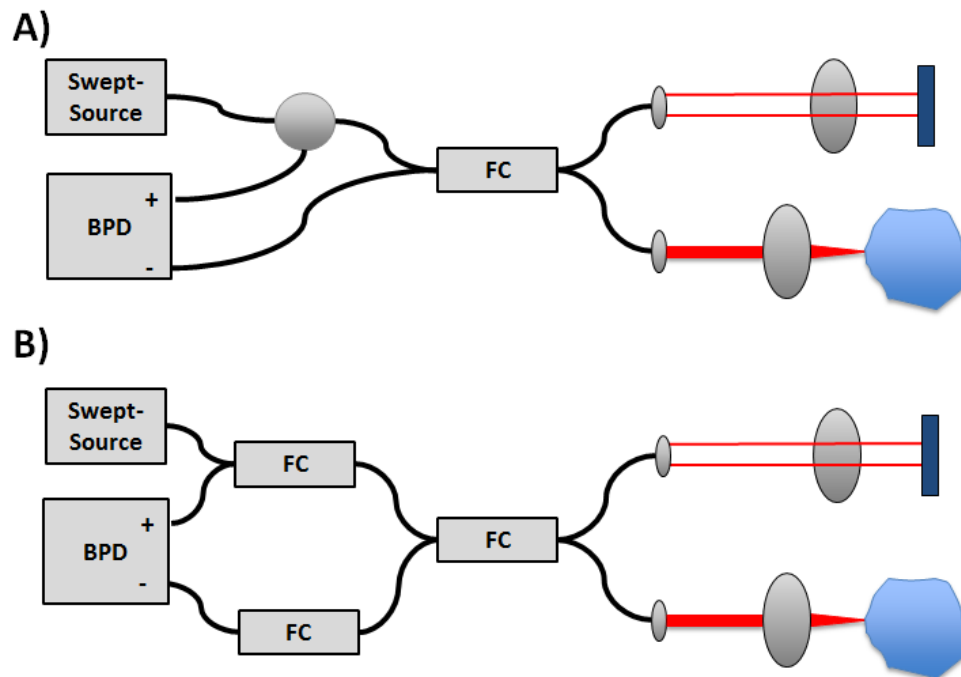
Figure 3-5: Balanced detection schemes for SS-OCT systems. A) Balanced circulator design. B) Balanced three-coupler design.

Balanced detection can be achieved through the addition of a circulator prior to the fiber coupler that only allows one-directional flow of light (Figure 3-5a). However, circulators are not optimized for all wavelengths. Commercially available circulators at 1060 nm, for example, have narrower bandwidths than the available light sources, and thus change the spectral shape, which affect the point-spread-function (PSF) of the imaging system and decreases the axial resolution. The uneven splitting also decreases the bandwidth of the interfered spectrum and therefore results in PFS broadening.

The three-coupler design in Figure 3-5b has the potential to minimize the problems associated with the uneven splitting and narrower bandwidth of commercially available circulators. The uneven splitting is minimized through the use of wavelength-flattened couplers. Although the three-coupler design does attenuate the power incident on the sample arm, it allows for greater interference between the sample and reference arms and provides greater axial resolution.

3.2.1. SS-OCT Processing

After detecting and digitizing the interferogram, the computer must process the raw data to yield the depth-resolved data. From Equations 3-7 and 3-12, the main processing step is the computation of the discrete Fourier transform (DFT). Prior to computing the DFT, however, there are pre-processing steps that must be taken into consideration, including DC subtraction and resampling.

Although the use of a balanced detection scheme minimizes the DC component of the interferogram, in practice, it is never completely eliminated. The residual DC component can be recorded by either blocking the sample arm, or by averaging multiple a-scans acquired from different locations. If the a-scans are not spatially correlated, the cross-correlation component of the fringe will get averaged out, leaving the DC component.

Another step in pre-preprocessing is resampling. Although the wavelength-swept laser encodes the spectral content in time, it does not do so in a linear fashion. To convert the acquired data from time to wavenumber, a pixel clock is required. A pixel clock is an interferometer with fixed path length. From Equation 3-1, the peaks and zero-crossings of the interference fringe are equidistant in k-space and can be used as a calibration signal. This calibration signal can be applied in post-processing, using software resampling methods, or in hardware, as a sample clock during the digitization.

After preprocessing, the data is then converted from wavenumber to depth through the DFT. One consequence of the k-space digitization and DFT calculation is that the maximum imaging depth is limited by aliasing. The maximum imaging depth is related to the k-space sampling rate by

3-15

$$z_{max} = \frac{\pi}{2 * \delta_s k} = \frac{\lambda_o^2}{4\delta_s \lambda},$$

where $\delta_s k$ and $\delta_s \lambda$ are the sampling periods in wavenumber and wavelength units respectively [49].

3.2.2. Sensitivity of SS-OCT

For OCT, the shot noise limit determines the maximum sensitivity of the system. Mathematically, the sensitivity of the system, SNR, can be determined using

3-16

$$SNR = \frac{\rho P R_s \Delta t}{2e}$$

where ρ is the detector sensitivity, P is the power incident on the sample, R_s is the reflectivity of the sample, Δt is the line integration time, and e is the electronic charge [50]. For SS-OCT, Δt is inversely related to the a-scan rate of the system . That is,

3-17

$$\Delta t = \frac{1}{f_{Ascan}},$$

where f_{Ascan} is the a-scan repetition rate. Thus, a faster a-scan rate decreases the maximum sensitivity of the system.

The above SNR equation assumes shot noise-limited detection. Although the equation does not explicitly include the reference arm power, it is an important factor for sensitivity. For maximum sensitivity, the reference arm power should be approximately one order of magnitude greater than the sample arm power. Increasing the reference arm power will cause photon noise to dominate, whereas decreasing the reference arm power will cause receiver noise to dominate.

Another important benefit of making the reference reflectivity dominate the sample reflectivities is to minimize auto-correlation artifacts. From Equation 3-7, the cross-correlation component is dependent on the product of the reference and sample arm reflectivities, whereas the auto-correlation component is only dependent on the sample arm reflectivities. Proper tuning of the reference reflectivity can ensure that the cross-correlation component dominates the detected signal [49].

3.3. Optical Design Parameters

In designing a system to image the mouse heart, we first need to consider the dimensions of our sample. The size of an adult mouse heart is typically 7-10 mm in diameter, with an average left ventricular wall thickness of 1.5 to 1.8 mm and right ventricular wall thickness of 0.5-0.6 mm. To image the full heart in a single acquisition, the imaging modality would need to have a depth of penetration of at least 3.5 mm in tissue with a depth of focus on the order of centimeters. However, the depth of penetration of near-infrared light is limited to a couple of millimeters. With this depth of penetration, we would not be able to visualize any structures on the interior of the ventricular lumen, nor would we be able to visualize the interventricular septum.

Another challenge in imaging the heart is its dimension. To image the heart in a single acquisition, a depth of focus on the order of centimeters is required. Due to the trade-off between depth of focus and lateral resolution, imaging the heart in a single shot would only be possible with a low-resolution system. For example, using Gaussian optics, the relationship between lateral resolution and depth of focus is:

3-18

$$DOF = 2z_R = 2\frac{\pi\omega_o^2}{\lambda}$$

where z_R is the Rayleigh range, DOF is the depth of focus, and ω_o is the radius of the focused beam spot size. From Equation 3-18, a system with a depth of focus of 1.5 cm would have a lateral resolution of $2\omega_o = 100\ \mu m$. With this low resolution, the advantages of moving to an optics-based modality would be outweighed by its limitations.

Due to the limited depth of penetration of light and the heart dimension, we chose to image the heart from multiple perspectives and then apply image registration and stitching techniques to acquire a volumetric image of the whole heart. By imaging the heart from multiple perspectives, the depth of focus and imaging depth can be decreased to half the heart diameter. Moreover, as the heart is mainly a hollow structure bordered by a thick wall, the depth of focus can be decreased to be on the order of its thickest portion, which is approximately 1.5 – 1.8 mm. Finally, prior to imaging, the heart is fixed using paraformaldehyde, which can shrink the tissue [51]. Thus, we decided to set the depth of focus to be 1 – 1.5 mm. In contrast to the depth of focus, the spatial resolution determines the sensitivity of the imaging system in detecting

changes in morphology. For example, to resolve a 5% change in wall thickness, a spatial resolution of approximately 25 μm is required (for a wall thickness of 0.5 m). A schematic of the resulting system that fulfills the design parameters above is presented in Figure 3-6.
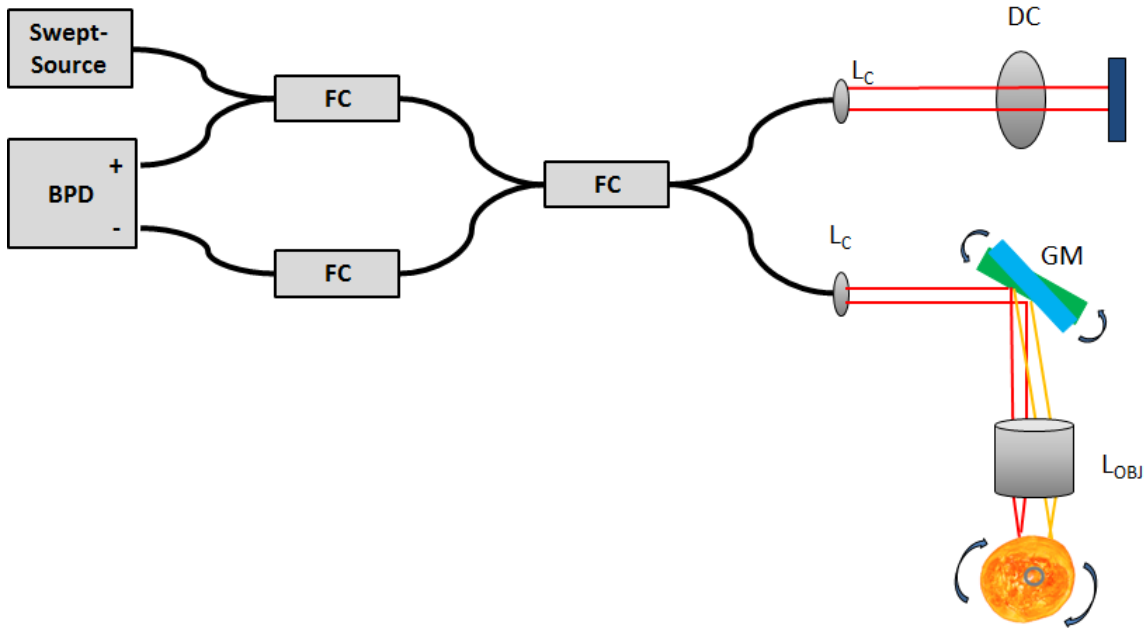
Figure 3-6: Schematic of OCT acquisition system. DC, dispersion compensator; FC, fiber coupler, GM, galvanometer scanning mirrors, L_{OBJ}, objective lens, L_C, collimating lens.

For the light source, we used a commercial swept-source engine (Axsun Technologies, MA) that had a center wavelength of 1060 nm and an effective 3 dB bandwidth of 85 nm. Thus, our theoretical axial resolution was 7 μm in air. The sample arm consisted of two lenses: an achromatic collimating lens (L_C = 10 mm) and a 3x OCT telecentric scan lens (L_{OBJ} =54 mm). The transverse resolution and depth of focus of the system was 30 μm and 1.34 mm respectively. These components were chosen based on the availability of lenses and a desired beam waist of approximately 25 μm.

To determine the spatial resolution of the system, we first considered the size of the collimated beam entering the objective lens. The size of the collimated beam is determined by the numerical aperture (NA) of the single-mode fiber (NA = 0.12) and the focal length of the collimating lens. Using standard trigonometry, the collimated beam waist was determined to be 1.2mm. From the collimated beam waist, the size of the focused beam waist was then determined using:

$$\omega_f = \frac{\lambda f_{OBJ}}{\pi \omega_c},$$

where ω_f and ω_c are the radii of the focused and collimated beam respectively.

Using this SS-OCT system, we acquired data from multiple perspectives of the heart. The heart was rotated relative to the static sample arm. To improve the match between the volumes from different perspectives, and improve the quantitative accuracy of our result, we minimize geometrical distortions by employing a telecentric lens in our setup. The following two sections provide a background into the telecentric lens, and describe the design of our rotation device. s

3.3.1.   Background on use of a Telecentric Lens

A telecentric lens was employed as the objective lens to minimize geometric distortions. Reduction of geometric distortions is important to increase the match between the volumes acquired from different perspectives, and to increase the accuracy of the quantitative analyses. Figure 3-7 shows a comparison of different types of scanning lens.
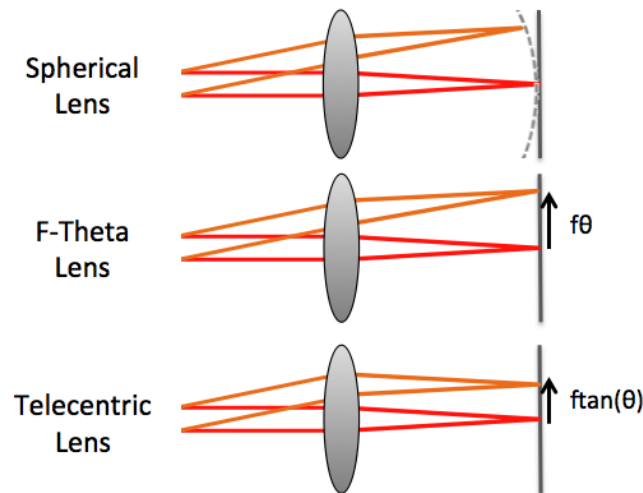
Figure 3-7: Comparison of scanning distortion in regular and telecentric scan lens. Telecentric lens remove both radial and field curvature aberrations that are associated with spherical lens. f, focal length of the lens; θ, angle of beam entering the lens.

A standard lens exhibits both radial and field curvature aberrations. When used as a scanning lens, the field curvature distortion results in non-uniform focus spot, whereas the radial distortion results in a pincushion-like distortion. F-theta scanning lenses minimize the field curvature distortion but still exhibit slight radial distortion, as the displacement of the beam is linear with θ. In contrast to the above lenses, telecentric lenses remove both field curvature and radial distortions by focusing light on a flat plane, and displacing the beam linearly.

A disadvantage of using a telecentric lens is its loss in power. The telecentric lens that we employed (LSM04-BB, Thorlabs, NJ) attenuated the incident power by 2.5 dB, whereas a similar-focal-length achromatic lens attenuated the power by 0.35 dB. From Equation 3-17, the power incident on the sample is linearly proportional to the maximum sensitivity of the system. Thus, using a telecentric lens instead of a simple achromatic lens will decrease our maximum achievable SNR.

3.3.2. Design of the Rotation Mount

To perform multi-perspective imaging, the heart was first attached to a needle. The needle was secured within the lumen of the aorta. The heart was then attached to the rotation device via the needle. The components included in the rotation device are shown in Figure 3-8.
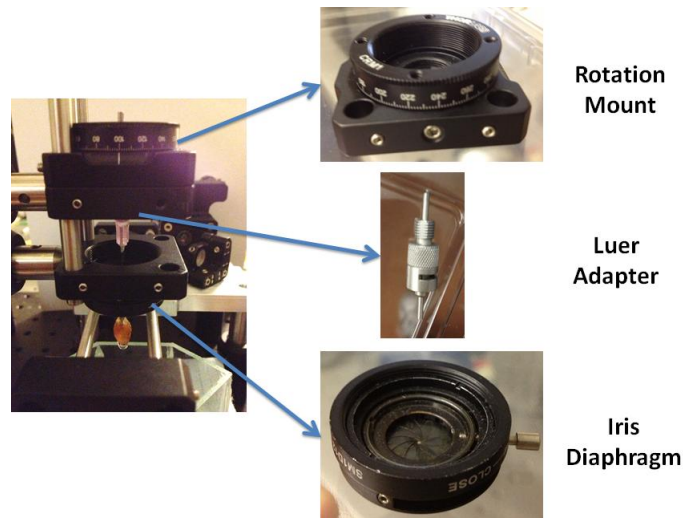
Figure 3-8: Components included in the rotation device. The graduated rotation mount, luer adapter, and iris diaphragm were mounted to Thorlabs' cage system for increased stability.

To minimize possible tissue deformation due to gravity, we designed the rotation mount to ensure that there was minimal wobble in the needle with rotation. Cage-mounted components were used to ensure that the needle hung vertically, and that the mount was stable with rotation. The rotation mount had 2° graduations, which allowed the user to rotate the heart with a precision of 1°. A luer-to-thread adapter was connected to the rotation mount using a suitable SM1-to-thread adapter. The final part of the assembly was an iris diaphragm, whose function was to minimize the wobble within the needle. The rotation mount was then connected to a three-axis translation stage for easy alignment of the heart relative to the imaging optics.

This rotation mount allowed us to rotate and image the heart from multiple perspectives, thus decreasing our required depth of focus and imaging depth. However, due to the thickness of the mouse heart, the limited penetration depth of OCT still presents a challenge in imaging mouse hearts.   The following section describes the method by which we increased the penetration depth.

3.4. Sample Preparation and Acquisition Protocol

To improve depth of penetration, we immersed the fixed hearts in glycerol. Glycerol is a hyperosmotic agent that clears tissue by synergistic actions of dehydration and refractive-index matching [52]. The effect of glycerol on decreasing the opacity of tissue is demonstrated in Figure 3-9.
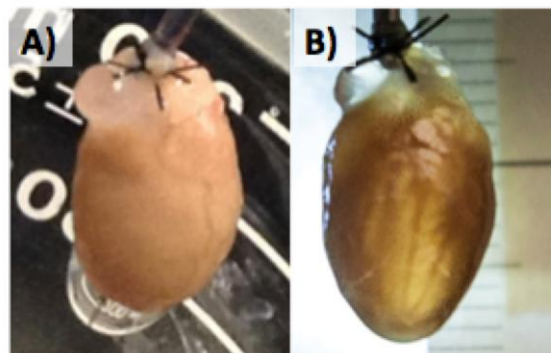
Figure 3-9: White-light photograph of a fixed heart before (A) and after (B) tissue clearing with glycerol. Optical clearing causes the heart to become more translucent. The ruler has been placed behind the cleared heart to show relative size.

The refractive index matching decreases the effective scattering coefficient, thereby resulting in an increased penetration depth (Figure 3-10). The top row displays the effect of glycerol on representative b-scans, whereas the bottom row displays the effect on c-scans.
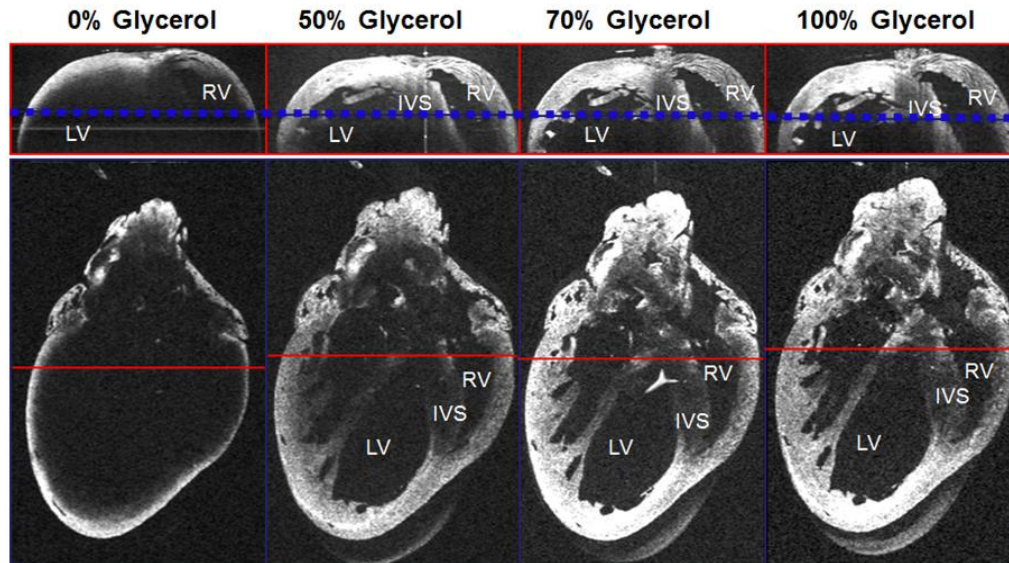
Figure 3-10: Comparison of OCT penetration depth at difference glycerol concentrations. Hearts were cleared at different glycerol concentrations and then imaged using OCT. Stronger glycerol concentrations results in increased penetration depth.

Glycerol clearing improves depth of penetration. Without clearing, the OCT beam is unable to penetrate the left ventricle. However, with the addition of glycerol, OCT is fully able to penetrate the left ventricular wall, and the structures on the endocardial surface become apparent. Increasing the glycerol concentration increases depth of penetration but also decreases scattering and therefore OCT contrast. We chose to use 70% glycerol as we found it to be a good compromise between depth of penetration and contrast.

The hearts were cleared under a graded protocol, at 50% glycerol and 70% glycerol for 1 day each, prior to imaging. The hearts were then mounted onto the rotation mount via its attached needle, and rotated and imaged in 30° increments, across the entire 360° span. At each rotation, 10 volumes were acquired and averaged to offset the loss in signal-to-noise from the telecentric scan lens and optical clearing. Given N volumes, and assuming that the signal and noise are uncorrelated, the SNR of the averaged image will increase by a factor of $\sqrt{N}$. After acquisition, the sub-volumes from multiple perspectives were then processed and registered to form a single volume of the whole heart.

3.5. Summary

In this section, we outlined the challenges with using optical coherence tomography for mouse heart imaging, and then described our approach to resolving these issues, including the adoption of multi-perspective imaging and optical clearing. We also described the design considerations for our optical imaging system and our imaging protocol. In the next chapter, we shall describe the processing steps required to register and stitch the volume into a volume of the full heart.

Chapter 4.   Volumetric Reconstruction of the Mouse Heart OCT Images

In the previous chapter, volumetric images of the mouse heart were acquired from multiple perspectives using optical coherence tomography (OCT). The next step is to combine these volumes taken from multiple perspectives into a single volume of the whole heart. For the remainder of this discussion, the volumes taken from different perspectives will be referred to as 'sub-volumes', whereas the volume of the whole heart will be referred to as the 'whole volume'.

Prior to registering and stitching the sub-volumes into a whole volume, distortions within the OCT volume due to the imaging process must be taken into account. In OCT, image distortions arising from nonlinear scanning distortion, non-telecentric scanning distortion, and refraction can cause registration mismatch and decrease the accuracy of the quantitative measurements [53], [54]. We minimized the scan-related distortions by using a telecentric lens as our objective lens and by considering only the linear portion of the scan in our data acquisition. However, the refractive distortion due to the difference in refractive index of air and the sample remained. To correct for refraction, the refractive index of each layer as well as the boundaries between the layers must first be determined. Since the heart was immersed in 70% glycerol prior to imaging, and glycerol permeates the tissue through passive diffusion, glycerol was assumed to be within the heart chambers as well. Given that the majority of the refraction occurs at the air to tissue interface, we chose to only correct for distortion due to refraction at the epicardial surface of the heart.

After segmenting the epicardial surface and applying refraction correction, the sub-volumes can then be registered and stitched. In this chapter, we describe our approach behind surface segmentation, refraction correction, registration, and stitching, apply this pipeline on the sub-volumes acquired from a single heart, and present the resulting volume of the whole heart.

4.1. Methods

This section describes the steps involved in our processing pipeline, namely surface segmentation, refraction correction, volumetric registration, and volumetric stitching.

4.1.1. Segmentation of the Epicardial Surface

The first step in the volume processing pipeline was the segmentation of the outer surface of the heart in preparation for refraction correction. The outermost surface of the heart was automatically segmented in 3D using a gradient-based approach. Figure 4-1 shows the result of the steps involved in the segmentation process on a single slow-axis scan.
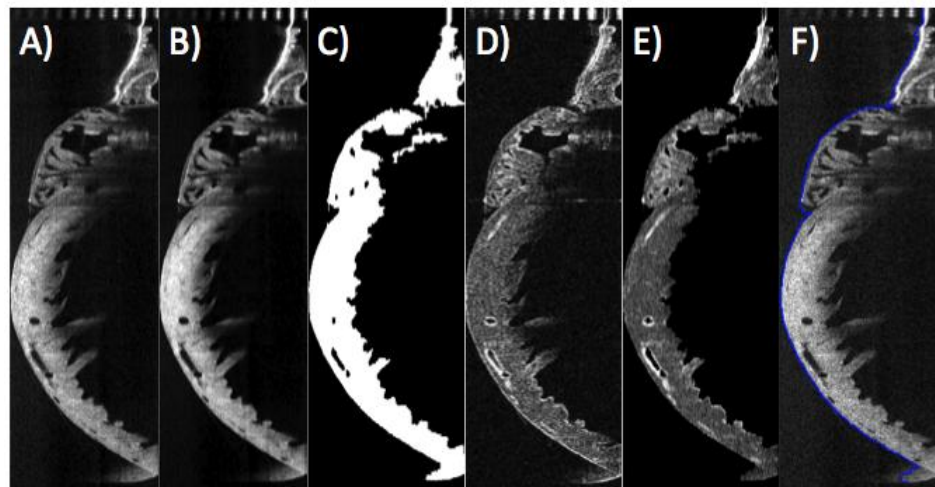
Figure 4-1: Slow-axis scan showing result of applying each step of the segmentation algorithm. A) Original Data. B) BV-smoothed image. C) Mask image. D) Gradient. E) Masked gradient. F) Segmented surface.

The volumes were first preprocessed using 3D edge-preserving BV smoothing to remove speckle noise (Figure 4-1B). The following mathematics on BV smoothing was taken from the lecture notes of Dr. Younes [55]. BV smoothing is based upon minimizing

4-1

$$E(I, I_o) = \int_\Omega |\nabla I| dx + \lambda \int_\Omega |I - I_o|^2 dx = Q(I) + \lambda C(I, I_o),$$

where I_o is the original, degraded image, I is the smoothed image, $Q(I)$ is the quality of image I, and $C(I, I_o)$ is the distance between the image I and original image I_o. $Q(I)$, the BV norm for a smooth image,

<div align="right">**4-2**</div>

$$\|I\|_{BV} = \int |\nabla I| dx,$$

represents the quality of the image. Minimizing E results in smoothing the image while enforcing a small distance between the smoothed and original image. The use of the BV-norm instead of the L2-norm helps preserve image sharpness, as the L1-norm does not penalize high-frequency content or sharp discontinuities as greatly. The discretization of the minimization of Equation 4-1 results in

<div align="right">**4-3**</div>

$$I^{n+1} = I^n + \delta t |\nabla I^n| \left(\nabla \cdot \left(\frac{\nabla I^n}{|\nabla I^n|} \right) - 2\lambda(I^n - I_o) \right),$$

where I^n is the smoothed image from the nth iteration.

Three image gradient volumes, G_x, G_y, and G_z, were calculated from the denoised volume via convolution with the appropriate 3D Sobel filter. Sobel filters involve taking the triangular difference [-1,0,1] in the primary direction, while smoothing in the two perpendicular directions. The gradient magnitude, G, was calculated for each voxel using

<div align="right">**4-4**</div>

$$G = \sqrt{G_x^2 + G_y^2 + G_z^2}$$

and masked such that only the gradient within the tissue was non-zero (Figure 4-1E). The masking volume was computed by applying morphological opening and closing on the BV-smoothed volume to remove other image artifacts, such as spots from bright back-reflections, and then applying a intensity-based global thresholding algorithm (Figure 4-1C). After masking, the topmost gradient point in each A-scan was labeled as the outermost surface (Figure 4-1F).

The segmented surface for each slow-axis scan in the volume was adjusted to ignore wrapping due to complex-conjugate artifact. Figure 4-2 shows the process by which we adjusted for the complex-conjugate artifact.
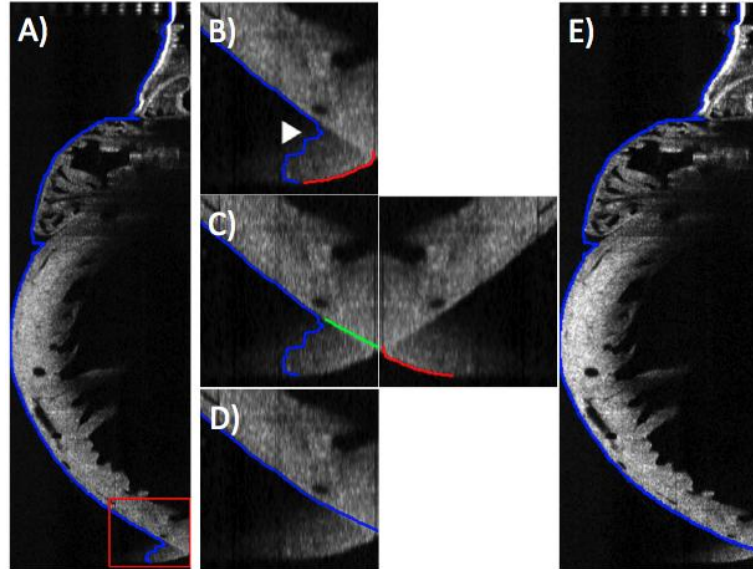
Figure 4-2: Diagram showing the adjustment of the surface segmentation result for wrapping due to complex conjugate artifact. A) Segmented surface. B) Detection of wrapped portion by finding the inflection point (white arrowhead). The bottom surface of heart is shown by the red line. C) Interpolation process to find the missing portion. The bottom surface (in red) is unwrapped, and the mission portion is interpolated (in green). D) Adjusted Result, zoomed in to the wrapped portion. E) Adjusted segmentation result.

The wrapped portion of the image was detected by taking into account the convex nature of the ventricular surface. The inflection point was detected in the segmented surface through the second derivative test (Figure 4-2B). For the portion of the image past the inflection point, the bottom surface was segmented and unwrapped, and the actual surface of the heart was estimated using interpolation (Figure 4-2C). The result of adjusting the segmented surface is shown in Figure 4-2E. This adjustment was performed on every slow-axis slice in the volume.

4.1.2.   Correction of Refractive Distortion

After determining the coordinates of the top surface, we then corrected for refractive distortions using a similar approach to previously published results [54], [56]. Refraction occurs when light is incident upon a medium with different index of refraction at an oblique angle.

Figure 4-3 depicts the bending of light when light enters a medium with a greater index of refraction.
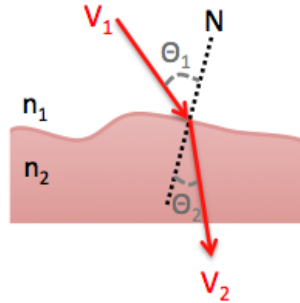
Figure 4-3: Diagram showing refraction of light. When light is incident on the sample at an oblique angle θ₁, it bends, according to Snell's law. Angles are computed relative to the surface normal.

Mathematically, the angle of refraction can be described using Snell's law, which is

4-5

$$n_1 \sin(\theta_1) = n_2 \sin(\theta_2),$$

where n_i is the refractive index of the ith material, and θ_1 and θ_2 are the angles of the incident and outgoing light. The angles are calculated relative to the surface normal. To compute the direction of the outgoing light, we implemented a vectorized version of Snell's law, which is

4-6

$$\vec{V_2} = \frac{n_1}{n_2}[\vec{N} \times (-\vec{N} \times \vec{V_1})] - \vec{N}\sqrt{1 - \left(\frac{n_1}{n_2}\right)^2 (\vec{N} \times \vec{V_1}) \cdot (\vec{N} \times \vec{V_1})},$$

where $\vec{V_1}$ and $\vec{V_2}$ are the incident and refracted rays, and $\vec{N}$ is the surface normal [54]. Since a telecentric lens was used for the objective lens, $\vec{V_1}(x, y, z) = <0,0,1>$, where z denotes depth, and x,y denotes the lateral position of each a-scan. The surface normal $\vec{N}$ was computed by taking the cross-product of the horizontal and vertical surface gradients. The length of the refracted ray (optical path length) was also scaled by the refractive index. Figure 4-4 shows the coordinate system used for the refraction correction algorithm, along with a slow-axis scan showing the effect of refraction correction.
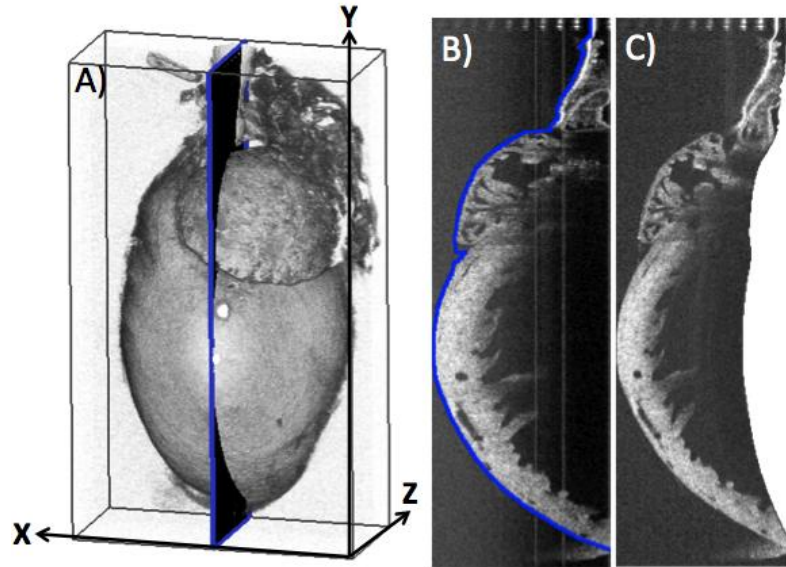
Figure 4-4: A) Coordinate system used for implementing refraction correction. B) Slow-axis of acquired volume with segmented surface. C) Slow-axis of refraction-corrected volume.

After calculating the refracted ray, the image was de-warped. For each a-scan, the position of each voxel, $\vec{V_1}(x,y,z)$, was adjusted to

4-7

$$P(x,y,z) = \begin{cases} \frac{1}{n_2}\vec{V_2}(x,y,z) & if\ \vec{V_1} > S(x,y,z) \\ \vec{V_1}(x,y,z) & otherwise \end{cases},$$

where S is the location of the segmented top surface, and P is the adjusted coordinate of the voxel. After calculating *P,* we interpolated the scattered data to find the one-to-one mapping between the refraction-correction and original volume, and applied 3D bicubic interpolation to generate the refraction-corrected volume.

4.1.3.   Volumetric Registration and Stitching

The refraction-corrected volumes were registered together to form a single volume of the whole heart. Three-dimensional rigid registration, with 6 degrees of freedom, was chosen to avoid introducing non-physical distortions from non-rigid algorithms. Registration was performed using a commercial 3D imaging analysis and processing software called Amira (FEI, France).

Although Amira cannot rigidly register multiple sub-volumes together, it can register one volume to multiple template volumes. We decided to make use of this ability to divide the registration errors across all volumes. First, the volumes acquired from 90° perspectives (at 0°, 90°, 180°, and 270°) were first pairwise registered to form the basic framework. Then, the volumes acquired at 90°, 180°, and 270° were registered to their two closest 90° neighbors. For example, the volume at 90° was registered to two template volumes: the volumes acquired at 0° and 180°. After the basic framework was determined, the remaining volumes were then registered to their two closest 90° neighbors. For example, the volume acquired at 30° was registered to the volumes acquired at 0° and 90°.

After registration, the volumes acquired from different perspectives were then stitched. Although refraction correction minimizes geometric distortion, small mismatches in the registered volumes due to residual distortions and registration errors remain. Small mismatches would result in a blurring of high frequency information when simple averaging is used to stitch the volumes. To prevent the decrease in resolution associated with averaging, we implemented a 3D version of multi-band blending, whereby lower-frequency information is averaged over a wider area [57], [58]. The following equations were adapted from an algorithm published by M .Brown and D. Lowe [58]. For a set of $i = 1 \dots N$ sub-volumes, a priority function P^i was calculated, where data with higher fidelity was given higher weight. That is, since data with the highest fidelity is near the center of the scan, where the sample surface is the most perpendicular to the imaging beam, the priority function can be calculated as

4-8

$$P^i = \frac{1}{\sqrt{(x - x_c)^2 + (y - y_c)^2}},$$

where x, y are the lateral scan positions, and x_c and y_c are the centers of the lateral scans.

A set of k = 1….n bandpass volumes were also generated using the equations

4-9

$$B^i_{(k+1)\sigma} = I^i_{k\sigma} - I^i_{(k+1)\sigma},$$

4-10

$$I^i_{(k+1)\sigma} = I^i_{k\sigma} \otimes g_{\sigma'},$$

$$and\ \sigma' = \sqrt{2k+1}\sigma,$$

where $B_{(k+1)\sigma}^i$ are the bandpass volumes and $I_{(k+1)\sigma}^i$ are the Gaussian-smoothed volumes. In this case, I_o is the original volume.

Instead of stitching all the volumes at once, the stitching was performed in an iterative fashion to better manage computer memory consumption. At each iteration, one sub-volume was added to the whole volume per iteration. The band-pass volumes were blended according to

4-12

$$T_{k\sigma}^j = B_{k\sigma}^i W_{k\sigma}^j + T_{k\sigma}^{j-1}\big(1 - W_{k\sigma}^j\big)\,j = i > 1$$

where W is the weighting function, calculated using

4-13

$$W_{(k+1)\sigma}^j = W_{k\sigma}^j \otimes g_{\sigma'},$$

4-14

$$where\ W_0^j = P^i \geq P_t^j \quad j = i > 1,$$

4-15

$$P_t^j = \max\big(P_t^{j-1}, P^{i-1}\big) \quad j = i > 1$$

The counter j marks the iteration number, whereas the counter i marks the sub-volume number. Thus, $W_{k\sigma}^2$ is the weighting function for the second iteration, when the second sub-volume is added to the whole volume. The iteration initializes at

4-16

$$T_0^1 = I_o^1$$

4-17

$$and\ P_t^1 = P^1.$$

Figure 4-5 shows the multi-band blending process for the first iteration on a representative short-axis scan, whereas Figure 4-6 shows a representative short-axis slice from the whole volume for the first 4 successive iterations.
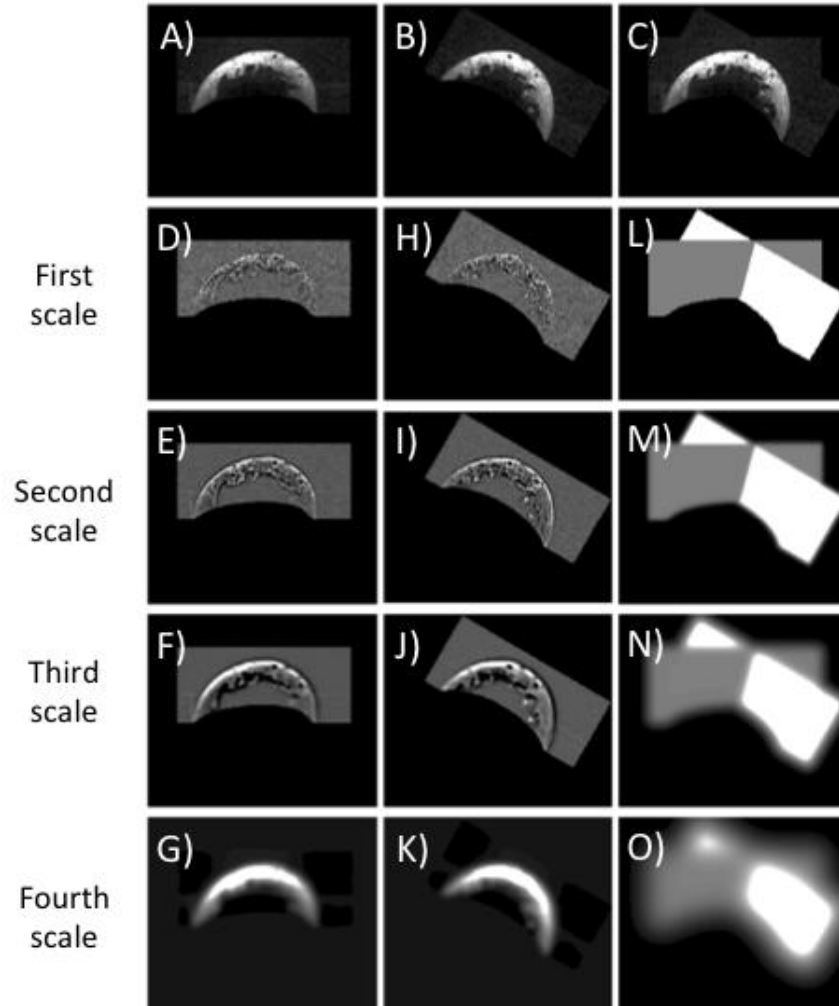
Figure 4-5: Process of multi-band blending for 2 volumes at n = 5, σ = 0.5 shown on a representative short-axis slice. (A) Slice from the whole volume, first iteration. (B) Slice from the second volume to be added. (C) Combined result. (D)-(G) show the bandpass images $T_{k\sigma}$ for k = 1,..4 for the whole volume. (H)-(K) show the bandpass images $B_{k\sigma}$ for k = 1,..4 for the second volume. (L)-(O) show the weightings used to blend the bandpass images.

Iteration #1 **Iteration #2** **Iteration #3** **Iteration #4**
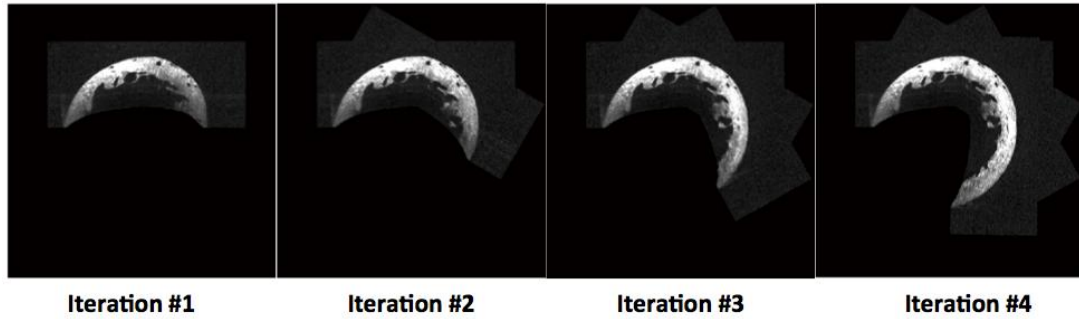
Figure 4-6: Short-axis slice from whole volume for the first 4 iterations. One sub-volume was added at each iteration.

4.2. Results

Figure 4-7 presents an OCT volume of the whole heart after refraction correction, registration, and stitching. A representative short-axis slice and 4-chamber slice from the whole volume has also been displayed. Using OCT, we were able to visualize structures within the heart such as the interventricular septum and the atrioventricular valves. Details within the left ventricular wall, such as coronary vasculature and myofibril bundles, are also visible.
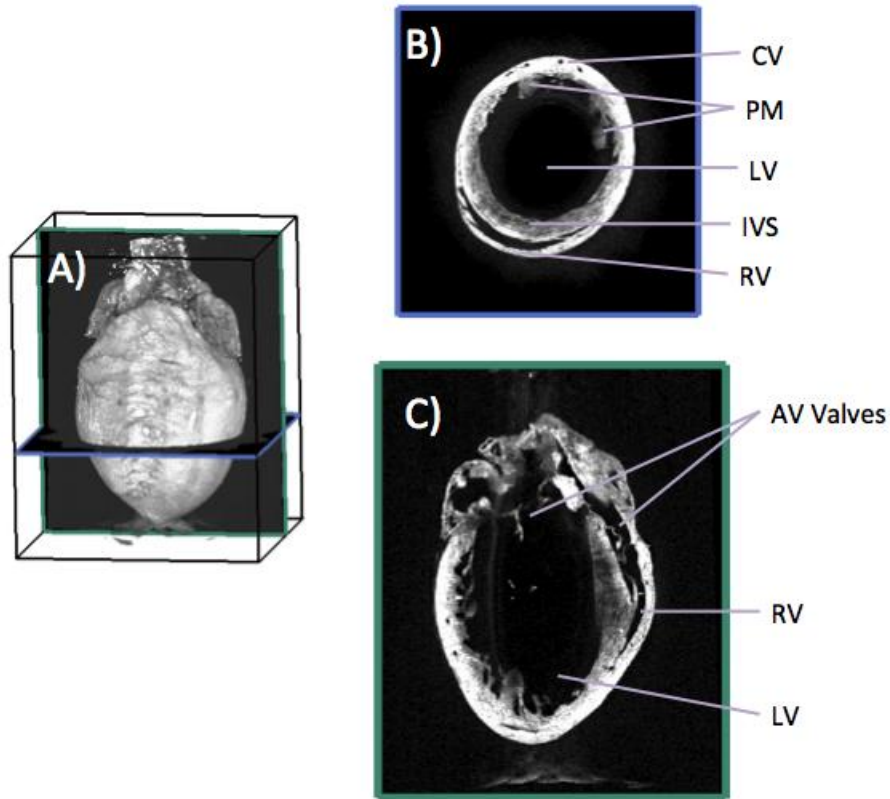
Figure 4-7: An OCT Volume of the Heart. A) Volumetric rendering of dataset showing slice locations. B) Representative short-axis slice. C) Representative slice showing 4-chamber view. AV valves, atrioventricular valves; CV, coronary vasculature; IVS, interventricular septum; LV, left ventricle; RV, right ventricle; PM, papillary muscles.

Figure 4-8 shows the contribution of each sub-volume to the final, whole volume for three representative slices. Images B-D show the stitched result, whereas images E-G show the contribution from the different volumes, where each sub-volume has been assigned a different color. Although each slice is a composite from multiple sub-volumes, registration and stitching artifacts are not easily distinguishable within the final result.
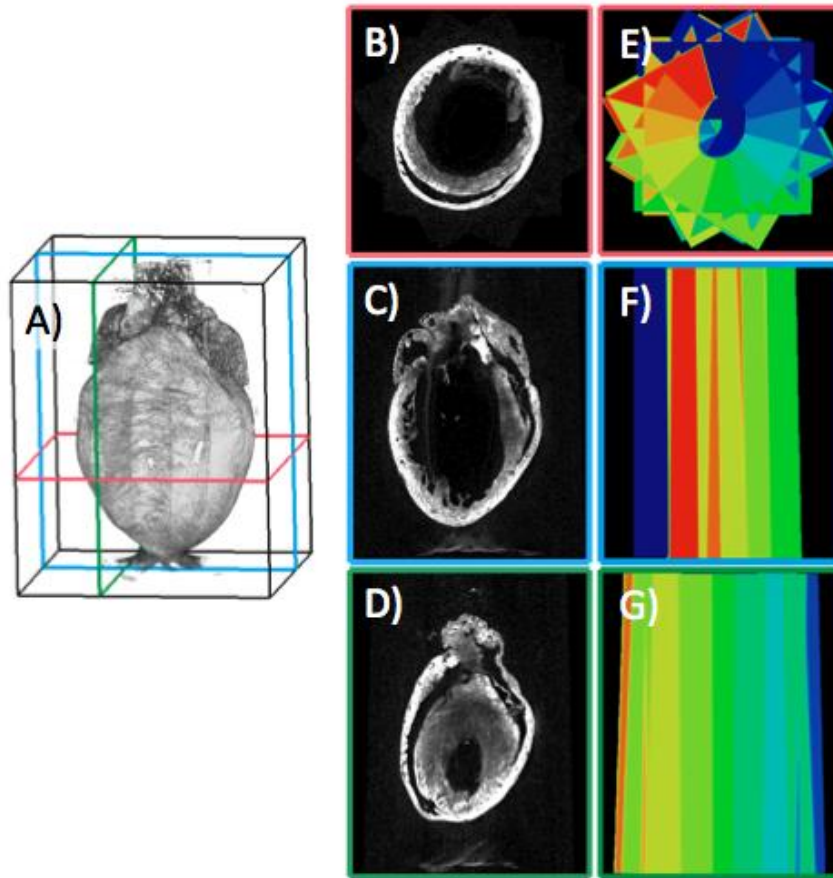
Figure 4-8: Contribution of sub-volumes to whole volume on three orthogonal slices. A) Location and orientation of slices. Slices displayed are short-axis slices (B) and two transverse slices (C,D), with the contributions from the sub-volumes given in (E,F,G).

To quantify our registration error, we analyzed the root mean squared error (RMSE) between the actual applied rotation and the registered rotation value. The mean RMSE for the 4 hearts was 0.72°±0.12°. Since the rotation mount we used to rotate the needle had a tolerance of 1°, our registered rotation agreed with the actual rotation.

Since the commercial swept-source engine we used only provided an imaging depth of 3.5 mm, our current OCT system was not able to fully image larger hearts. Figure 4-9 shows a transverse slice taken from a whole volume of a larger heart.
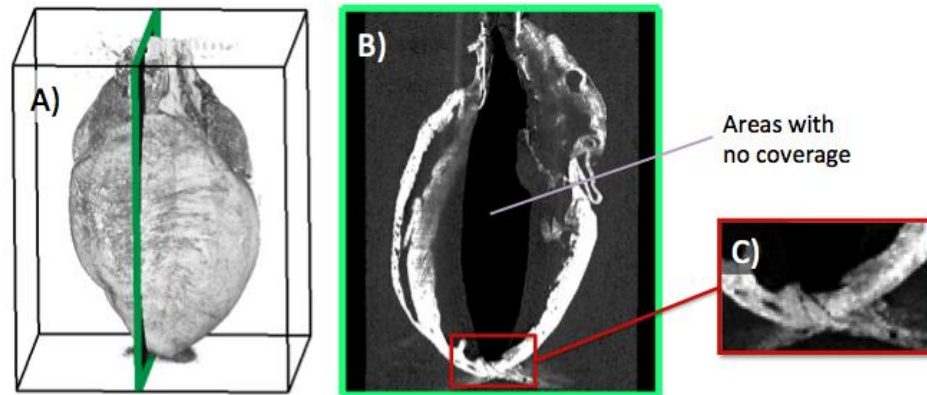
Figure 4-9: Limitations in imaging mouse hearts with current OCT system. A) Volumetric rendering of data with location of slice shown. B) Transverse slice taken near the center of the heart, showing areas that were not imaged using OCT. C) Zoomed-in image of heart apex, showing how contributions from multiple sub-volumes join to form a coherent image of the apex.

From image C, we see that multi-perspective imaging helps 'increase' our imaging depth. Referring to the apex of the heart, the entire apex is not visible from one perspective only. Instead, multiple perspectives are required to capture the entire apex. Due to the large size of some of the hearts, however, there were areas that were not captured using our OCT system. A discussion of possible solutions is provided in the last chapter of this thesis.

4.2.1.　Effect of Refraction Correction

The effect of refraction correction on the similarity of the contributions from the sub-volumes is shown in Figure 4-10, where 3 of the registered volumes have been placed in different RGB color channels. Comparing the refraction-corrected volumes (Figure 4-10D) to the non-corrected volume (Figure 4-10C), refraction correction minimizes the artifactual differences in tissue thickness with rotation, and increases the coincidence of tissue structures across the sub-volumes.
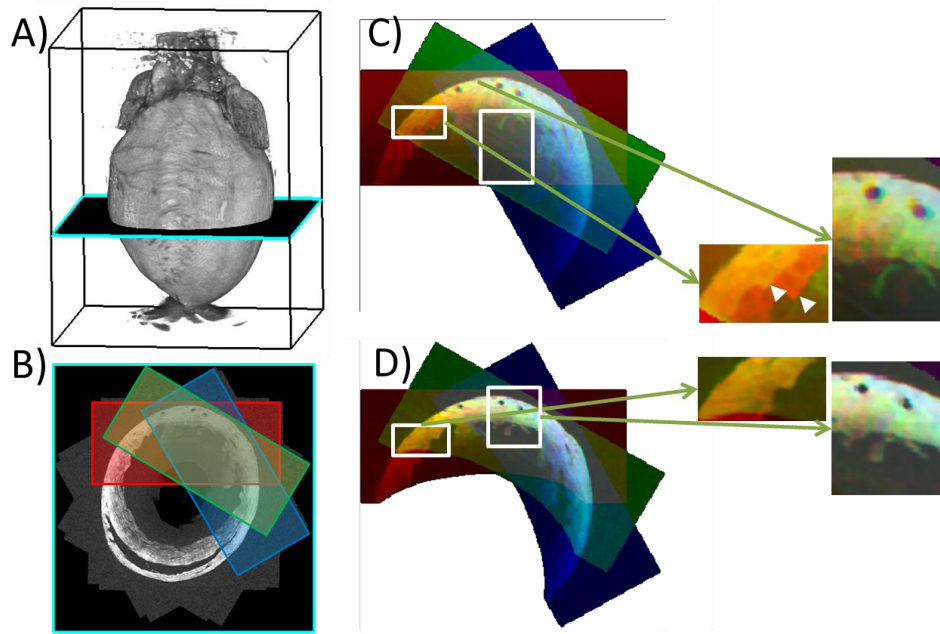
Figure 4-10: Improvement in registration match with refraction correction. A) Volumetric rending of OCT volume, showing location of short-axis slice. B) Short-axis slice from volume, showing location of three registered volumes. C) Result of registration with non-corrected volumes. Inset highlights mismatch across volumes, such as difference in thickness (white arrow heads) and location of structures. D) Result of registration with refraction-corrected volumes.

4.3. Summary

In this section, we described our processing pipeline to convert the volumes acquired from multiple perspectives into a single volume of the whole heart. This pipeline involved segmenting the outer surface of the heart, correcting for refractive distortions, and then automatically registering and stitching the volumes together. We also demonstrated the impact of refraction correction on the match between registered volumes. The impact of refraction correction on improving the accuracy of quantitative data in OCT has been previously validated and published by other groups [53], [54], [56].

Using this volume of the whole heart, various morphological parameters can be quantified, such as the dimensions of the ventricular volume, ventricular wall thickness. The next chapter discusses the use of computational anatomy methods to quantify the morphology of the heart.

Chapter 5.   Quantitative Analysis of Cardiac Morphology

In the previous chapters, we described our method of using optical coherence tomography (OCT) for imaging adult mouse hearts. We first built an OCT system to acquire volumes of the heart from multiple perspectives. We then corrected for refractive distortion in the volumes, and registered and stitched the corrected volumes together to form a single volume of the whole heart. From these volumes of the whole hearts, techniques from computational anatomy can be applied to quantify and compare the morphology of different mouse models. To study the pathological changes in cardiac structure, we are interested in the following morphological parameters:

- Ventricular wall thickness
- Ventricular wall mass and luminal volume
- Myofibril orientation

Prior to determining these parameters, the various chambers and walls must first be segmented within the volumes. To perform the segmentation, we used a semi-automatic method using a commercial 3D image analysis and processing software called Amira (FEI, France). In this section, we first describe our segmentation process, and then describe our method of quantifying the various morphological parameters listed above.

5.1. Semi-Automatic Segmentation

After stitching the sub-volumes into a single volume of a whole heart, the data set can then be analyzed. Prior to quantifying the morphology of the heart, the ventricular surfaces and cavities were first semi-automatically segmented using Amira. Figure 5-1 shows the steps of the segmentation process on three representative slices. Using Amira, the volume was first automatically thresholded using hysteresis. Hysteresis is based on a region-growing algorithm which uses two thresholds. All voxels with intensities greater than the threshold are set as tissue

automatically. For voxels whose intensities are between the low and high threshold, only those voxels that are connected to the high threshold are labeled as tissue. Figure 5-1C shows the result from automatic thresholding using Amira. Although most of the cardiac tissue was segmented automatically, deeper regions that had greater signal attenuation were not always detected. Moreover, the automatic thresholding process could not distinguish tissue from other back-reflected noises, such as the bright back-reflections from the heart surface, or back-reflections from the lens surface. The automatically thresholded results were manually refined (Figure 5-1D). After manual refinement, the atrioventricular valves, ventricular walls, and ventricular lumens were manually labeled in Amira (Figure 5-1E).
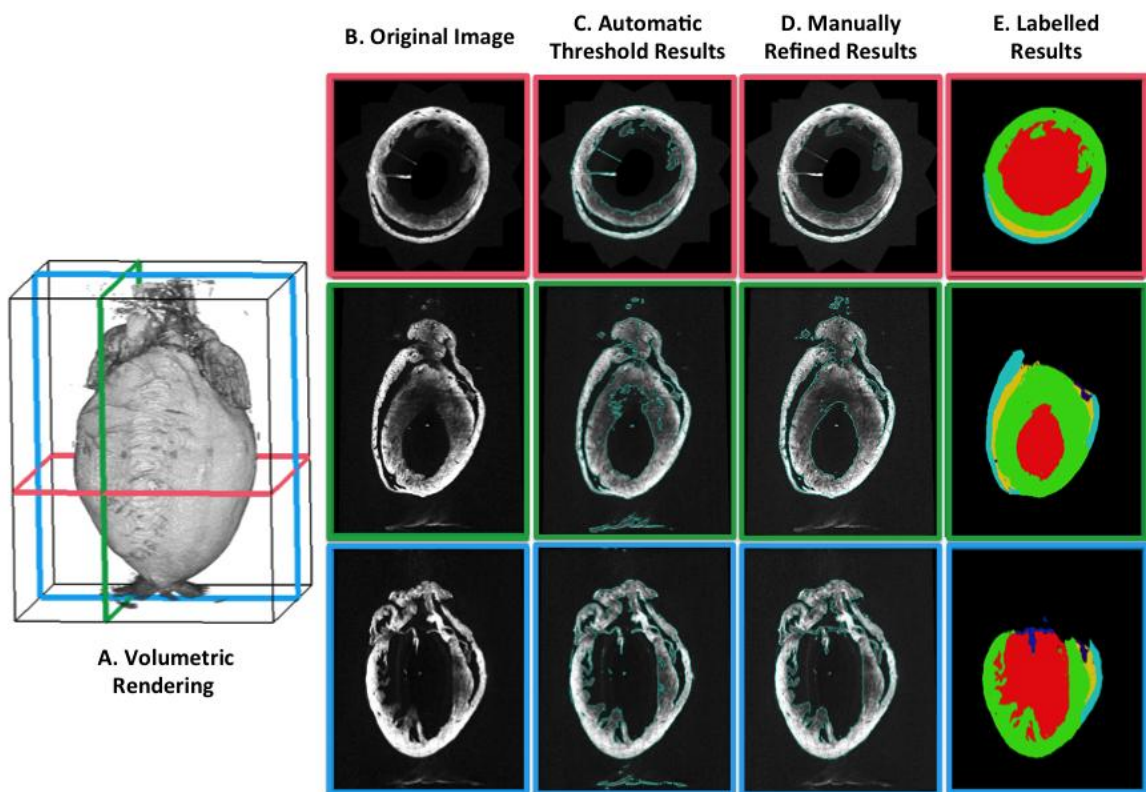
Figure 5-1: Steps involved in segmentation process, shown on 3 orthogonal slices. A) Volumetric rendering of data set showing location of orthogonal slices. B) Original Image. C) Results after automatic thresholding using Amira. D) Manual refinement of automatic threshold to remove noise and include low-intensity tissue regions. E) Slices with manually labeled structures. Green, left ventricular wall; red, left ventricular lumen; light blue, right ventricular wall; yellow, right ventricular lumen; dark blue, left atrioventricular valve.

5.2. Determination of Wall Mass and Luminal Volume

After segmentation, the wall mass and luminal volume can be extracted from the segmented volumes directly. Letting $n_{V,Lumen}$ be the number of voxels assigned to the left/right ventricle volume, and $n_{V,Wall}$ be the number of voxels assigned to the left/right ventricular wall, the wall masses and luminal volumes can be calculated using:

5-1

$$V\ (mL) = n_{V,Lumen}d,$$

5-2

$$m(mg) = n_{V,Wall}dg,$$

Where *V* is the luminal volume, *m* is the wall mass, $g = 1.055\ mg/\mu L$ is the specific gravity of myocardium, and *d* is the size of a voxel, in mm^3.

5.3. Realignment

In order to compare similar regions across multiple hearts, the hearts need to be aligned to a standard orientation. We chose to align the vertical axis to the long axis of the left ventricle, as per standard conventions in the field of cardiac imaging. Since the left ventricle is ellipsoidal in nature, its long axis can be estimated by using Principal Component Analysis (PCA) [59]–[61]. The principal component analysis fits a set of data points to a set of linearly uncorrelated, but orthogonal, variables called principal components. The first component from the PCA transform accounts for most of the variability of the data, and will thus be oriented in the direction of the long axis. Since only the left ventricle coordinates were used to orient the long axis, the PCA transform does not show the direction of the right ventricle relative to the left ventricle. Instead, the circumferential orientation was standardized by finding the mean direction of the right ventricle relative to the left ventricle, and rotating the PCA transform appropriately. Figure 5-2 shows the estimation of the long-axis and circumferential direction on one of the whole volumes, and displays the orientation after realignment.
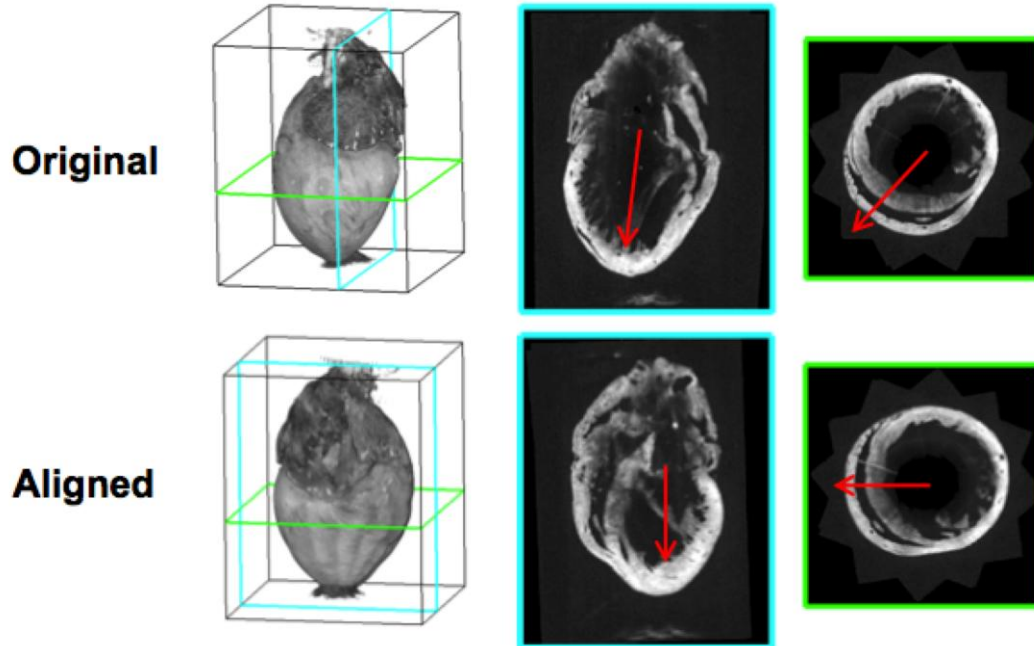
Figure 5-2: Realignment of datasets to standard orientation. Top row: Orientation of acquired data set. Red arrows show the detected long axis and circumferential direction. Bottom row: Orientation of data set after realignment

5.4. Determination of Ventricular Wall Thickness

The myocardial wall consists of two regions: a compact region, and a trabeculated region. Trabeculae carnae are muscular protusions on the inner surface of the ventricles that increase pump efficiency. Following published protocols, we calculated the thickness of the compact regions [62], [63]. Prior to computing the wall thickness, the inner and outer surfaces of the wall have to be segmented. Figure 5-3 shows the various steps in segmenting the inner and outer walls of the right and left ventricles. First, the trabeculae on the endocardial surface of the heart were removed using morphological closing in order to compute the thickness of the compact myocardium. After removal of the trabeculae from the segmented regions, the center of the LV was estimated using a center of mass algorithm (Figure 5-3B), and the image was unwrapped from that point (Figure 5-3C). The boundaries of the right and left-ventricles were then detected in the unwrapped image, and converted back to Cartesian coordinates (Figure 5-3D).
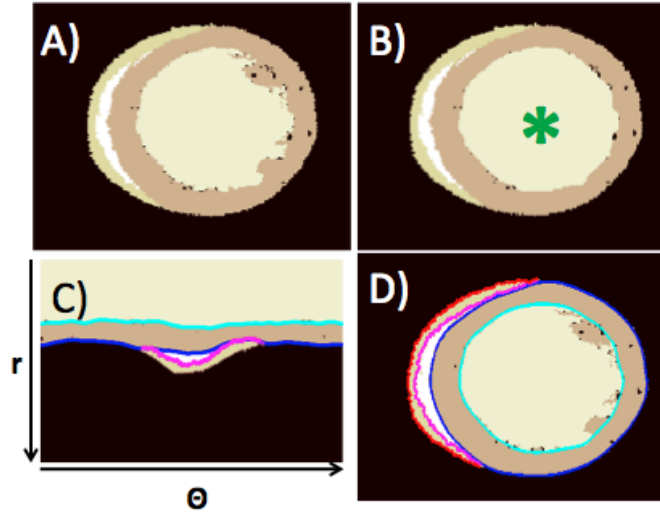
Figure 5-3: Algorithm for segmenting inner and outer walls. A) Labeled short-axis slice B) Short-Axis slice with trabeculae removed, to measure the compact myocardium. Green star shows the detected center from which the image is unwrapped. C) Surfaces were segmented in the polar domain. D) Segmented surface transformed to original coordinates.

The detected surfaces were then spline-fitted to smoothen the surface and resample it evenly. A spline function was fitted to the arc length of the curve, which was computed using:

<div align="right">**5-3**</div>

$$s_2(\theta) = \int \sqrt{1 + \left(\frac{ds_1}{d\theta}\right)^2} \; d\theta$$

We calculated the arc length for θ = [0, 370] to ensure that the calculated arc length would be a closed surface for θ = [0, 360], since no boundary conditions were enforced in the spline-fitting. Figure 5-4 shows the segmented surface before and after spline fitting. The spline-fitted curve is smoother than the original curve. Another benefit of spline-fitting to the arc length is that the boundary is now resampled evenly according to the length of the curve.
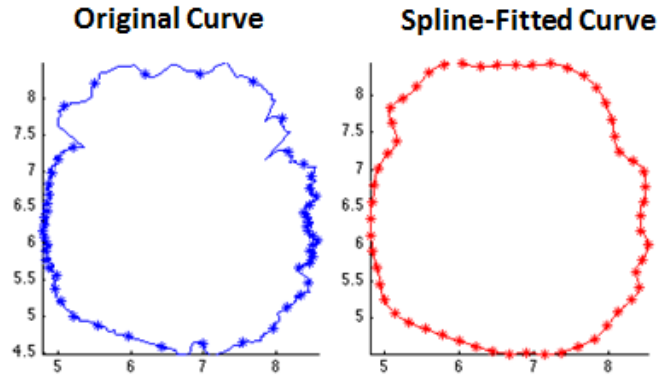
Figure 5-4: Segmented Boundary before and after spline fitting. Spline-fitting was used to smoothen the curve and resample it evenly.

After determining the inner and outer boundaries of the ventricular wall, the wall thickness can then be calculated. Wall thickness can be described as the one-to-one mapping of a point on the outer surface to a point on an inner surface. Letting $P_1(x_1,y_1,z_1)$ and $P_2(x_2,y_2,z_2)$ be points on the outer and inner surface respectively, the thickness is the distance between these two points; that is,

5-4

$$Thickness = D(P_1, P_2) = \sqrt{(x_1 - x_2)^2 + (y_1 - y_2)^2 + (z_1 - z_2)^2}.$$

There are multiple methods of finding the point-to-point correspondence between the inner and outer surface. Figure 5-5 presents two intuitive methods of determining wall thickness: the minimum thickness method, and the perpendicular thickness method. The minimum thickness method finds the point P_2 that is the closest to a given point P_1. In contrast, the perpendicular thickness method finds the surface normal at a given point P_1 and then finds the point on the inner surface that intersects the surface normal.

55
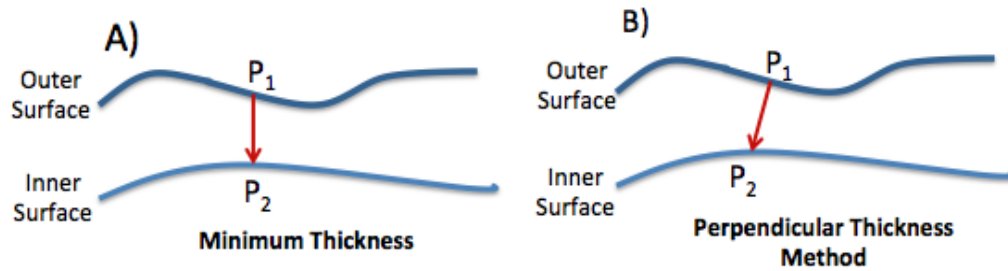
Figure 5-5: Different methods of determining thickness. A) Minimum thickness method. B) Perpendicular thickness method

To compute the minimum thickness, for each point P_{1i} on the outer surface, the distance between P_{1i} and the points within the inner surface around the surrounding region was calculated. The point on the inner surface P_{2i} that had the smallest distance was set to be the corresponding point.

To compute the perpendicular thickness, we utilized properties of cross products and dot products. Figure 5-6 depicts the method by which the point-to-point correspondence for the perpendicular thickness method was determined. The vector normal at each point on the outer wall was computed in 3D using the cross product of the vertical and horizontal gradients (Figure 5-6A). For each point in the outer wall, the difference vector from the inner to outer wall was computed (Figure 5-6B). The intersection point between the surface normal and inner surface was then determined by calculating the dot product to find the difference vector that was parallel to the surface normal (Figure 5-6C).
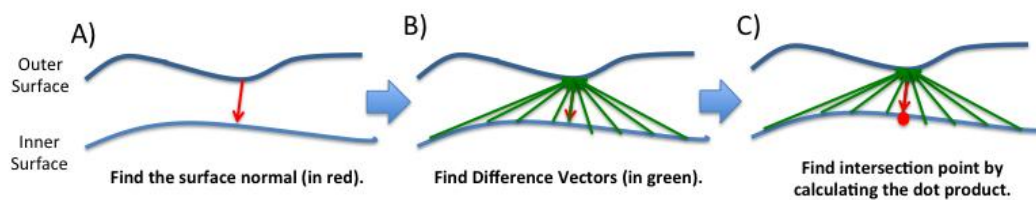
Figure 5-6: Method for calculating thickness perpendicular to the outer surface. A) Surface normal is calculated using cross-product of the gradients. B) Difference vectors from the inner surface points to the outer surface point are calculated. C) Point at which the surface normal intersects the inner surface is found by calculating the dot product of the difference vector and surface normal.

The wall thickness of the left ventricular wall was calculated using both the minimum and perpendicular thickness methods. The LV wall was then divided into 4 myocardial segments – anterior, lateral, septal, and inferior. The relative locations of these 4 segments are shown in Figure 5-7. A comparison of the thickness results calculated using the minimum thickness method and the perpendicular thickness method is shown in Figure 5-8. The thickness at a particular point has been displayed as a heat map, where blue represents the thinnest portions and red the thickest portions.
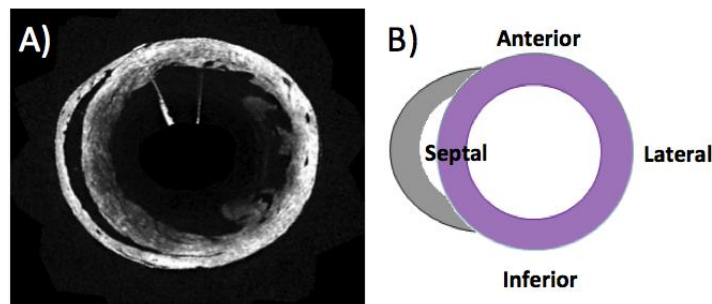
Figure 5-7: A) Representative short-axis slice. B) Diagram of short axis slice, showing the relative locations of the anterior, septal, inferior, and lateral segments.
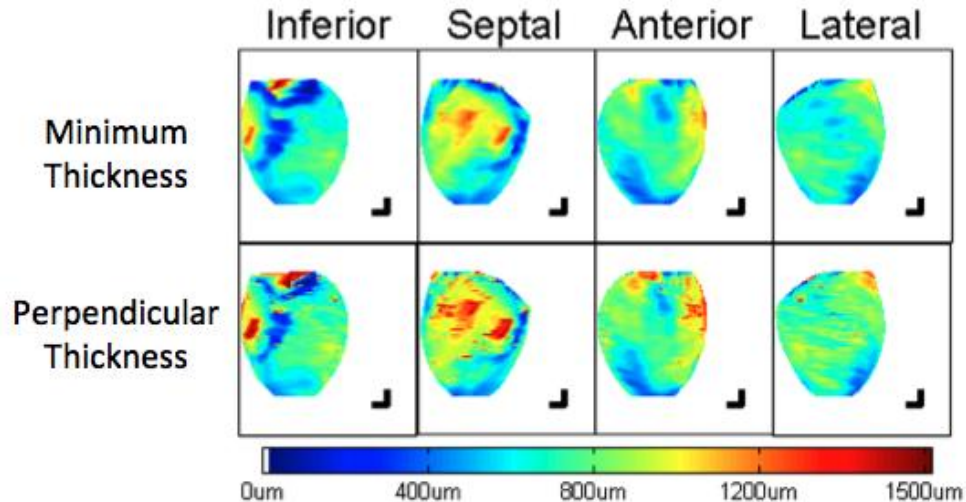
Figure 5-8: Result of calculating LV wall thickness using minimum and perpendicular thickness methods. The measurements from the minimum thickness method are thinner and have lower spatial frequency than the perpendicular thickness method.

Comparing the perpendicular thickness and minimum thickness methods, the thickness maps from the minimum thickness method have a lower spatial frequency. Moreover, the

thickness values calculated using the minimum thickness method is smaller than the perpendicular thickness method. Intuitively, this makes sense: compared to the actual thickness, the minimum thickness method should yield measurements that are equal or smaller than the actual thickness. Despite these differences, the results from both methods show similar trends: in both cases, the thickness in the septal wall seems to be larger than the other three segments.

Although these two methods are intuitive, each has its own weakness. The perpendicular method does not ensure a one-to-one mapping and is not symmetrical. Since the thickness measurement is performed orthogonal to the outer surface, but not the inner, there is no guarantee that the thickness measurement will be the same if the surfaces are interchanged. That is, the thickness measurement might differ if the thickness is calculated from the inner to outer surface instead. While the minimum thickness might be more symmetric, it still does not provide a unique mapping between the surfaces. Moreover, it has the tendency of underestimating the true thickness. In our case, however, both the inner and outer boundaries of both the right and left ventricle contain few curves and can be modeled as two ellipses, or two elliptical arcs. Thus, the above issues with both methods should be minimal, and universal across all the hearts. From Figure 5-8, the trends in LV thickness are not changed despite the inherent flaws of these methods. Thus, both of these methods of determining thickness should be sufficient to determine whether a significant regional difference in thickness exists between mouse types.

5.5. Quantification of Fiber Orientation

The final parameter that will be quantified is fiber orientation. While this parameter does not strictly require the stitched result, applying the algorithm on the stitched result could result in the quantification of the global fiber orientation. Prior to quantifying fiber orientation, the free wall was first virtually sliced parallel to the epicardial surface. Figure 5-9 depicts the slicing procedure. The surface normals (yellow arrows) were first calculated from the segmented surface coordinates by taking the cross product of the horizontal and vertical surface gradients. Slices were then extracted by finding the spatial coordinates that are equidistant from the epicardial surface. The green line shows the segmented epicardial surface, whereas the red line shows the location of one of the interior slices through the myocardium. These slices were then projected to a 2D image.
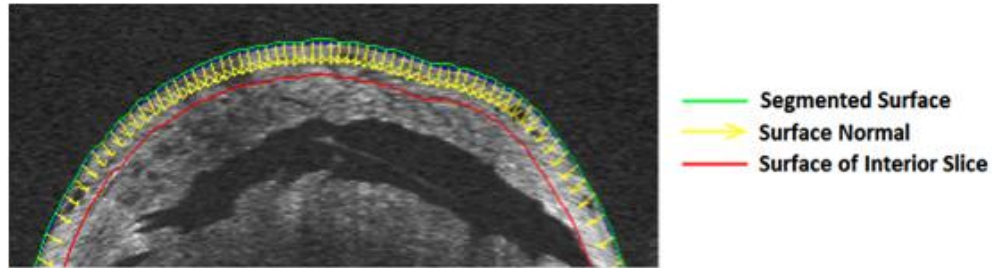
Figure 5-9: Diagram showing process of parallel en-face slicing on the right ventricular free wall. Yellow arrows show the surface normal, while the green and red lines show the top surface and surface of an interior slice respectively.

Figure 5-10 displays a few of the slices taken from the epicardial to endocardial surface of the right ventricle of a wild-type heart, where we can see the gradual counter-clockwise rotation in fiber orientation. Each slice had a thickness of 15μm.
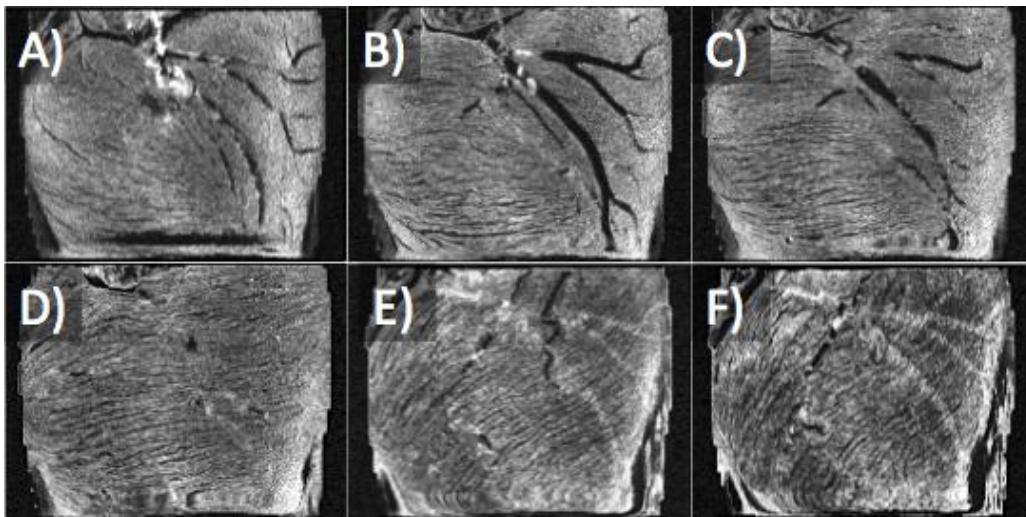
Figure 5-10: En-face slice from the right ventricle free wall of a mouse heart, going from epicardial (A) to endocardial (F) surface. Slices show transmural rotation in fiber angle with depth.

To automatically quantify the fiber orientation in the en-face slices, we adapted a previously-published method [64], [65]. The images were pre-processed using a Gaussian high-pass filter to remove shadows from the blood vessels, and a Wiener filter for speckle reduction. The gradients of the images were then calculated by convolving the images with two 3x3 Sobel filters, G_X and G_Y. For each pixel in the en-face image, the gradient magnitude G and direction θ were calculated using

$$G(i,j) = \sqrt{G_x^2(i,j) + G_y^2(i,j)} \text{ and}$$

5-6

$$\phi(i,j) = \phi_{ij} = \tan^{-1}(\frac{G_y(i,j)}{G_x(i,j)}).$$

The dominant fiber orientation within a window W was then calculated by first finding the dominant gradient orientation using an accumulator scheme. An accumulator array A_θ^W was calculated using

5-7

$$A_\theta^W = \sum_{(i,j)\in W} G(i,j) \frac{e^{2\cos[2\theta-\phi_{ij}]}}{e^2}$$

where $\theta \in [0°, 180°)$[64]. The equation for A_θ^W was set by assuming that the pixel orientations follow a circular probability distribution with a von Mises distribution, $e^{2\cos[2\theta-\phi]}$, that has a mean value of ϕ_{ij} [64].The dominant gradient orientation was then determined by finding the angle at which A_θ^W is maximum. The dominant fiber orientation is perpendicular to the dominant gradient orientation. We eliminated measurements that corresponded to regions that did not contain tissue as determined using global thresholding on the intensity images.

Fiber disarray is an important parameter for studying pathological changes in cardiac morphology. Karlon et al found that myofiber disarray corresponded to a local angular dispersion of greater than 20° for a ~0.01mm^2 region [64], [66]. For a set of fiber orientation measurements θ_i, the mean and standard deviation of the fiber orientation was calculated using:

5-8

$$cos2(\theta_{mean}) = \frac{C}{R} \text{ and}$$

5-9

$$\sigma = \frac{1}{2}(-2\log(R_{mean}))^{\frac{1}{2}}, \text{where}$$

θ_{mean} is the mean orientation, and σ is the standard deviation [64]. C, R, and R_{mean} is determined from the fiber orientation measurements using

$$C = \sum_{i} cos2\theta_i,$$

$$S = \sum_{i} \sin 2\theta_i,$$

$$R = \sqrt{C^2 + S^2}, \text{ and}$$

$$R_{mean} = \frac{R}{n}$$

where θ_i is the fiber orientation measurements, and n is the number of measurements [64]. Using Equation 5-8, we calculated the mean orientation within the center region of each slice. The change in mean orientation with depth is presented in Figure 5-11, with the error bars scaled to the standard error of the mean $SE = \frac{\sigma}{\sqrt{N}}$, where N is the number of measurements. From the plot, the fiber orientation rotates counter-clockwise from epi- to endo- cardial surface, which is consistent with previously published results [39], [65], [67].

61
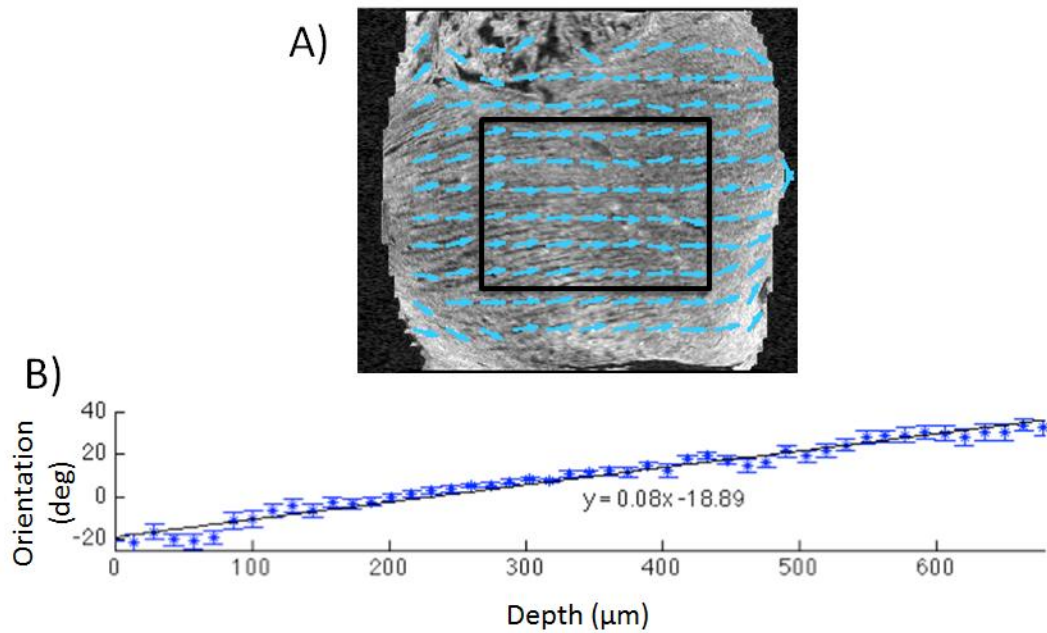
Figure 5-11: A) Fiber slice showing automated fiber orientation (blue arrows), and region that was included for the mean orientation calculation (black box). B) Mean fiber orientation vs depth for right ventricular free wall, showing transmural rotation.

5.6. Summary

In this section, we presented various computational tools for quantifying the cardiac morphology from the OCT volume of the whole heart. After semi-automatic segmentation and labeling, the hearts were re-aligned by estimating the long axis of the left ventricle using ellipsoid-fitting methods. We then presented methods for computing the following morphological parameters: luminal volumes, wall masses, local wall thickness, and fiber orientation. In the next section, we present results of a study that compares the cardiac morphology of wild-type and a transgenic mouse model of Marfan syndrome.

Chapter 6.   Effect of Marfan Syndrome on Cardiac Morphology

A background on Marfan syndrome (MFS) and our motivation for studying its effect on cardiac morphology was presented in Chapter 2. In MFS, cardiovascular complications such as aortic dilation, mitral valve prolapse, and pulmonary artery dilation are well documented. However, cardiac dysfunction in MFS is not as well understood. Transgenic mouse models can be used to study the etiology behind MFS. However, the cardiovascular phenotypes of transgenic mouse models of MFS are not well characterized.

Ultrasound is commonly used to study the structure and function of the mouse heart. While 3D ultrasound machines do exist, most labs still routinely use 2D high-frequency ultrasound, and estimate 3D parameters from 2D measurements. The estimation of 3D volume, for example, is routinely performed using the diameter of the left ventricular (LV) lumen. 2D to 3D conversion methods make assumptions on the geometry of the lumen which may not necessarily be conserved in diseased hearts. Since OCT provides 3D information, it can also be used to study whether or not these 2D estimation methods are valid in MFS.

In this chapter, we investigated the change in cardiac morphology with MFS in mice, focusing on measurements of the ventricular thickness, mass, and wall thickness. We also compare the 2D estimation method of ultrasound to 3D measurement of volume.

6.1. Methods

6.1.1.   Animal Preparation

All experimental protocols were approved by the Animal Ethics Board of the University of British Columbia and are in accordance with the Canadian Council on Animal Care (CCAC) Regulations. Three wild-type (Fbn1 +/+) and five Marfan (Fbn1 C1039G/+) mice were used in

this study. All mice were twelve months of age. The Marfan mouse models were provided by John Hopkins University.

The mouse heart preparation was performed by Ms. Lillian Lee, a graduate student in a collaborating lab in the School of Biomedical Physiology and Kinesiology. In preparation for extracting the heart, the mice were first heparizined (100 μL, at 1000 U/mL and 5000 U/kg) and then anesthetized via an intra-peritoneal injection of 40 μL somnotol (32.5 mg/ml at 65 mg/kg). After the disappearance of the toe pinch response, the hearts were exposed via a midsternal thoracotomy and excised 2mm distal to the coronary sinus. The hearts were then cannulated at the aorta on a Langendorff apparatus and retrogradely perfused with Tyrode's solution (4 min at 2 mL/min) and 4% paraformaldehyde (30 min at 2 mL/min) to remove the blood and fix the tissue. The fixed heart was stored at 4°C in PBS. At this point, the mice were provided to our imaging laboratory. Prior to imaging, the hearts were cleared via immersion in glycerol under a graded protocol (50% and 70% for 1 day each).

6.1.2.   Data Acquisition

A custom-built 1060 nm swept-source optical coherence tomography (SS-OCT) system was used to image the hearts. The details of the acquisition system, along with a schematic, have been provided in Chapter 3. For each heart, volumes were acquired at 30-degree increments, across the entire 360-degree span. At each rotation, 10 volumes were acquired and averaged to offset the loss in signal-to-noise from the telecentric scan lens and glycerol clearing. Each volume consisted of 1408x400x800 voxels, with each voxel having a physical dimension of 2.63x21.1x17.98 um^3.

6.1.3.   Image Processing

After acquiring the volumes for different perspectives, these volumes were then corrected for refractive distortions, rigidly registered, and stitched together to form a single volume of the whole heart, as per the methods described in Chapter 4. Each stitched volume had an isotropic voxel size of 20x20x20 μm^3. From the volume of the whole heart, the left ventricular (LV) and right ventricular (RV) volumes and masses were computed, along with the LV wall thickness, as per Chapter 5.

6.1.4. Comparison with Ultrasound

2D ultrasound is commonly used to study the cardiac structure and function of the mouse. A common method to estimate the 3D volume is to measure the diameter of the left ventricular lumen, D, at the mid-papillary level, and then apply the equation

6-1

$$Volume\ (\mu L) = \frac{7}{2.4 + D} * D^3$$

to convert the diameter measurement to volume [68]. To compare the 2D estimation to the 3D volume measurement, we manually selected slices, which corresponded to the mid-papillary level in each volume and automatically computed the diameter. Figure 6-1 shows the relative location of the short-axis slice at the mid-papillary level, which intersects the papillary muscles within the left ventricle.
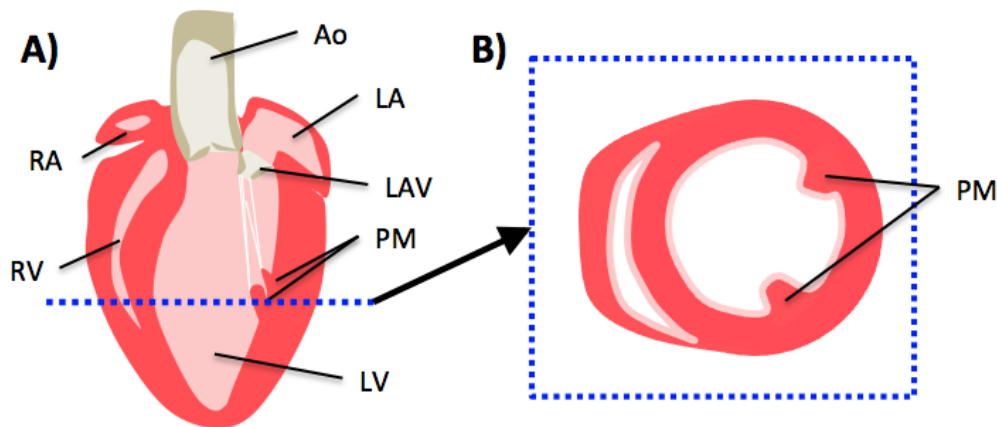
Figure 6-1: Location of short axis slice at mid-papillary level (MPL) for 3D volume estimation. A) Diagram of mouse heart showing location of MPL slice. B) Diagram of MPL short-axis slice, showing 2 papillary muscles within left ventricle. Ao, aorta; LA, left atrium; LAV, left atrioventricular valve; LV, left ventricle; RA, right atrium; RV, right ventricle; PM, papillary muscle.

Since the mid-papillary level is not only visible from a single slice, but a range within the heart, we chose a range of slices from each heart that we thought corresponded to the mid-papillary level. For the diameter calculation, the maximum distance between two points at a given angle was determined. Figure 6-2 displays a short-axis slice at the mid-papillary level taken from one of the hearts, along with the computed diameter (red line). The angle was set to be similar to ultrasound imaging protocols.
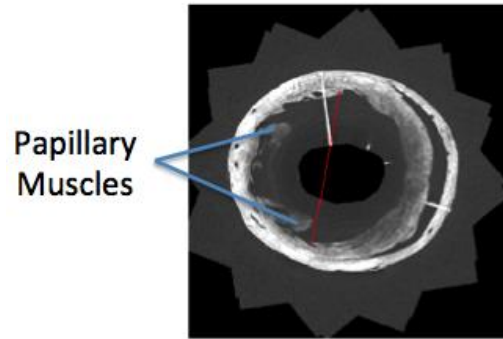
Figure 6-2: Determination of mid-papillary slice diameter, with the length of red line corresponding to the diameter.

6.2. Results and Discussion

The body weights, ventricular volumes, masses, and ventricular mass-to-volume ratio were compared using a paired t-test, with significance set at $p<0.05$. The luminal volumes and masses were normalized by body weight. Table 1 presents all the values, reported as mean ± SEM. Only the normalized LV volume, and LV volume to mass ratio had significant differences, as presented in Figure 6-6.

Table 1: Comparison of body weight, and ventricular mass and volumes between the Marfan and wild-type mice.

	Marfan	Wild-Type	p
BW(g)	36.78 ± 1.79	43.63 ± 2.17	0.054
RV Volume (µL)	14.97 ± 2.53	10.27 ± 2.45	0.264
RV Volume/ BW (µL/g)	0.42 ± 0.09	0.24 ± 0.05	0.195
RV Mass (mg)	33.93 ± 2.53	34.68 ± 2.42	0.85
RV Mass/BW(mg/g)	0.92 ± 0.05	0.80 ± 0.06	0.173
RV Mass/Volume (mg/uL)	2.51 ± 0.40	3.68 ± 0.67	0.156
LV Volume (µL)	110.56 ± 8.92	97.29 ± 7.47	0.35
LV Volume / BW(µL/g)	3.01 ± 0.21	2.24 ± 0.18	0.047
LV Mass (mg)	110.69 ± 9.17	120.59 ± 11.45	0.529
LV Mass/ BW (mg/g)	3.01 ± 0.21	2.76 ± 0.19	0.451
LV Mass/Volume (mg/µL)	1.00 ± 0.01	1.24 ± 0.06	0.002
RV/LV Volume	0.14 ± 0.03	0.10 ± 0.02	0.387
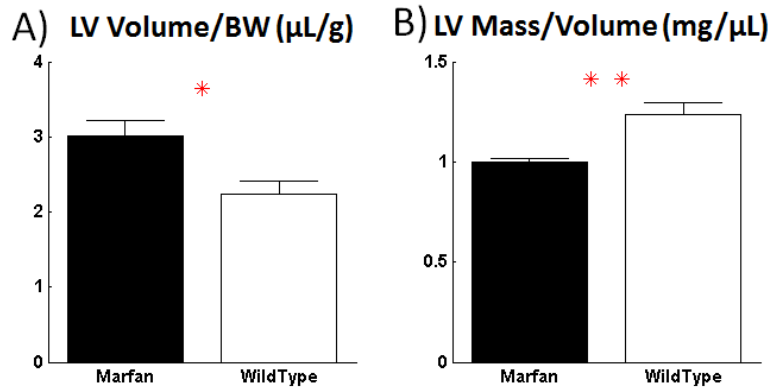
Figure 6-3: Comparison of LV Wall Masses and Volumes between wild-type and Marfan mice. A) Comparison of normalized LV volume. B) Comparison of LV mass-to-volume ratio. * p<0.05, ** p < 0.01.

Comparing the wild-type and Marfan mouse model, the MFS mice exhibit significantly smaller mass-to-volume ratios (1.00±0.01 vs 1.24±0.06 mg/µL) and larger normalized LV volumes (3.01±0.21 µL/g vs 2.24±0.18 µL/g).

6.2.1. 2D to 3D comparison

Figure 6-4 provides a comparison of the volume estimated from 2D parameters to the actual volume, as computed from the labeled volume. Using a paired t-test, a significant difference existed on the estimated to actual volume ratio for wild-type and Marfan mice. Linear regression was applied to determine the relation between the estimated and actual volumes. From the regression results, while the slopes of the fit are quite similar, there is an offset difference. The 2D method underestimates the actual LV luminal volume in the MFS mice, compared to the wild-type mice.
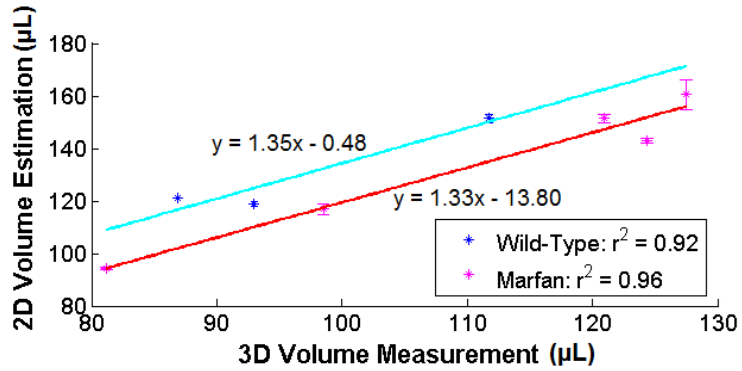
Figure 6-4: Comparison of estimated to actual volume in Marfan and wild-type mice. The 2D method underestimates the actual volume in the Marfan with respect to the wild-type mice.

In MFS, it is possible that the dilation changed the underlying geometry, thus invalidating the geometrical assumptions underlying the 2D to 3D conversion equations. Figure 6-5 compares the difference in the actual and estimated LV volumes between the Marfan and wild-type mice. From the 3D volume calculations, the LV volume in the Marfan mice is significantly larger than the wild-type mice after normalizing for body weight. The estimated volume did not show a significant difference either before or after normalization.
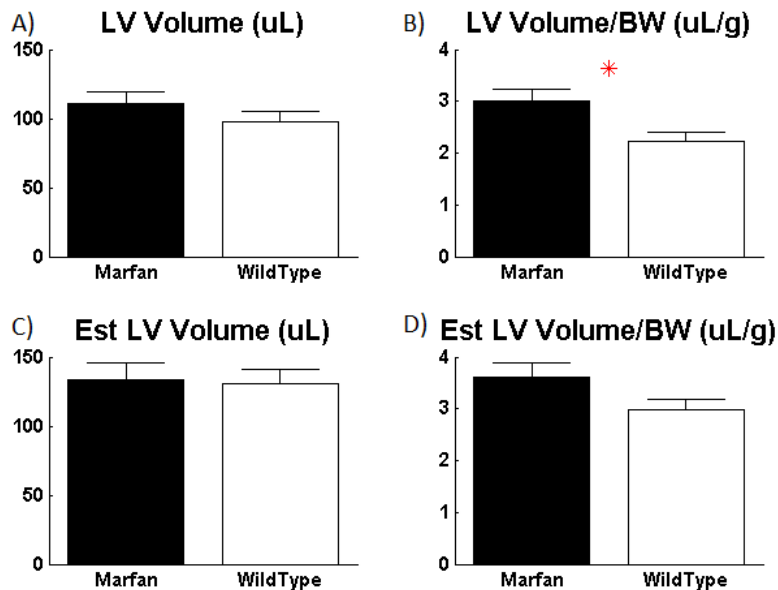
Figure 6-5: Comparison of estimated and actual LV volume between Marfan and wild-type mice. A) Actual LV volume. B) Normalized actual LV volume. C) Estimated LV Volume. D). Normalized estimated LV volume. * $p < 0.05$.

68

6.2.2.   Wall Thickness

The thickness of the LV was computed across the entire wall in 3D, and displayed by dividing the LV wall into 4 myocardial segments: anterior, lateral, septal, and inferior, as described in Chapter 5. Figure 6-6 and Figure 6-7 provide a comparison of the thickness of the left ventricle across the 8 hearts using the minimum and perpendicular thicknesses, respectively. The thickness at a particular point has been displayed as a heat map, where blue represents the thinnest portions and red the thickest portions. The right ventricle has been show in gray for the inferior and anterior views for orientation purposes.
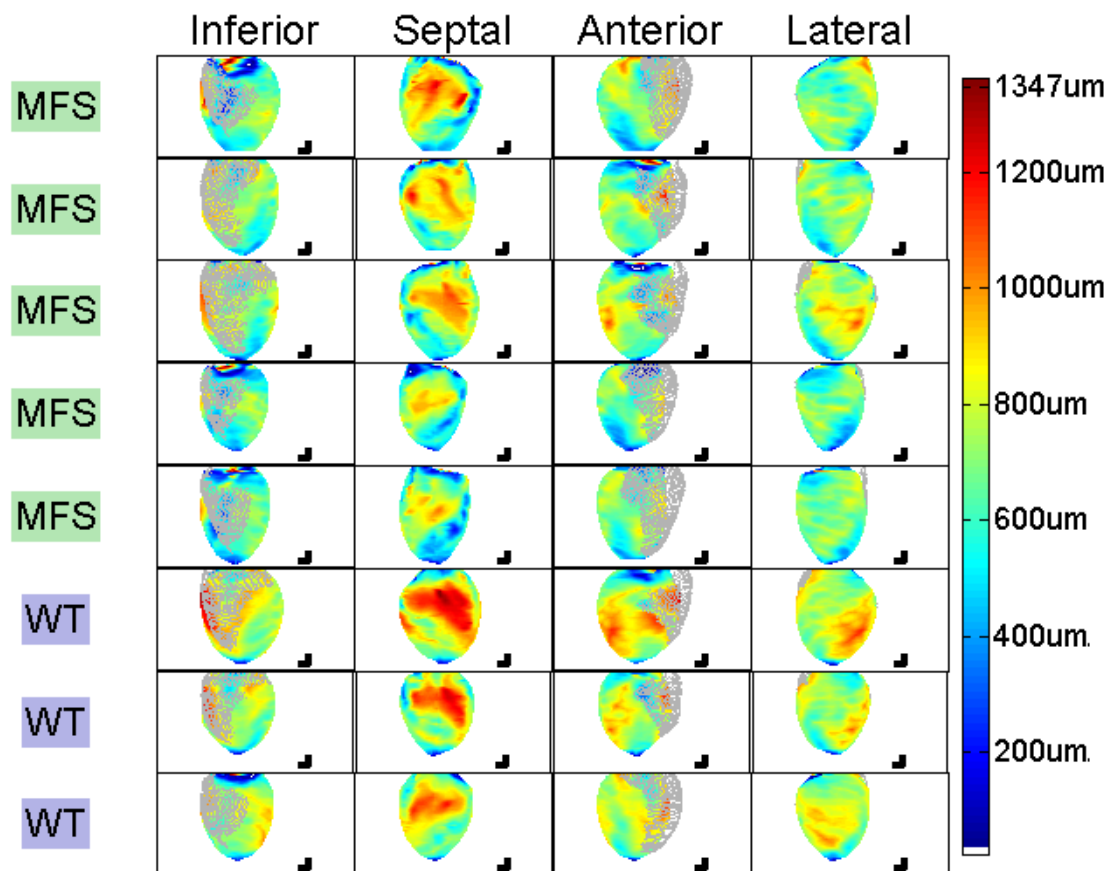
Figure 6-6: Comparison of ventricular wall thickness between Marfan and wild-type mice, where thickness was computed using the minimum thickness method. Gray points in the inferior and anterior views show location of right ventricle. MFS, Marfan syndrome; WT, wild-type.
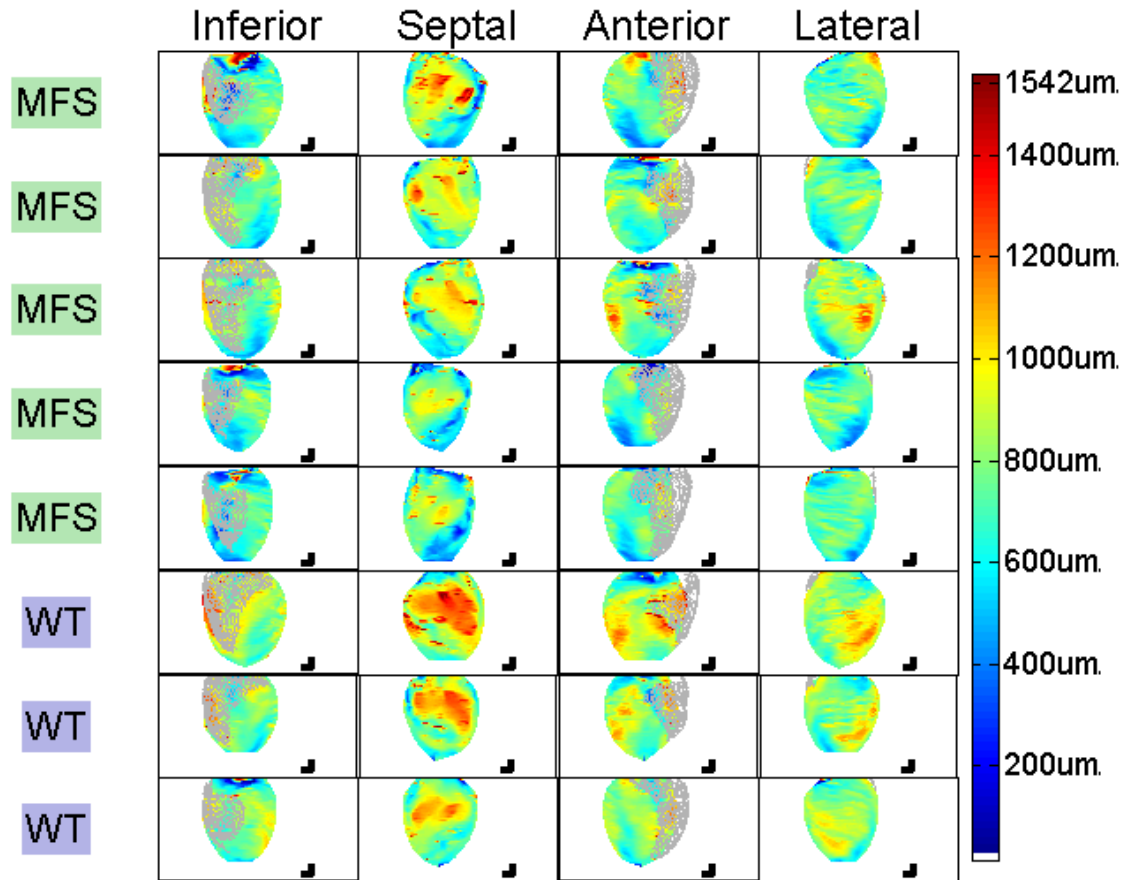
Figure 6-7: Comparison of left ventricular wall thickness between Marfan and wild-type mice, where thickness was computed using the perpendicular thickness method. Gray points in the inferior and anterior views show location of right ventricle. MFS, Marfan syndrome; WT, wild-type.

By observation of the data in Figs 6-4 and 6-5, the Marfan mice qualitatively have thinner LV walls than their wild-type counterparts. The difference in thickness is most apparent in the septal region. Comparing the perpendicular thickness method and the minimum thickness method, the thickness map has a lower spatial frequency when using the minimum thickness method. Moreover, as expected, the thickness values calculated using the minimum thickness method are smaller than the perpendicular-thickness method. In both cases, the Marfan mice tend to exhibit thinner walls.

One potential conflicting factor in the wall thickness comparison is the effect of heart size. We normalized the wall thickness measurements by body weight, which is an acceptable measure for age-matched mice [69]. Figure 6-8 presents the perpendicular thickness results after normalizing for body weight. After normalizing for body weight, the difference in wall

thickness was no longer evident qualitatively. Instead, comparing the MFS to wild-type mice, the MFS mice seem to exhibit slightly thicker walls in comparison to their wild-type counterparts. As the mean body weight of the MFS mice in this study was smaller than the wild-type mice, it is possible that the apparent thinness from the previous comparison was due to difference in body weight, and not pathological.
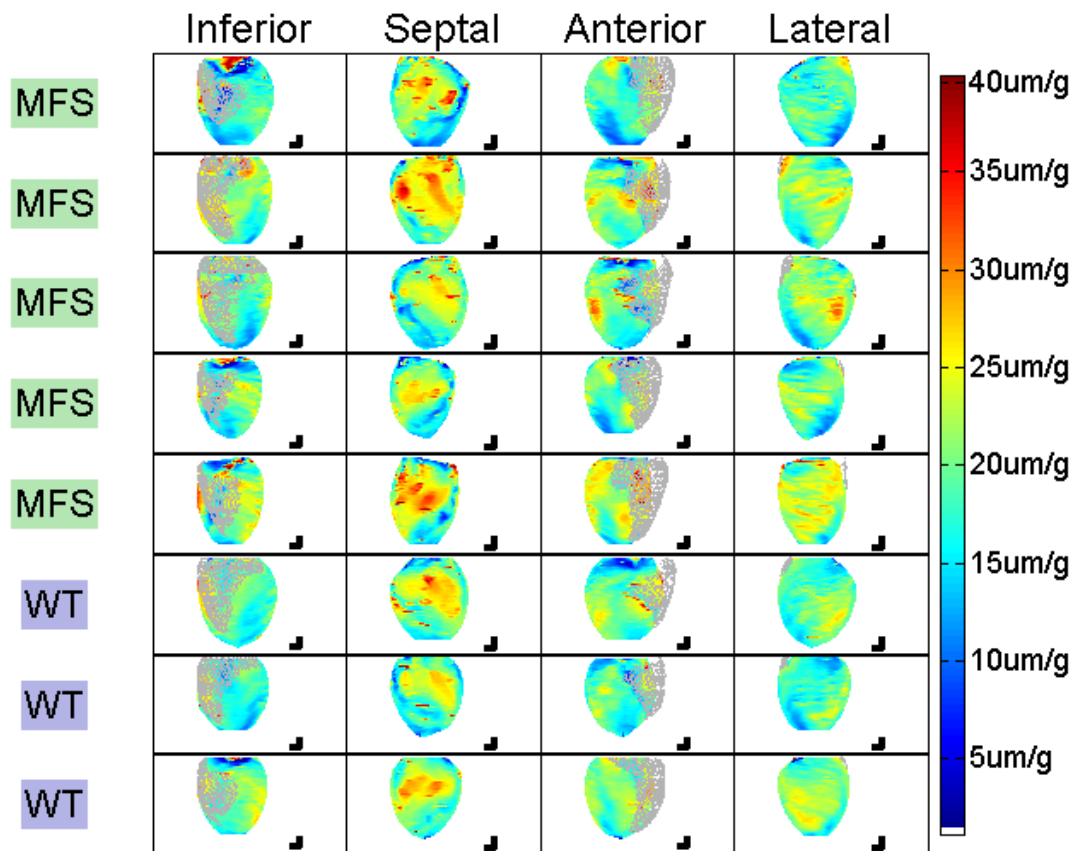
Figure 6-8: Comparison of normalized left ventricular wall thickness between Marfan and wild-type mice, where thickness was computed using the perpendicular thickness method. Gray points in the inferior and anterior views show location of right ventricle. MFS, Marfan syndrome; WT, wild-type.

6.3. Myocardial Fiber Orientation

Figure 6-9 presents a qualitative comparison of the myocardial fiber orientation in the right ventricular free wall of a Marfan and wild-type mouse. The slices are presented from sub-epicardial to sub-endocardial surface. The slices have been shown side-by-side with the automatically determined fiber angle. Qualitatively, the fiber orientation appears to be more

uniform across the right ventricle compared to the Marfan mouse (yellow arrowheads). However, the disarray is not as visible when compared using the automatically determined fiber orientation. Strong features, such as coronary vasculature, cause inaccuracies in the fiber orientation determination (white arrowheads) using the automated algorithm.
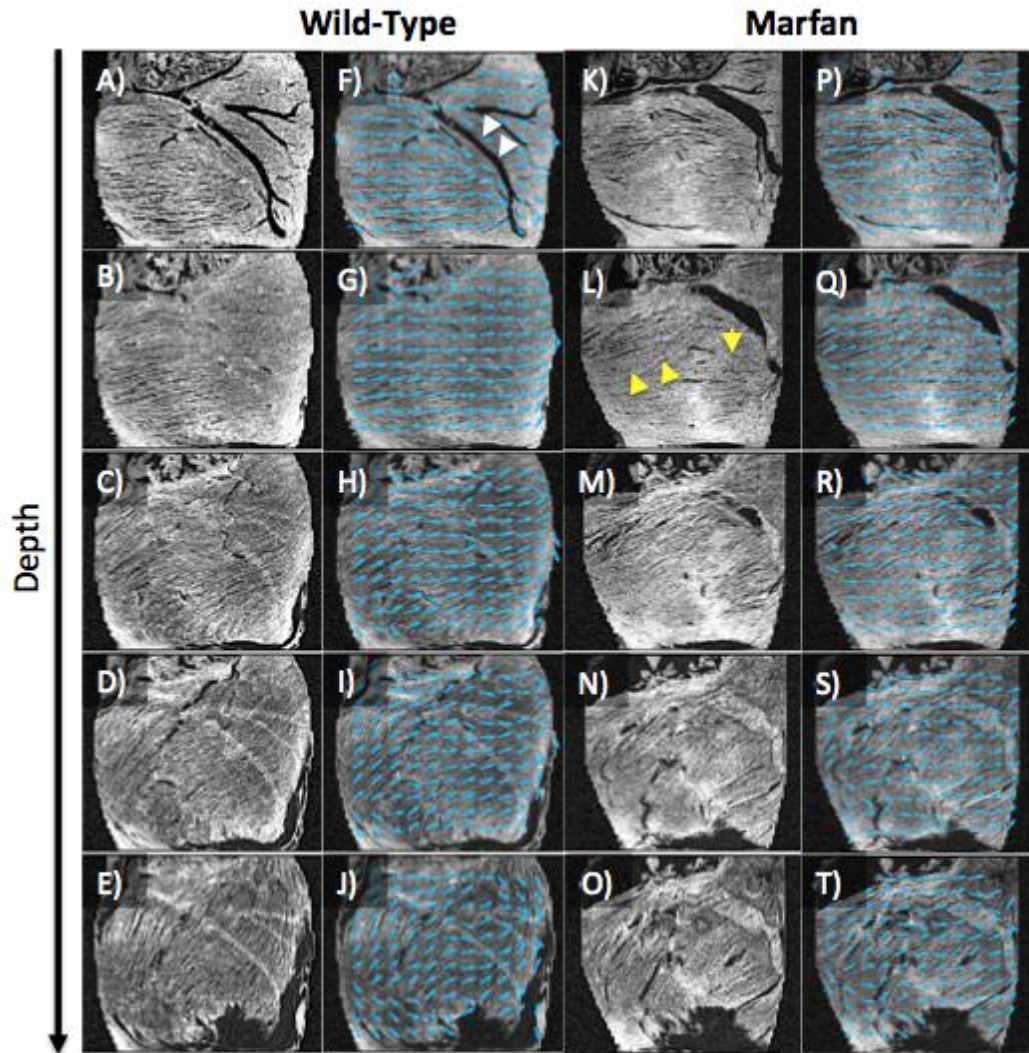
Figure 6-9: Comparison of myofiber orientation in right ventricle of wild-type and Marfan mouse. (A)-(E): Slices from the RV free wall of a wild-type mouse, going from epicardial (A) to endocardial (E) surface, with fiber orientation shown in (F)-(J). (K)-(O): Slices from the RV free wall of a MFS mouse, going from epicardial (K) to endocardial (O) surface, with fiber orientation shown in (P)-(T). Coronary vasculature can confuse the automatic fiber orientation algorithm (white arrowheads). Marfan mice seem to have less-uniform distribution of fiber orientation (yellow arrowheads).

For a quantitative comparison, the mean orientation and dispersion within each slice was computed as described in Chapter 5. Since the slices weren't truly flattened, but sliced parallel to the epicardial surface and project to a 2D image, only fiber measurements within the center region of the image was considered. Figure 6-10 compares the mean fiber orientation vs depth and the angular dispersion in the Marfan and wild-type mice. For the mean orientation, the wild-type mouse has data points at greater depth as it had a larger average right ventricular wall thickness. In both the Marfan and wild-type mice, the right ventricular free wall exhibits a rotation in angle of 0.11 and 0.08 °/μm, respectively. Comparing the angular dispersion, neither of the data sets exhibited dispersion large enough to meet the criterion for fiber disarray as by Karlon et al [64]. We did not quantify the fiber orientation in the right ventricular free wall of the remaining hearts, as they were not visible, for reasons that are discussed in the last chapter.
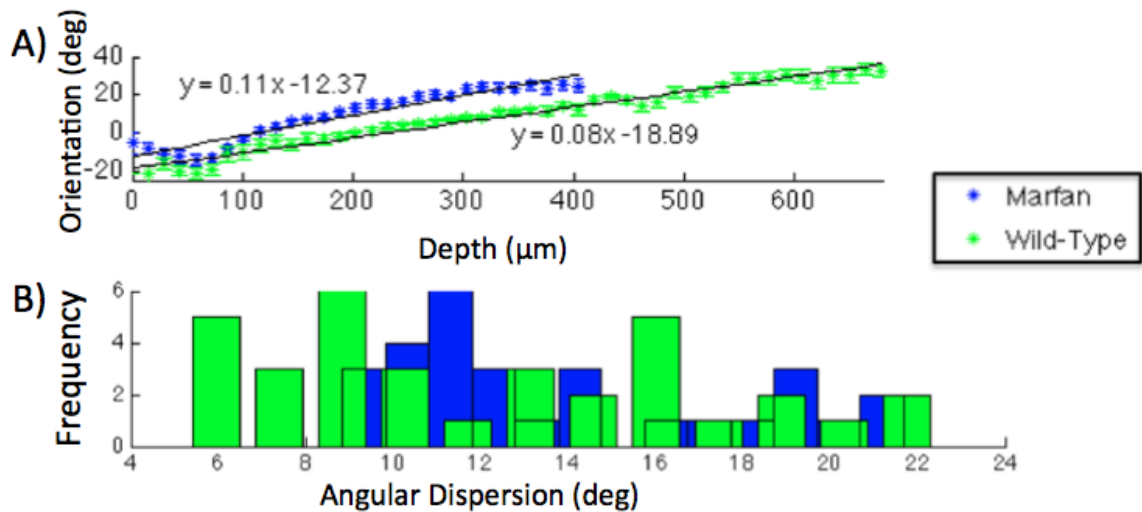
Figure 6-10: Comparison of mean orientation and dispersion of wild-type and Marfan mice. A) Mean fiber orientation per depth in the right ventricular free wall of Marfan (blue) and wild-type (green) mice, showing rotation over depth. B) Frequency of dispersion in Marfan (blue) and wild-type (green) mice.

6.4. Discussion

In this study, we used optical coherence tomography (OCT) to image and compare the cardiac morphology of wild-type and Marfan mice. Our preliminary results indicate that the Marfan mice exhibit significantly decreased left ventricular mass-to-volume ratio than their wild-type counterparts. The smaller mass-to-volume ratio is primarily due to the change in volume: when adjusted for body weight, the Marfan mice had significantly increased left ventricular

volume, with little change in LV mass. Qualitative data on the normalized LV thickness also suggest that the Marfan mice might have slightly thicker walls. The presence of dilated volumes with near-normal wall thickness is suggestive of dilated cardiomyopathy (DCM), which is in agreement with previously reported findings, as discussed in Section 2.4 [14]. However, it is not clear whether DCM is a primary finding, or secondary to abnormal hemodynamic loading conditions from other cardiovascular complications.

We also compared LV volume measurements from OCT with estimated values from ultrasound. While a significant difference between the Marfan and wild-type mouse was found in the normalized LV volumes, the 2D estimated volumes did not yield a significant difference. One possible reason for the loss in significance is that the volumes in the Marfan mice were underestimated in comparison to the wild-type mice. Other researchers have also found that, for comparisons of 3D parameters and gross morphology, ultrasound is not as sensitive as 3D imaging modalities such as MRI [16], [20].

We compared the fiber orientation in two representative hearts, one from each a wild-type and Marfan mouse. The other hearts were not analyzed because the fiber orientation was not visible from the OCT images. In both cases, the fiber orientation rotated counter-clockwise from epicardial to endocardial surface, as has been previously described [39], [67]. Although the fiber orientation within the Marfan mice was qualitatively less uniform, we did not find evidence of myofiber disarray in the Marfan mice. The dispersion from the wild-type mouse was surprisingly high. One possible factor that could skew the dispersion measurements is the noise due to low fiber visibility, and the sensitivity of the algorithm to other structures such as coronary vasculature. Finally, the analysis needs to be extended on more hearts before we can conclusive state whether or not a difference exists.

To the best of our knowledge, this is the first time OCT has been applied for phenotyping adult mouse hearts. Using OCT, we were able to find significant differences in cardiac morphology between two mouse types. The advantage of using OCT is that it can provide high-resolution, volumetric images of the sample in a cost-effective, non-radiative manner. The quantitative analyses performed in this paper served as a proof-of-concept for the use of OCT in discerning and quantifying changes in cardiac morphology. Although we did not make full use of the high-resolution nature of OCT data in this work, the morphological analyses can be improved through the application of more sophisticated computational anatomy tools, which would allow researchers to study subtle, localized changes in morphology.

6.5. Summary

In this chapter, the cardiac OCT imaging system and computational methods that were developed and described in the previous chapters were applied to a preliminary study that compared the cardiac morphology of Marfan and wild-type mice. Although the sample size was small, the preliminary results suggest that the Marfan mice have dilated left ventricles and a smaller left ventricular mass-to-volume ratio in comparison to their wild-type counterparts. Through the study, we demonstrated the tractability of OCT as a cardiac imaging modality. In the next chapter, the current limitations in our system, and possible future extensions, are discussed.

Chapter 7.   Summary and Future Work

In this thesis, we demonstrated the tractability of using optical coherence tomography (OCT) for phenotyping adult mouse hearts. While OCT has been useful in characterizing the structure and function of embryonic hearts, the same strides have not been made in imaging the whole adult heart [70]–[72]. Due to the limited depth of penetration (~1.5 – 2 millimeters in cardiac tissue) and trade-off between depth of focus and spatial resolution, conventional OCT is unable to image the entire adult mouse heart with high resolution.

As described in Chapter 3, our approach to imaging the whole heart involved the application of optical clearing and multi-perspective imaging to increase penetration depth and spatial resolution, respectively. To acquire images from different perspectives, the heart was rotated relative to the sample beam. A stable rotation device was constructed by incorporating the rotation mount and iris diaphragm into a Thorlab's cage system. One issue with multi-perspective and quantitative OCT imaging is image distortions from the acquisition process. Scanning distortions from non-linear axial scanning and non-telecentric scanning can warp the image, thereby increasing registration mismatches and limiting the validity of quantitative results. These scanning distortions were minimized by limiting the a-scan acquisition to the linear portion of the lateral scan, as well as utilizing a telecentric scan lens for the objective lens.

Another acquisition-related distortion is due to refraction. As discussed in Chapter 4, we corrected for refraction from the outer surface of the heart in each of the volumes prior to registration and stitching. Although we did not verify it ourselves, our algorithm was based off of previously published results that validated the impact of refraction correction on the accuracy of quantitative measurements [53], [54], [56]. After stitching the perspective volumes into a single volume of the whole heart, various morphological parameters were quantified, such as luminal volumes, wall masses and thicknesses, and fiber orientation. Our method of quantifying theses parameters was discussed in Chapter 5.

Finally, we performed a preliminary study comparing the cardiac morphology of 12-month old wild-type mice and transgenic mouse models of Marfan syndrome (MFS), and

presented the results in Chapter 6. This study served dual purposes: it provided a preliminary comparison on the effects of MFS on cardiac morphology, and served to demonstrate the tractability of using OCT to discern and quantify changes in cardiac morphology.

This thesis provided a proof-of-concept of using OCT for cardiovascular phenotyping of adult hearts. Although we were successful in imaging and characterizing mouse hearts using OCT, there are still existing challenges in our project. While improvements were made in the tissue penetration and imaging depth, it was still insufficient for imaging larger hearts. Secondly, the myocardial fiber visibility was inconsistent across the hearts we imaged, which made comparing the fiber orientation between wild-type and MFS mice difficult. In the following sections, we provide possible causes and/or solutions to these challenges.

After discussing the challenges, we next discuss potential improvements and extensions. The morphological analyses of the hearts can be improved through the use of more sophisticated techniques from computational anatomy. Lastly, while we developed the technology using fixed hearts in this project, our OCT system can also eventually be used to image ex-vivo, perfused live hearts. We end this section by discussing adaptations to our system for imaging live hearts.

7.1. Increasing Imaging Depth and Depth of Penetration

Figure 7-3 presents a transverse slice from one of the larger hearts we imaged, showing regions of the heart that had low signal or were not imaged. Given the limited imaging depth of our OCT system (3.5 mm), hearts with a minimum diameter greater than 7mm will have portions that cannot be imaged. The decreased signal at larger depths is due to the limited depth of penetration of OCT.
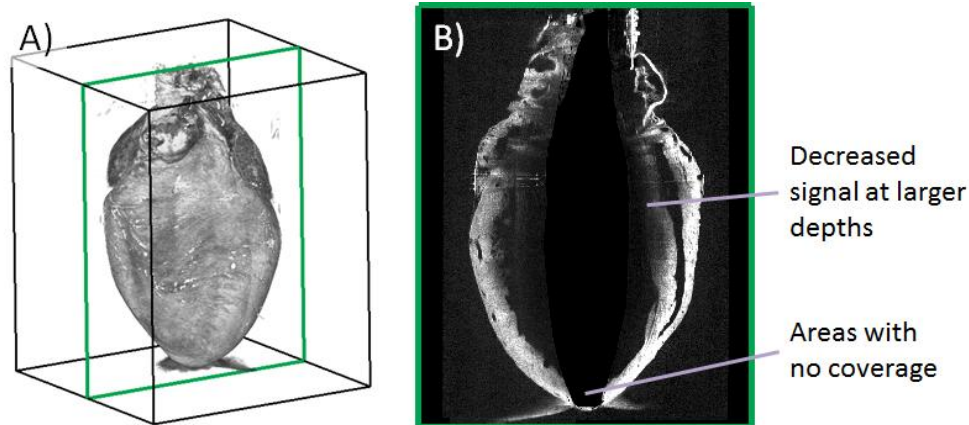
Figure 7-1: Challenges in imaging larger hearts. A) Volumetric rendering showing location of slice. B) Slice showing portions of the heart was were imaged with decreased visibility, or not imaged at all, due to the limited imaging depth and depth of penetration in OCT.

The imaging depth can be increased by resolving the complex-conjugate ambiguity (CCA). CCA, which is due to the symmetry of the cosine terms in the interference equation (Equation 3-1) causes portions of the image to wrap around the reference distance position. While we were able to detect and ignore the wrap-around in the outer surface during the segmentation process, we were not able to distinguish the wrapped portions in the interior of the heart. Removing the CCA through phase-shifting or quadrature detection would double our imaging depth, since both the negative and positive portions of the Fourier-transformed space can be used [73], [74].

Although increasing the imaging depth might give us better coverage of the surface of the heart, it will not help improve the visibility of the deeper structures, such as the interventricular septum, which is limited by tissue penetration. The tissue penetration can be increased by moving to a longer wavelength or by applying stronger clearing agents. The next two sections describe these two potential solutions in more detail.

7.1.1. Improvement in Depth of Penetration by Imaging at 1310 nm

Compared to 1060nm, imaging at 1310nm provides greater tissue penetration due to decreased scattering. However, the tradeoffs to moving to a longer wavelength include decreased signal contrast and lower resolution, since resolution is proportional to wavelength (Equation 3-13). Figure 7-2 compares the visibility at larger depths when imaging at 1060nm and 1310nm. The c-scans (in blue) were acquired at similar depths within the heart. The depths

at which the c-scans were extracted are shown by the blue lines in the b-scans (which are outlined in red). For a given depth, the visibility is much greater at 1310nm. For example, the IVS within the heart is barely visible using the 1060 nm system, while it is clearly visible using 1310nm.
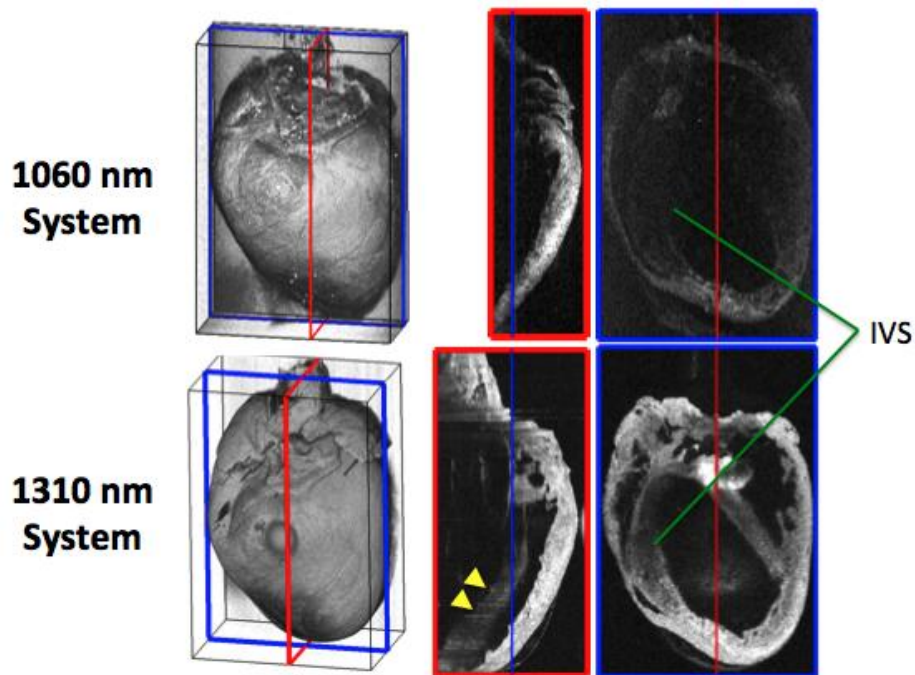
Figure 7-2: Comparison of depth of penetration of 1060nm and 1310nm systems. Volumetric rendering shows location of b-scan (in red) in c-scan (in blue). At a given depth, the visibility at 1310nm is greater than 1060 nm. IVS, interventricular septum.

Switching to a 1310nm system and increasing the imaging depth would allow us to image a greater portion of the heart. It would also allow us to use less potent clearing agents. When we image hearts cleared with 70% glycerol using 1310nm, the other surface of the heart is visible (yellow arrowheads). Thus, we can most likely decrease the glycerol concentration without any negative impact. Using a less-effective optical clearing agent would increase tissue scattering, which is beneficial for image contrast.

7.1.2.   Investigation of More Potent Clearing Agents

Another potential solution to increasing the depth of penetration is to use stronger optical clearing agents. While we chose to use 70% glycerol to clear the mouse heart samples used for this thesis, there are clearing agents that offer greater penetrance. For example, the synergistic

combination of 50% diemthyl sulfoxide (DMSO) and 30% glycerol is more effective than 80% glycerol, due to the membrane permeability and carrier effect of DMSO [75]. However, the use of stronger clearing agents will decrease light scattering and therefore image contrast, as the reflectivity from the sample is decreased (Equation 3-16). While there are stronger clearing agents that can cause the heart to become nearly transparent, these agents are most likely not suitable for OCT imaging since they cause too much SNR loss [76].

7.1.3. Imaging in Refractive-Index-Matching Solution

Imaging in solution rather than air could increase tissue penetration due to the attenuation of refractive mismatch at the surface. One benefit of imaging in solution is the reduction of refractive distortions, thus likely alleviating the need for refraction correction in post-processing. However, other issues with imaging in solution include absorption and back-reflections. The container must be carefully designed so that large back-reflections from the optical surfaces do not affect the OCT image quality. Moreover, the front surface must be orthogonal to the imaging beam to minimize refraction from the air-cage interface, which complicates the issue of minimizing back-reflection. Another issue with imaging in solution is absorption, which is much greater at 1310nm than at 1060nm. For example, if the heart is placed 5mm from the front surface of the cage, the expected attenuation at 1310nm is approximately 7.3 dB, whereas the attenuation at 1060 nm is only 0.7 dB [77]. If the front surface of the cage is designed properly, then imaging the heart at 1060 nm, but not at 1310nm, might be possible.

7.2. Improving the Fiber Visibility

Due to challenges in visualizing the fiber orientation consistently, we were not able to quantify and compare the fiber orientation between the wild-type mice and transgenic mouse model of MFS. To investigate whether or not the lack of visibility was due to insufficient resolution, we imaged section of the left and right ventricle using a higher-resolution system that had a lateral resolution of 11µm (axial resolution remains the same because it depends on the optical bandwidth of the wavelength swept laser). The results of imaging the right and left ventricular free wall have been displayed in Figure 7-3. Comparing the left and right ventricle, the cleavage planes within the right ventricle seem to be larger, thus increasing the visibility of the myofibril orientation. In the LV free wall, the fiber orientation is barely visible. Thus, it is

possible that a higher-resolution system is required to visualize the myofibril orientation in the left ventricle.
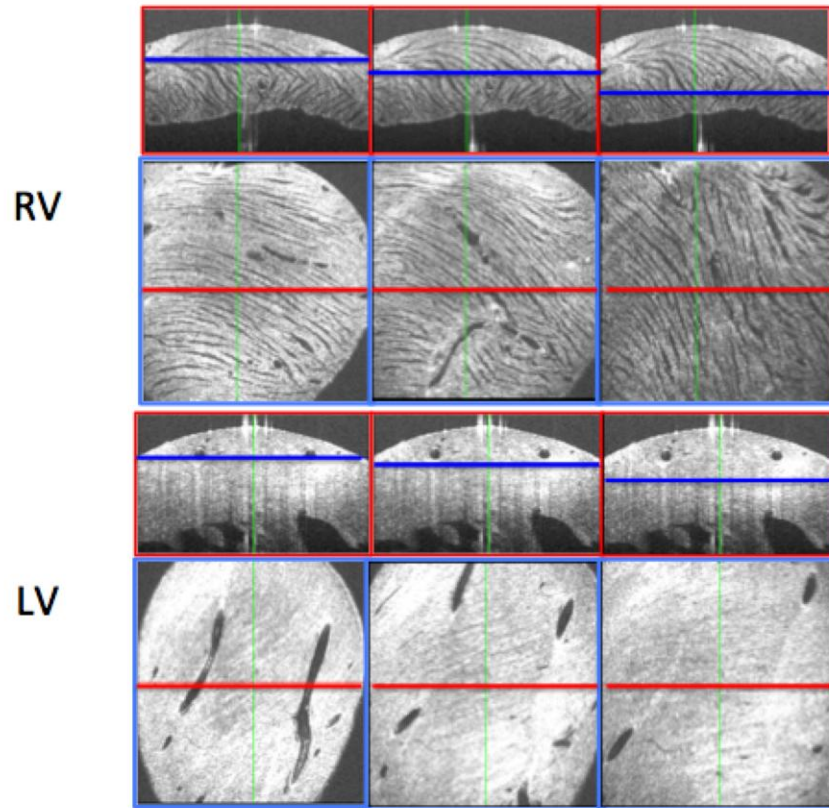
Figure 7-3: Comparison of myofibril visibility in the right and left ventricle. B-scans (red) show location of c-scans (in blue).

Within the right ventricular free wall, there are differences in visibility of the cleavage planes across hearts. Figure 7-4 compares the myofibril orientation in the right ventricular free wall of 2 hearts from 12-month old wild-type littermates. The size of the cleavage planes differs across these two hearts. Due to the role of the cleavage planes in fiber visibility, it is more likely that the difference in visibility is not due to insufficient spatial resolution, but is more due to differences in the preparation, such as variability in the loading conditions during sample preparation prior to fixation, or variability in the fixed heart's contractile state. In future work, we propose to revisit the preparation of the heart.
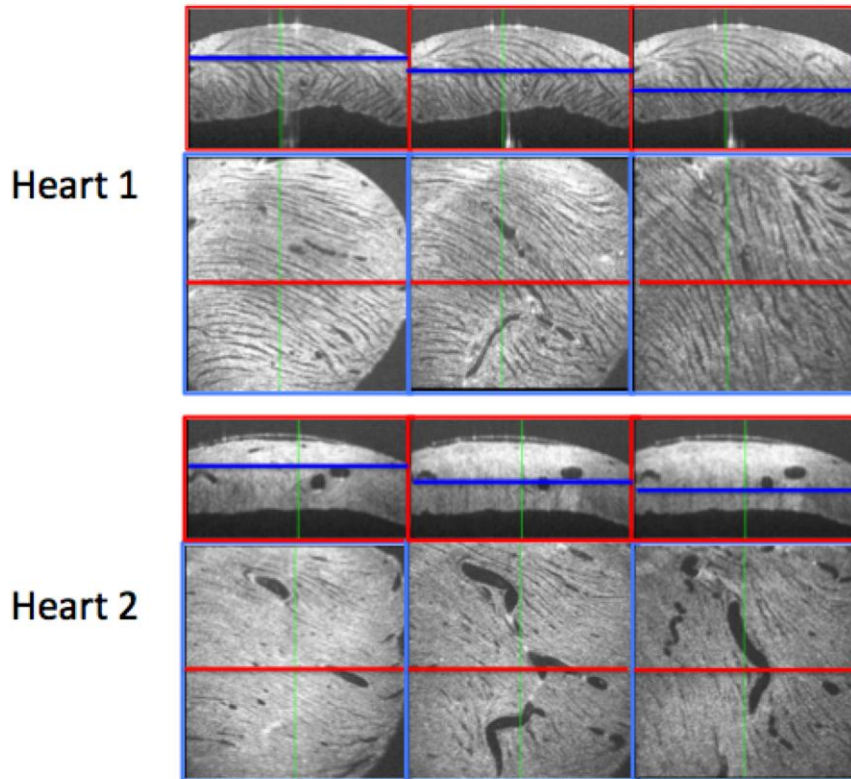
Figure 7-4: Differences in myofibril visibility in the right ventricle across 2 hearts from age-matched wild-type mice. B-scans (red slices) show location of c-scan (in blue).

7.3. Improvements in Morphological Analysis

The morphological analyses presented in this thesis can be improved by applying techniques from computational anatomy. Computational anatomy is an emerging field that applies statistical and mathematical techniques to quantify the variability in biological shapes. One improvement that can be made to the current system is the method of calculating wall thickness. The minimum and perpendicular thickness methods are neither reciprocal nor robust. An alternative method is the Laplacian thickness method, which computes thickness based on streamlines that are perpendicular to both the outer and inner surface and do not intersect with other streamlines [78]. The streamlines can be mathematically represented as:

7-1

$$E = -\nabla\psi,$$

where $\nabla\psi$ is found by solving the Laplace's equation, which is

<div align="right">**7-2**</div>

$$\nabla^2\psi = \frac{\partial^2\psi}{\partial x^2} + \frac{\partial^2\psi}{\partial y^2} + \frac{\partial^2\psi}{\partial z^2}.$$

In this case, $\psi = \psi_1$ and $\psi = \psi_2$ are the outer and inner surfaces [78].

The Laplacian thickness method is more mathematically robust and enforces a one-to-one, reciprocal mapping between the two surfaces. Unlike the perpendicular thickness method, since the method is reciprocal and symmetric, the same thickness measurements will be acquired if the thickness is measured starting from either the outer or inner surface.
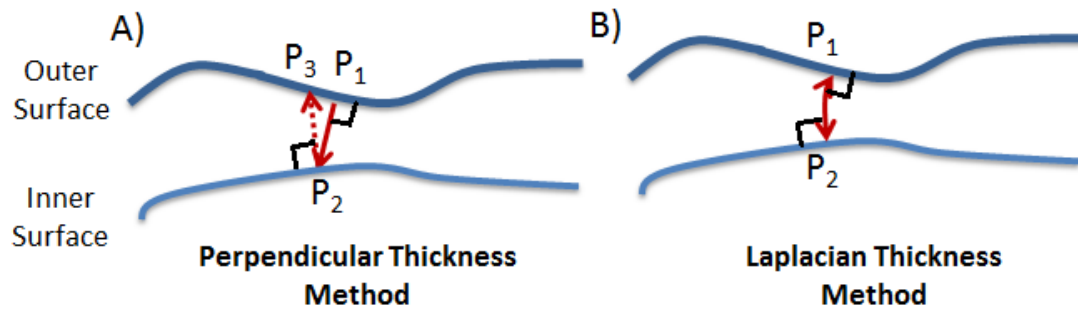
Figure 7-5: Comparison of reciprocity in perpendicular and Laplacian thickness methods. A) Perpendicular thickness method, showing dependence of thickness measurement to which surface it is measured from. B) Laplacian thickness method, which is orthogonal to both surfaces and invariant with respect to which surface it is measured from.

A study comparing the minimum, perpendicular, and Laplacian thickness methods on a segmented cortex found that the Laplacian method was the least sensitive to slice thickness and imaging orientation [79]. In contrast, the perpendicular thickness method was the most sensitive: a change in slice thickness and/or imaging orientation, which in our case corresponds to residual re-alignment errors, caused a significant difference in the calculated thickness [79]. Compared to the other methods, the results from the Laplacian thickness method could be more repeatable.

Another technique from computational anatomy that would be useful in quantifying cardiac morphology is nonrigid, diffeomorphic registration, which provides a one-to-one geometric correspondence across different samples. In the heart, this registration tool has been

applied to cardiac MRI images to quantify both local and global changes in heart geometry and fiber orientation [80]. When applied to our OCT volumes, diffeomorphic registration would allow us to quantitatively compare and perform statistical analyses on the wall thickness, fiber orientation, and ventricular shape at the same regions across multiple hearts.

7.4. Ex-Vivo Perfused Live-Heart Imaging

Finally, our project can be extended to imaging ex-vivo, perfused, live hearts, to acquire 3D volumes of the heart at different points in the cardiac cycle. From these volumes, physiological parameters such as ejection fraction, stroke volume, and mechanical strain can be calculated. Differences in strain are an important, and early, indicator of heart disease [81]–[83].

Prior to imaging the beating heart, the OCT system speed needs to be increased. Our current system images at a line rate of 100,000 a-scans per second, or 100 kHz. The volumetric rate of imaging is dependent on the number of a-scans within the volume. For our current volume size consisting of 400x800 a-scans, the volumetric imaging rate is 0.3125 volumes/second, or 3.2 seconds/volume. Since the mouse heart beats at an average rate of 500-600 beats/min, or 8-10 beats/second, our current imaging rate is insufficient for capturing volumes of the heart at a 'single point' in the cardiac cycle. The volumetric imaging rate can be increased by decreasing the volume size; however, the decrease in sampling rate inversely impacts the spatial resolution. Another potential solution is to increase the a-scan rate.

Novel swept sources with high speed a-scan rates are emerging, but are not yet mature. Alternatively, the line rate of the wavelength swept source used in this research could be increased through the implementation of double-buffered OCT [84]–[86]. Double buffering is used to increase the line rate of wavelength-swept lasers that have a low duty cycle (≤ 50%). To implement the double-buffered technique, the swept-source output is first split by a fiber coupler, one portion of which is directed to an optical delay line. A coupler with uneven splitting ratio (in this case, 60:40) is commonly used, and the arm with the greater percentage of the power goes through the delay line to compensate for the loss in power in the spool (typically ~1 km). Since light travels at a speed of

$$v = \frac{c}{n_{Fiber}} \cong \frac{3.0 * 10^9}{1.47} = 2.04 * 10^9 \frac{m}{s},$$

the 1km fiber spool causes a delay of 5 μs, which is half the period of the a-scan rate of 100kHz.

The delayed and original signals are then combined by either using a 50:50 fiber coupler, or a fast optical switch [85]. An ideal, wavelength-flattened fiber coupler (FC) would combine the delayed and original signal equally and then split it into two spots with equal power. However, each spot has 3dB lower power than the original beam. To improve the power efficiency, an optical switch can be used instead of the fiber coupler. The switch from Boston Applied Technologies, for example, offers a switch time of <60 ns, and maximum crosstalk of 26dB, which corresponds to a splitting ratio of 99.7:0.3. Figure 7-6 presents a sample schematic of a double-buffered source, how it connects with an OCT system, and the other parts that are required to make it work. In the figure, the interchangeable fiber coupler and switch has been denoted as FC/S.

We have initiated preliminary work on implementing the double-buffered configuration using the Axsun wavelength-swept laser described in Chapter 3. Figure 7-7 displays the original spectrum, the delayed spectrum, and the combined spectrum at the output of the FC/S. For Figure 7-6c, the output at the switch was simulated in MATLAB (Mathworks Inc., MA) using a switch time of 60 ns and maximum crosstalk suppression of 26dB, according to manufacturer specifications. Along with improvements in power efficiency, the use of a switch also increases the usable bandwidth of the double-buffered source in cases where the duty cycle of the original source is larger than 50%. The laser that we used had a duty cycle of 66.4%.
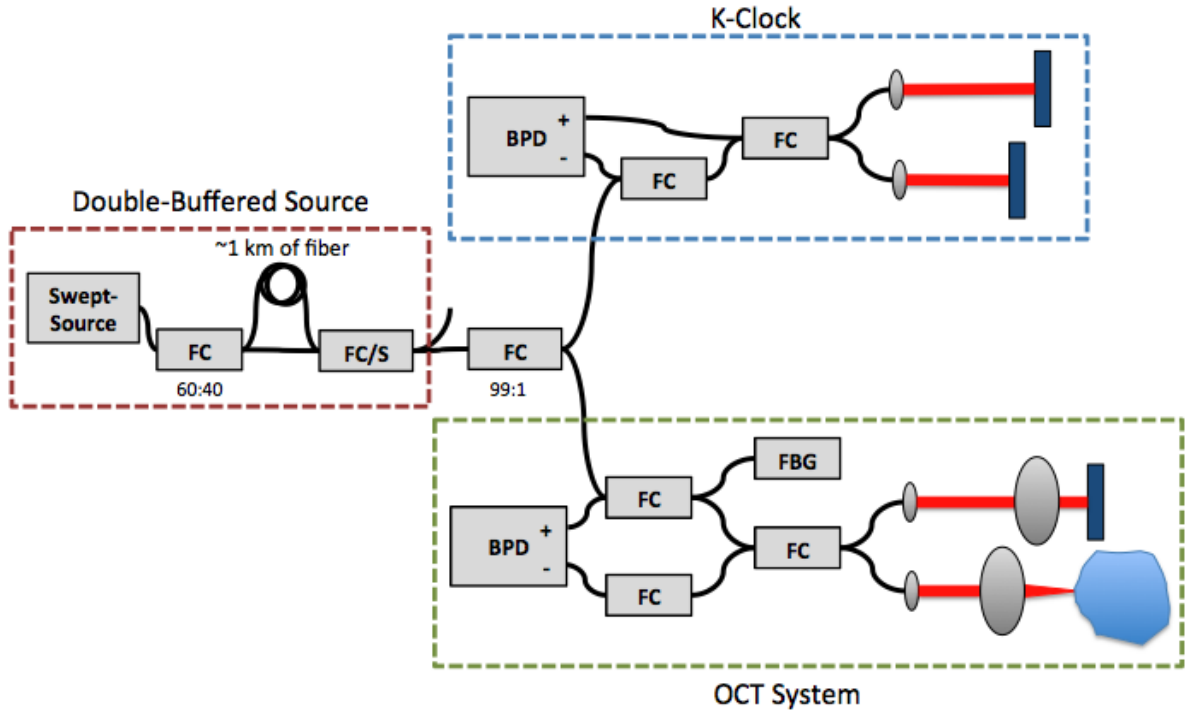
Figure 7-6: Schematic of double-buffered OCT system, including double-buffered source, k-clock, and OCT system. FBG, Fiber-Bragg Grating; FC, fiber coupler; FC/S, fiber coupler or switch; BPD, balanced photodiode detector.
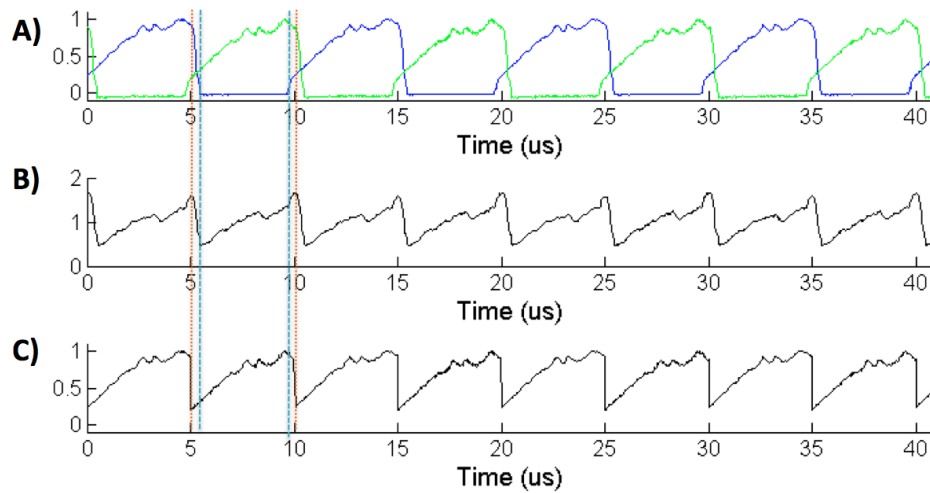
Figure 7-7: A) Overlay of the original (blue) and delayed (green) spectra. B) Combined signal after the FC/S, using a fiber coupler. C) Combined signal after the FC/S, using the switch. The orange and blue dashed lines compare the usable bandwidth when using the switch and fiber coupler respectively. The usable bandwidth is decreased when a fiber coupler is used to combine the signals due to the overlap in the original and delayed signals.

As mentioned in Chapter 3, a k-clock provides the calibration signal that converts the acquired interferogram from time to k-space. The k-clock supplied by the commercial swept source system used (Axsun Technologies, Billerica, MA) is only present during the original sweep. To resample the delayed portion of the sweep, we could delay the provided k-clock by 5µs. However, due to dispersion from the 1km delay, and the fact that the delay is not exactly 5µs, the provided k-clock will not be accurate for the delayed spectrum. To provide more accurate resampling, a fixed-path length interferometer can be built to provide a stable calibration signal for both the original and delayed sweep.

The final component required for implementing the double-buffered scheme is a Fiber-Bragg Grating (FBG), which serves to trigger each a-scan at the same phase. An FBG reflects a specific wavelength while transmitting the remaining wavelengths. A narrow-band FBG with high reflectivity can provide a phase-stable trigger for both the original and delayed spectrum. A representative signal from the FBG has been provided along with the original and delayed spectrum in Figure 7-8.
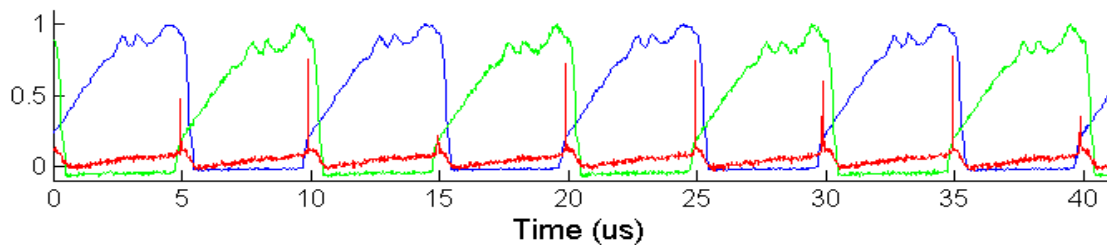
Figure 7-8: Original (blue) and delayed (green) signals, with FBG trigger (red)

The proposed double-buffered system would double the speed of our current imaging system and enable fast scanning. For the double-buffered engine, although the use of the fiber coupler instead of a switch would result in a 3dB loss in power in each arm, both of these spots could also be used simultaneously [86]. Multi-spot OCT would allow us to double our effective imaging speed, or image the heart from multiple perspectives simultaneously, which could be useful in imaging live hearts and studying cardiovascular dynamics.

References

[1]   G. D. Pearson, R. Devereux, B. Loeys, C. Maslen, D. Milewicz, R. Pyeritz, F. Ramirez, D. Rifkin, L. Sakai, L. Svensson, A. Wessels, J. Van Eyk, and H. C. Dietz, "Report of the National Heart, Lung, and Blood Institute and National Marfan Foundation Working Group on research in Marfan syndrome and related disorders.," *Circulation*, vol. 118, no. 7, pp. 785–91, Aug. 2008.

[2]   D. P. Judge and H. C. Dietz, "Marfan's syndrome," *Lancet*, vol. 366, pp. 1965–1976, 2005.

[3]   V. Cañadas, I. Vilacosta, I. Bruna, and V. Fuster, "Marfan syndrome. Part 1: pathophysiology and diagnosis.," *Nat. Rev. Cardiol.*, vol. 7, no. 5, pp. 256–65, May 2010.

[4]   E. a Gonzales, "Marfan syndrome.," *J. Am. Acad. Nurse Pract.*, vol. 21, no. 12, pp. 663–70, Dec. 2009.

[5]   N. M. Ammash, T. M. Sundt, and H. M. Connolly, "Marfan syndrome-diagnosis and management.," *Curr. Probl. Cardiol.*, vol. 33, no. 1, pp. 7–39, Jan. 2008.

[6]   Y. von Kodolitsch and P. N. Robinson, "Marfan syndrome: an update of genetics, medical and surgical management.," *Heart*, vol. 93, no. 6, pp. 755–60, Jun. 2007.

[7]   A. Madamanchi, "Mouse Models in Cardiology Research," no. 5, pp. 34–39, 2004.

[8]   P. a Doevendans, M. J. Daemen, E. D. de Muinck, and J. F. Smits, "Cardiovascular phenotyping in mice.," *Cardiovasc. Res.*, vol. 39, no. 1, pp. 34–49, Jul. 1998.

[9]   T. E. Bunton, N. J. Biery, L. Myers, B. Gayraud, F. Ramirez, and H. C. Dietz, "Phenotypic alteration of vascular smooth muscle cells precedes elastolysis in a mouse model of Marfan syndrome.," *Circ. Res.*, vol. 88, no. 1, pp. 37–43, Jan. 2001.

[10]   V. Marque, P. Kieffer, B. Gayraud, I. Lartaud-Idjouadiene, F. Ramirez, and J. Atkinson, "Aortic Wall Mechanics and Composition in a Transgenic Mouse Model of Marfan Syndrome," *Arterioscler. Thromb. Vasc. Biol.*, vol. 21, no. 7, pp. 1184–1189, Jul. 2001.

[11]   J. P. Habashi, D. P. Judge, T. M. Holm, R. D. Cohn, L. Bart, T. K. Cooper, L. Myers, E. C. Klein, G. Liu, C. Calvi, E. R. Neptune, M. K. Halushka, D. Bedja, K. Gabrielson, B. Daniel, L. Carta, F. Ramirez, D. L. Huso, and H. C. Dietz, "Losartan, an AT1 Antagonist Prevents Aortic Aneurysm in a Mouse Model of Marfan Syndrome," *Science (80-.).*, vol. 312, no. 5770, pp. 117–121, 2006.

[12] M. Groenink, A. W. den Hartog, R. Franken, T. Radonic, V. de Waard, J. Timmermans, A. J. Scholte, M. P. van den Berg, A. M. Spijkerboer, H. a Marquering, A. H. Zwinderman, and B. J. M. Mulder, "Losartan reduces aortic dilatation rate in adults with Marfan syndrome: a randomized controlled trial.," *Eur. Heart J.*, vol. 34, no. 45, pp. 3491–500, Dec. 2013.

[13] A. M. Shah and S. D. Solomon, "A unified view of ventricular remodelling.," *Eur. J. Heart Fail.*, vol. 12, no. 8, pp. 779–81, Aug. 2010.

[14] J. R. Cook, L. Carta, L. Bénard, E. R. Chemaly, E. Chiu, S. K. Rao, T. G. Hampton, P. Yurchenco, G. R. Consortium, K. D. Costa, R. J. Hajjar, and F. Ramirez, "Abnormal muscle mechanosignaling triggers cardiomyopathy in mice with Marfan syndrome," vol. 124, no. 3, pp. 1329–1339, 2014.

[15] L. J. Meijboom, J. Timmermans, J. P. van Tintelen, G. J. Nollen, J. De Backer, M. P. van den Berg, G. H. Boers, and B. J. M. Mulder, "Evaluation of left ventricular dimensions and function in Marfan's syndrome without significant valvular regurgitation.," *Am. J. Cardiol.*, vol. 95, no. 6, pp. 795–7, Mar. 2005.

[16] J. F. De Backer, D. Devos, P. Segers, D. Matthys, K. François, T. C. Gillebert, A. M. De Paepe, and J. De Sutter, "Primary impairment of left ventricular function in Marfan syndrome.," *Int. J. Cardiol.*, vol. 112, no. 3, pp. 353–8, Oct. 2006.

[17] B. B. Das, a L. Taylor, and a T. Yetman, "Left ventricular diastolic dysfunction in children and young adults with Marfan syndrome.," *Pediatr. Cardiol.*, vol. 27, no. 2, pp. 256–8, 2006.

[18] F. Alpendurada, J. Wong, A. Kiotsekoglou, W. Banya, A. Child, S. K. Prasad, D. J. Pennell, and R. H. Mohiaddin, "Evidence for Marfan cardiomyopathy.," *Eur. J. Heart Fail.*, vol. 12, no. 10, pp. 1085–91, Oct. 2010.

[19] K. A. H. Arasiewicz, B. G. S. Tarkoski, L. Z. An, D. A. K. Napik, and S. L. A. Damson, "A NEW ULTRASOUND INSTRUMENT FOR IN VIVO MICROIMAGING OF MICE," *Ultrasound Med. Biol.*, vol. 28, no. 9, pp. 1165–1172, 2002.

[20] H. Dormand and R. H. Mohiaddin, "Cardiovascular magnetic resonance in Marfan syndrome.," *J. Cardiovasc. Magn. Reson.*, vol. 15, p. 33, Jan. 2013.

[21] K. Ramanujan, "New CT scanner images fossils, mice from the inside out | Cornell Chronicle." [Online]. Available: http://www.news.cornell.edu/stories/2011/05/new-scanner-takes-images-inside-and-out. [Accessed: 09-Apr-2014].

[22] "Small Animal Imaging Systems : Addressing The Costs | Nutaq." [Online]. Available: http://nutaq.com/en/blog/small-animal-imaging-systems-addressing-costs. [Accessed: 09-Apr-2014].

[23] "Today's MRI Market - Magnetica." [Online]. Available: http://www.magnetica.com/page/innovation/todays-mri-market/. [Accessed: 09-Apr-2014].

[24] "MicroCT opens door to new research options for Ohio University." [Online]. Available: http://www.ohio.edu/outlook/05-06/August/618f-056.cfm. [Accessed: 09-Apr-2014].

[25] "UBC MRI Research Centre: Facilities: 7T Imaging rates." [Online]. Available: http://www.mriresearch.ubc.ca/content/facilities/7T/rates.php. [Accessed: 09-Apr-2014].

[26] "Fees | Micro CT Laboratory | University of Calgary." [Online]. Available: http://www.ucalgary.ca/microct/access_and_services/fees. [Accessed: 09-Apr-2014].

[27] "UBC Center for High-Throughput Phenogenics Fee." [Online]. Available: http://www.phenogenomics.dentistry.ubc.ca/pdf/PhenogenomicsPriceList.pdf. [Accessed: 09-Apr-2014].

[28] D. Huang, E. A. Swanson, C. P. Lin, J. S. Schuman, W. G. Stinson, W. Chang, M. R. Hee, T. Flotte, K. Gregory, and C. A. Puliafito, "Optical coherence tomography.," *Science*, vol. 254, no. 5035, pp. 1178–81, Nov. 1991.

[29] M. A. Laflamme, M. M. Sebastian, and B. S. Buetow, "Cardiovascular," in *Comparative Anatomy and Histology*, no. Figure 1, 2012, pp. 135–153.

[30] P. Matt, J. Habashi, T. Carrel, D. E. Cameron, J. E. Van Eyk, and H. C. Dietz, "Recent advances in understanding Marfan syndrome: should we now treat surgical patients with losartan?," *J. Thorac. Cardiovasc. Surg.*, vol. 135, no. 2, pp. 389–94, Feb. 2008.

[31] Y. von Kodolitsch and P. N. Robinson, "Marfan syndrome: an update of genetics, medical and surgical management.," *Heart*, vol. 93, no. 6, pp. 755–60, Jun. 2007.

[32] H. C. Dietz, G. R. Cutting, R. E. Pyeritz, C. L. Maslen, L. Y. Sakai, G. M. Corson, E. G. Puffenberger, A. Hamosh, E. J. Nanthakumar, and S. M. Curristin, "Marfan syndrome caused by a recurrent de novo missense mutation in the fibrillin gene.," *Nature*, vol. 352, no. 6333, pp. 337–9, Jul. 1991.

[33] P. N. Robinson, "The molecular genetics of Marfan syndrome and related microfibrillopathies," *J. Med. Genet.*, vol. 37, no. 1, pp. 9–25, Jan. 2000.

[34] C. M. Ng, A. Cheng, L. A. Myers, F. Martinez-murillo, C. Jie, D. Bedja, K. L. Gabrielson, J. M. W. Hausladen, R. P. Mecham, D. P. Judge, and H. C. Dietz, "TGF- β – dependent pathogenesis of mitral valve prolapse in a mouse model of Marfan syndrome," *J. Clin. Invest.*, vol. 114, no. 11, pp. 1586–1592, 2004.

[35] E. R. Neptune, P. a Frischmeyer, D. E. Arking, L. Myers, T. E. Bunton, B. Gayraud, F. Ramirez, L. Y. Sakai, and H. C. Dietz, "Dysregulation of TGF-beta activation contributes to pathogenesis in Marfan syndrome.," *Nat. Genet.*, vol. 33, no. 3, pp. 407–11, Mar. 2003.

[36] T. M. Holm, J. P. Habashi, J. J. Doyle, D. Bedja, C. Van Erp, M. E. Lindsay, D. Kim, F. Schoenhoff, D. Ronald, B. L. Loeys, C. J. Thomas, S. Patnaik, J. J. Marugan, P. Daniel, and H. C. Dietz, "Noncanonical TGFb Signaling Contributes to Aortic Aneurysm Progression in Marfan Syndrome Mice," *Science (80-.).*, vol. 332, no. 6027, pp. 358–361, 2011.

[37] I. J. LeGrice, B. H. Smaill, L. Z. Chai, S. G. Edgar, J. B. Gavin, and P. J. Hunter, "Laminar structure of the heart: ventricular myocyte arrangement and connective tissue architecture in the dog.," *Am. J. Physiol.*, vol. 269, no. 2 Pt 2, pp. H571–82, Aug. 1995.

[38] I. J. Legrice, B. H. Smaill, L. Z. Chai, S. G. Edgar, J. B. Gavin, and P. J. Hunter, "Laminar structure of the heart : ventricular myocyte arrangement and connective tissue architecture in the dog," *Am. J. Physiol. Heart Circ. Physiol.*, vol. 269, pp. H571–H582, 1995.

[39] L. J. Healy, Y. Jiang, and E. W. Hsu, "Quantitative comparison of myocardial fiber structure between mice, rabbit, and sheep using diffusion tensor cardiovascular magnetic resonance.," *J. Cardiovasc. Magn. Reson.*, vol. 13, no. 1, p. 74, Jan. 2011.

[40] F. E. Rademakers, W. J. Rogers, W. H. Guier, G. M. Hutchins, C. O. Siu, M. L. Weisfeldt, J. L. Weiss, and E. P. Shapiro, "Relation of regional cross-fiber shortening to wall thickening in the intact heart. Three-dimensional strain analysis by NMR tagging," *Circulation*, vol. 89, no. 3, pp. 1174–1182, Mar. 1994.

[41] H. Ashikaga, J. C. Criscione, J. H. Omens, J. W. Covell, and N. B. Ingels, "Transmural left ventricular mechanics underlying torsional recoil during relaxation.," *Am. J. Physiol. Heart Circ. Physiol.*, vol. 286, no. 2, pp. H640–7, Feb. 2004.

[42] T. Arts, P. C. Veenstra, and R. S. Reneman, "Epicardial deformation and left ventricular wall mechanisms during ejection in the dog," *Am J Physiol Hear. Circ Physiol*, vol. 243, no. 3, pp. H379–390, Sep. 1982.

[43] J. N. Cohn, R. Ferrari, and N. Sharpe, "Cardiac remodeling—concepts and clinical implications: a consensus paper from an international forum on cardiac remodeling," *J. Am. Coll. Cardiol.*, vol. 35, no. 3, pp. 569–582, Mar. 2000.

[44] W. H. Gaasch and T. E. Meyer, "Left ventricular response to mitral regurgitation: implications for management.," *Circulation*, vol. 118, no. 22, pp. 2298–303, Nov. 2008.

[45] A. Wessels and D. Sedmera, "Developmental anatomy of the heart: a tale of mice and man.," *Physiol. Genomics*, vol. 15, no. 3, pp. 165–76, Nov. 2003.

[46] D. P. Judge, N. J. Biery, D. R. Keene, J. Geubtner, L. Myers, D. L. Huso, L. Y. Sakai, and H. C. Dietz, "Evidence for a critical contribution of haploinsufficiency in the complex pathogenesis of Marfan syndrome," vol. 114, no. 2, 2004.

[47]   L. Pereira, S. Y. Lee, B. Gayraud, K. Andrikopoulos, S. D. Shapiro, T. Bunton, N. J. Biery, H. C. Dietz, L. Y. Sakai, and F. Ramirez, "Pathogenetic sequence for aneurysm revealed in mice underexpressing fibrillin-1," *Proc. Natl. Acad. Sci.*, vol. 96, no. 7, pp. 3819–3823, Mar. 1999.

[48]   W. M. H. Behan, C. Longman, R. K. H. Petty, P. Comeglio, A. H. Child, M. Boxer, P. Foskett, and D. G. F. Harriman, "Muscle fibrillin deficiency in Marfan's syndrome myopathy," *J. Neurol. Neurosurg. Psychiatry*, vol. 74, pp. 633–639, 2003.

[49]   J. Izatt and M. Choma, "Theory of optical coherence tomography," in *Optical coherence tomography*, J. G. Fujimoto and W. Drexler, Eds. 2008, pp. 47–72.

[50]   M. Choma, M. Sarunic, C. Yang, and J. Izatt, "Sensitivity advantage of swept source and Fourier domain optical coherence tomography," *Opt. Express*, vol. 11, no. 18, p. 2183, Sep. 2003.

[51]   P.-L. Hsiung, P. R. Nambiar, and J. G. Fujimoto, "Effect of tissue preservation on imaging using ultrahigh resolution optical coherence tomography.," *J. Biomed. Opt.*, vol. 10, no. 6, p. 064033, 2012.

[52]   Y. He and R. K. Wang, "Dynamic optical clearing effect of tissue impregnated with hyperosmotic agents and studied with optical coherence tomography.," *J. Biomed. Opt.*, vol. 9, no. 1, pp. 200–6, Jan. 2004.

[53]   V. Westphal, A. Rollins, S. Radhakrishnan, and J. Izatt, "Correction of geometric and refractive image distortions in optical coherence tomography applying Fermat's principle.," *Opt. Express*, vol. 10, no. 9, pp. 397–404, May 2002.

[54]   S. Ortiz, D. Siedlecki, I. Grulkowski, L. Remon, D. Pascual, M. Wojtkowski, and S. Marcos, "Optical distortion correction in optical coherence tomography for quantitative ocular anterior segment by three-dimensional imaging.," *Opt. Express*, vol. 18, no. 3, pp. 2782–96, Feb. 2010.

[55]   L. Younes, "Mathematical Image Analysis AMS493," 2008.

[56]   M. Zhao, A. N. Kuo, and J. a Izatt, "3D refraction correction and extraction of clinical parameters from spectral domain optical coherence tomography of the cornea.," *Opt. Express*, vol. 18, no. 9, pp. 8923–36, Apr. 2010.

[57]   P. J. Burt and E. H. Adelson, "A multiresolution spline with application to image mosaics," *ACM Trans. Graph.*, vol. 2, no. 4, pp. 217–236, Oct. 1983.

[58]   M. Brown and D. G. Lowe, "Automatic Panoramic Image Stitching using Invariant Features," *Int. J. Comput. Vis.*, vol. 74, no. 1, pp. 59–73, Dec. 2006.

[59]   J. C, J. Y. Boire, J. C. Maublant, J. M, and M. Zanca, "Automatic detection of the left ventricular myocardium long axis and center in thallium-201 single photon emission computed tomography," *Eur. J. Nucl. Med.*, vol. 19, no. 12, pp. 1032–1037, 1992.

[60] S. Dwivedi, A. J. Da Silva, A. Wong, A. Gervais, S. Flowers, and H. Hines, "Automated cardiac pose computation from reconstructed myocardial SPECT images," *2011 IEEE Nucl. Sci. Symp. Conf. Rec.*, pp. 2787–2794, Oct. 2011.

[61] R. a deKemp and C. Nahmias, "Automated determination of the left ventricular long axis in cardiac positron tomography.," *Physiol. Meas.*, vol. 17, no. 2, pp. 95–108, May 1996.

[62] C. Rickers, N. M. Wilke, M. Jerosch-Herold, S. A. Casey, P. Panse, N. Panse, J. Weil, A. G. Zenovich, and B. J. Maron, "Utility of cardiac magnetic resonance imaging in the diagnosis of hypertrophic cardiomyopathy.," *Circulation*, vol. 112, no. 6, pp. 855–61, Aug. 2005.

[63] N. Kawel, E. B. Turkbey, J. J. Carr, J. Eng, A. S. Gomes, W. G. Hundley, C. Johnson, S. C. Masri, M. R. Prince, R. J. van der Geest, J. a C. Lima, and D. a Bluemke, "Normal left ventricular myocardial thickness for middle-aged and older subjects with steady-state free precession cardiac magnetic resonance: the multi-ethnic study of atherosclerosis.," *Circ. Cardiovasc. Imaging*, vol. 5, no. 4, pp. 500–8, Jul. 2012.

[64] W. J. Karlon, J. W. Covell, a D. McCulloch, J. J. Hunter, and J. H. Omens, "Automated measurement of myofiber disarray in transgenic mice with ventricular expression of ras.," *Anat. Rec.*, vol. 252, no. 4, pp. 612–25, Dec. 1998.

[65] C. P. Fleming, C. M. Ripplinger, B. Webb, I. R. Efimov, and A. M. Rollins, "Quantification of cardiac fiber orientation using optical coherence tomography.," *J. Biomed. Opt.*, vol. 13, no. 3, p. 030505, 2011.

[66] W. J. Karlon, a D. McCulloch, J. W. Covell, J. J. Hunter, and J. H. Omens, "Regional dysfunction correlates with myofiber disarray in transgenic mice with ventricular expression of ras.," *Am. J. Physiol. Heart Circ. Physiol.*, vol. 278, no. 3, pp. H898–906, Mar. 2000.

[67] D. J. Hautemann, "Fiber architecture of the post-mortem rat heart obtained with Diffusion Tensor Imaging," 2007.

[68] A. Ghanem, W. Röll, T. Hashemi, O. Dewald, P. C. Djoufack, K. B. Fink, J. Schrickel, T. Lewalter, B. Lüderitz, and K. Tiemann, "Echocardiographic assessment of left ventricular mass in neonatal and adult mice: accuracy of different echocardiographic methods.," *Echocardiography*, vol. 23, no. 10, pp. 900–7, Nov. 2006.

[69] D. E. Forman, A. Cittadini, G. Azhar, P. S. Douglas, and J. Y. Wei, "Cardiac Morphology and Function in Senescent Rats: Gender-Related Differences," *J. Am. Coll. Cardiol.*, vol. 30, no. 7, pp. 1872–1877, Dec. 1997.

[70] M. W. Jenkins, F. Rothenberg, D. Roy, V. P. Nikolski, Z. Hu, M. Watanabe, D. L. Wilson, I. R. Efimov, and a M. Rollins, "4D embryonic cardiography using gated optical coherence tomography.," *Opt. Express*, vol. 14, no. 2, pp. 736–48, Jan. 2006.

[71] M. W. Jenkins, P. Patel, H. Deng, M. M. Montano, M. Watanabe, and A. M. Rollins, "Phenotyping transgenic embryonic murine hearts using optical coherence tomography.," *Appl. Opt.*, vol. 46, no. 10, pp. 1776–81, Apr. 2007.

[72] X. Liu, K. Tobita, R. J. B. Francis, and C. W. Lo, "Imaging techniques for visualizing and phenotyping congenital heart defects in murine models.," *Birth Defects Res. C. Embryo Today*, vol. 99, no. 2, pp. 93–105, Jun. 2013.

[73] M. Wojtkowski, a Kowalczyk, R. Leitgeb, and a F. Fercher, "Full range complex spectral optical coherence tomography technique in eye imaging.," *Opt. Lett.*, vol. 27, no. 16, pp. 1415–7, Aug. 2002.

[74] M. Sarunic, M. a Choma, C. Yang, and J. a Izatt, "Instantaneous complex conjugate resolved spectral domain and swept-source OCT using 3x3 fiber couplers.," *Opt. Express*, vol. 13, no. 3, pp. 957–67, Feb. 2005.

[75] X. Xu and R. K. Wang, "Synergistic effect of hyperosmotic agents of dimethyl sulfoxide and glycerol on optical clearing of gastric tissue studied with near infrared spectroscopy," *Phys. Med. Biol.*, vol. 49, no. 3, pp. 457–468, Feb. 2004.

[76] R. M. Smith, A. Matiukas, C. W. Zemlin, and A. M. Pertsov, "Nondestructive optical determination of fiber organization in intact myocardial wall.," *Microsc. Res. Tech.*, vol. 71, no. 7, pp. 510–6, Jul. 2008.

[77] K. F. Palmer and D. Williams, "Optical properties of water in the near infrared," *J. Opt. Soc. Am.*, vol. 64, no. 8, p. 1107, Aug. 1974.

[78] S. E. Jones, B. R. Buchbinder, and I. Aharon, "Three-dimensional mapping of cortical thickness using Laplace's Equation," *Hum. Brain Mapp.*, vol. 11, no. 1, pp. 12–32, Sep. 2000.

[79] H. Haidar and J. S. Soul, "Measurement of cortical thickness in 3D brain MRI data: validation of the Laplacian method.," *J. Neuroimaging*, vol. 16, no. 2, pp. 146–53, Apr. 2006.

[80] M. F. Beg, P. A. Helm, E. Mcveigh, M. I. Miller, and L. Raimond, "Computational Cardiac Anatomy using MRI," *Magn. Reson. Med.*, vol. 52, no. 5, pp. 1167–1174, 2005.

[81] T. Arts, K. D. Costa, and J. W. Covell, "Relating myocardial laminar architecture to shear strain and muscle fiber orientation," *Am. J. Physiol. Heart Circ. Physiol.*, vol. 280, pp. 2222–2229, 2001.

[82] T. Varghese, J. a Zagzebski, P. Rahko, and C. S. Breburda, "Ultrasonic imaging of myocardial strain using cardiac elastography.," *Ultrason. Imaging*, vol. 25, no. 1, pp. 1–16, Jan. 2003.

[83]   P. M. Smith, V. Daruwalla, B. H. Freed, B. S. Spottiswoode, K. Kalisz, J. C. Carr, and J. D. Collins, "Myocardial strain analysis in patients with Heart Failure with preserved Ejection Fraction using bright blood cine MR images: A comparison with speckle-tracking echocardiography," *J. Cardiovasc. Magn. Reson.*, vol. 16, no. Suppl 1, p. P71, 2014.

[84]   R. Huber, D. C. Adler, and J. G. Fujimoto, "Buffered Fourier domain mode locking: unidirectional swept laser sources for optical coherence tomography imaging at 370,000 lines/s," *Opt. Lett.*, vol. 31, no. 20, p. 2975, 2006.

[85]   A.-H. Dhalla, K. Shia, and J. A. Izatt, "Efficient sweep buffering in swept source optical coherence tomography using a fast optical switch.," *Biomed. Opt. Express*, vol. 3, no. 12, pp. 3054–66, Dec. 2012.

[86]   B. Potsaid, B. Baumann, D. Huang, S. Barry, A. E. Cable, J. S. Schuman, J. S. Duker, and J. G. Fujimoto, "Ultrahigh speed 1050nm swept source/Fourier domain OCT retinal and anterior segment imaging at 100,000 to 400,000 axial scans per second.," *Opt. Express*, vol. 18, no. 19, pp. 20029–48, Sep. 2010.